Rotating heat pipe assisted annealing

Çelik, Metin

DOI
10.4233/uuid:1e0e9c0b-06f0-4b11-ab5f-40fcfcacbea4

Publication date
2020

Document Version
Final published version

Citation (APA)
Çelik, M. (2020). *Rotating heat pipe assisted annealing*. [Dissertation (TU Delft), Delft University of Technology]. https://doi.org/10.4233/uuid:1e0e9c0b-06f0-4b11-ab5f-40fcfcacbea4

ROTATING HEAT PIPE ASSISTED ANNEALING

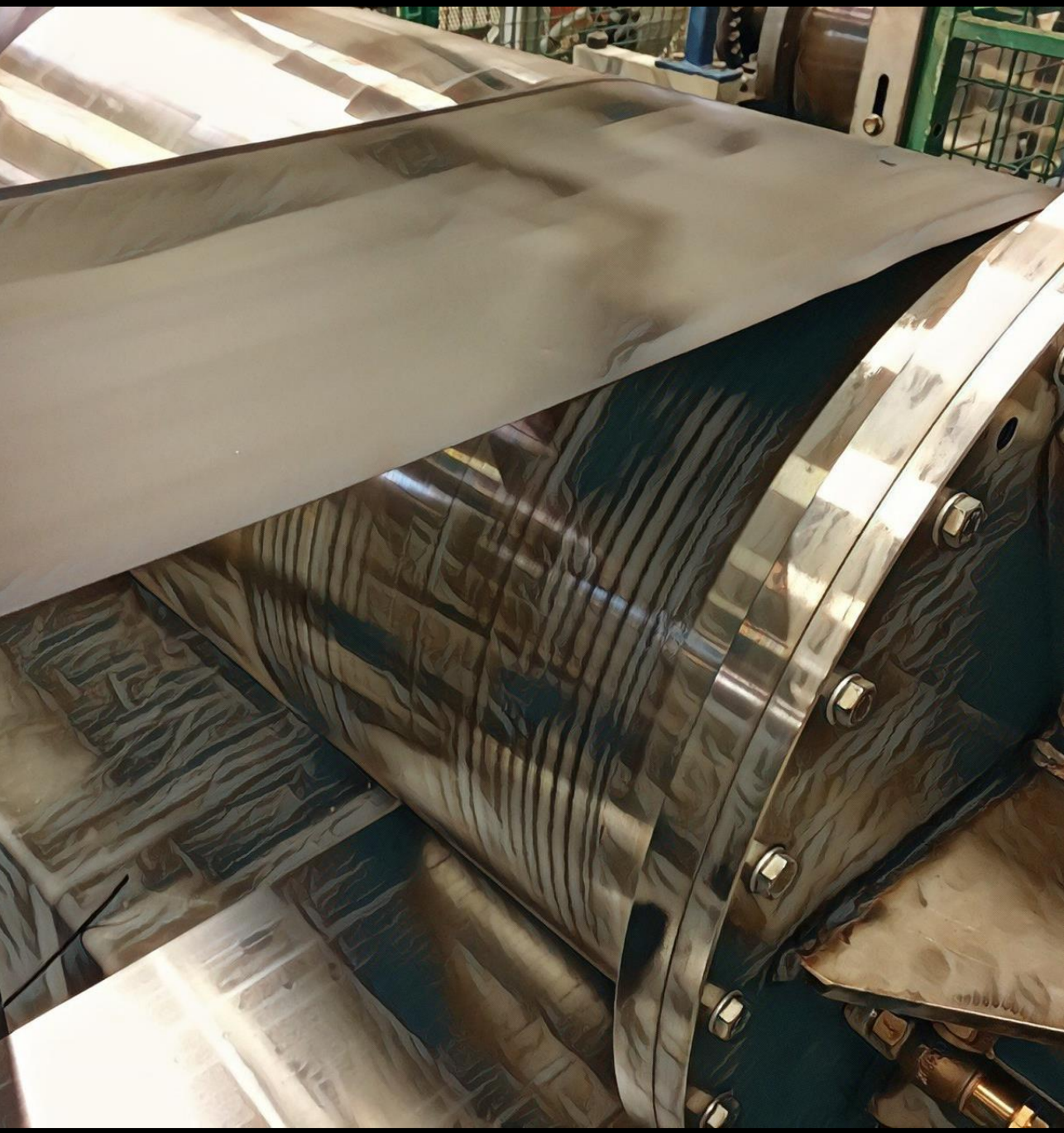

Metin Celik

Rotating Heat Pipe Assisted Annealing

Dissertation

for the purpose of obtaining the degree of doctor
at Delft University of Technology
by the authority of the Rector Magnificus prof. dr. ir. T.H.J.J. van der Hagen
chair of the Board for Doctorates
to be defended publicly on
Thursday 12 March 2020 at 12:30 o'clock

by

Metin ÇELİK

Master of Science in Sustainable Energy Technology,
Delft University of Technology, the Netherlands
born in Rize, Turkey

This dissertation has been approved by the promotors.

Composition of the doctoral committee:

Rector Magnificus,	chairperson
Prof. dr. ir. W. de Jong	Technische Universiteit Delft, promotor
Prof. dr. ir. B.J. Boersma	Technische Universiteit Delft, promotor
Independent members:	
Prof. dr. ir. P. Colonna	Technische Universiteit Delft
Prof. dr. J.M. Buchlin	The von Karman Institute for Fluid Dynamics, Belgium
Prof. dr. ir. D. Smeulders	Technische Universiteit Eindhoven
Prof. dr. ir. T.H. van der Meer	Universiteit Twente
Prof. dr. D.J.E.M. Roekaerts	Technische Universiteit Delft, reserve member
Other members:	
Dr. W.J. van der Meer	Tata Steel Europe

Keywords: rotating heat pipe, annealing, energy efficiency, heat transfer, fluid dynamics

Cover by: M. Çelik

ISBN 978-94-6402-114-1

An electronic version of this dissertation is available at
http://repository.tudelft.nl/.

Contents

Summary

Steel is an indispensable material for the sustainable maintenance and progress of modern civilization. Its versatility in terms of mechanical and thermal characteristics, corrosion resistance, raw material availability, energy consumption and recyclability provides a clear advantage in a fast-changing technological landscape. In order to adapt to the changing needs, steel production methods have been evolving and improving over time. One such improvement opportunity in terms of energy efficient production is the ”heat pipe assisted annealing” concept.

The cold rolling of steel is a process where the steel strip is cold-worked by means of rolls to achieve thickness reduction and better uniformity. This results in the strain hardening of steel. To reduce the hardness of steel and to render it more workable, it is thermally treated by heating it to a target soaking temperature and then cooling it down. This process is called annealing and it is an energy intensive process. Conventionally, heating is achieved with natural gas fired furnaces, whereas cooling is done using convective gas cooling. With this setting, the thermal energy extracted from the steel strip during the cooling stage is not used in any way. Moreover, none of the energy that is introduced during the heating stage is retained in the final product.

An alternative technology for the annealing of steel was developed at Tata Steel IJmuiden R&D with the objective of recovering and using some of the heat removed during the cooling stage and thus, achieving more energy efficient annealing. With this technology called heat pipe assisted annealing, the cooling strip is thermally linked to the heating strip with multiple rotating heat pipes. In this way, each heat pipe transfers a certain amount of heat from the cooling strip to the heating strip. Only final heating and cooling of the steel strip is carried out in a conventional way. This concept is applicable to relatively low temperature (sub-critical) annealing where the cooling rate is not crucial. Therefore, packaging steel is a good candidate for the application of this technology.

A rotating heat pipe is a highly efficient heat transfer device which is a wickless hollow cylindrical vessel rotating around its symmetric axis and containing a fixed amount of working fluid. The working fluid acts as a thermal energy carrier, transporting heat from one end of the heat pipe to the other. This basically occurs in four steps: (i) heat added to the evaporator part of the heat pipe causes the evaporation of the liquid, (ii) vapor travels to the condenser end of the heat pipe due to pressure difference, (iii) vapor condenses in the condenser section where heat is removed from the heat pipe, (iv) liquid returns to the evaporator with the help of the static pressure head and the centrifugal force induced by rotation.

The heat pipe assisted annealing concept has been patented and subsequently further studied by Tata Steel Europe R&D. A water-filled rotating heat pipe test rig integrated with steel strips provided the bulk of the prior work. This test rig served

as the proof-of-principle installation and it showed that heat can be transported from a hot strip to a cold one with a rotating heat pipe. In this context, several gaps have been identified to further acquire the knowledge on the system components, the concept performance and feasibility.

This thesis focuses on four main aspects of the fundamentals and the feasibility of the heat pipe assisted annealing concept: (i) contact heat transfer between the steel strip and the rotating heat pipe, (ii) computationally efficient modelling of the interior dynamics of a rotating heat pipe, (iii) applicable working fluids for the high temperature range, (iv) behavior of the heat pipe assisted annealing system as a whole. These aspects are studied through a thermal engineering perspective.

The heat pipe assisted annealing concept relies on the effective transfer of heat from the strip to the rotating heat pipe and vice versa. Therefore, it is important to understand the underlying physics governing this heat transfer and to be able to predict the heat transfer rate for possible configurations. In this context, in Chapter 2 of this thesis, the contact heat transfer between a steel strip and a rotating heat pipe is investigated both experimentally and numerically. The numerical model is based on first principles. It finds the thickness and the pressure of the gas layer between the strip and the heat pipe and subsequently considers different heat transfer mechanisms. The experimental work was carried out on the the proof-of-principle test rig. The model is validated with the experimental results. The contact heat transfer coefficient in the uniform region varied between 4,000 to 20,000 W/(m^2.K). It showed an increase in the contact heat transfer with decreasing strip velocity and increasing radial stress. For the considered cases, conduction through the gas layer was the dominant heat transfer mechanism. Additionally, a simplified expression has been developed for the calculation of contact heat transfer through multiple regression analysis.

The modelling of a rotating heat pipe is a crucial step for the detailed study of the heat pipe assisted annealing technology. Although modelling of rotating heat pipes has been the subject of many studies in the literature, these models are not computationally efficient enough to allow for the simultaneous modelling of multiple heat pipes linked to each other with strips. On this ground, in Chapter 3, a novel computationally efficient engineering model describing the transient behavior of the heat pipe is developed. In this model, the liquid and the vapor cells are allowed to change size radially in order to allow for the tracking of the liquid / vapor interface without the need for fine meshing or re-meshing. The model is also adapted to capillary-driven heat pipes. The model is validated with experimental and numerical studies from the literature. The deviation is computed to be around 2% with the numerical and analytical studies and around 6% with the experimental study.

The heat pipe assisted annealing concept requires the operation of heat pipes within a temperature range of 25 °C to 700 °C. In order to operate within this range, different working fluids need to be used for different temperature ranges due to constraints of vapor pressure, life time, performance and safety. These working fluids are studied in Chapter 4. First, a selection of the working fluids is made based on a literature review. This selection yielded water, Dowtherm A, phenanthrene and cesium. Then, a life time test has been carried out with thermosyphons to

test the stability of phenanthrene. At the end of a 3 months long test at 460 °C, thermal decomposition of phenanthrene was observed. However, these tests should be repeated with better initial vacuum and at multiple temperatures. Finally, Dowtherm A has been used in a rotating heat pipe setup to test its applicability and performance. It has been shown that Dowtherm A is suitable to be used in a rotating heat pipe at the designated temperature range in terms of performance, provided that annular flow is avoided.

With the knowledge gathered from the previous chapters of this thesis, a model of the heat pipe assisted annealing line has been developed in Chapter 5. The aim of this model is to quantify the energy efficiency advantage brought by the concept for different number of heat pipes and to understand the behavior of the system as a whole. The simulations were run for a fixed plant layout with varying number of heat pipes and an average wrap angle of 104°. The energy recoveries for the simulations run for a strip of 0.25 mm and a line speed of 6.133 m/s were 76.5%, 73.4%, 69.4% and 63.9% for a total number of 90, 75, 60 and 45 heat pipes, respectively. From the simulation results it follows that cesium heat pipes are more efficient than organic heat pipes. Finally, the simulation results showed that the thermal cycle requirements can be satisfied with this new technology.

Samenvatting

Staal is een onmisbaar materiaal voor het duurzame onderhoud en de vooruitgang van de moderne beschaving. Zijn veelzijdigheid met betrekking tot mechanische en thermische eigenschappen, corrosieweerstand, beschikbaarheid van grondstoffen, energieverbruik en recyclebaarheid leiden tot duidelijke voordelen in een snel veranderend technologielandschap. Staalproductiemethoden werden steeds verbeterd om aan de veranderende behoeften te voldoen. Een voorbeeld van een verbeteringsmogelijkheid wat betreft energie-efficiënte productie is het concept van de "heat pipe assisted annealing".

Het koudwalsen van staal is een proces waarbij de staalband wordt omgevormd met behulp van walsen om diktevermindering en een betere uniformiteit te bereiken. Na koud walsen wordt staal harder. Om de hardheid van staal te verminderen en het werkbaarder te maken, wordt het warmtebehandeld door het te verwarmen tot een bepaalde weektemperatuur en het vervolgens af te koelen. Dit proces wordt uitgloeien genoemd en het is een energie-intensief proces. Conventioneel wordt verwarming uitgevoerd met aardgasgestookte ovens, terwijl afkoeling wordt gerealiseerd met convectieve gaskoeling. Met dit systeem wordt de energie die tijdens het afkoelen van staalband wordt afgegeven op geen enkele manier gebruikt. Bovendien blijft in het eindproduct niets van de thermische energie die wordt toegevoegd tijdens de opwarmende fase.

Een alternatieve technologie voor het uitgloeien van staal werd ontwikkeld bij Tata Steel IJmuiden R&D. Het doel van deze technologie is een deel van de warmte (die tijdens de afkoelingsfase verwijderd wordt) te gebruiken en hiermee een energie-efficiënter uitgloeiproces te realiseren. Met behulp van deze technologie die "heat pipe assisted annealing" wordt genoemd, wordt de afkoelende staalband thermisch gekoppeld aan de opwarmende staalband door middel van meerdere roterende heat pipes. Op deze manier brengt elke heat pipe een bepaalde hoeveelheid warmte van de afkoelende strip over naar de opwarmende stallband. Alleen de laatste stadia van verwarming en afkoeling van de staalband worden op conventionele wijze uitgevoerd. Dit concept is van toepassing op gloeien bij relatief lage temperaturen (sub-kritisch) waarbij de koelsnelheid niet cruciaal is. Daarom is verpakkingsstaal een goede kandidaat voor de toepassing van deze technologie.

Een roterende heat pipe is een zeer efficiënte cilindrische warmtewisselaar zonder capillair materiaal. Het roteert rond zijn symmetrische as en het bevat een vaste hoeveelheid transportmedium. Het transportmedium werkt als een thermische energiedrager en het transporteert warmte van het ene einde van de heat pipe naar het andere. Dit gebeurt in principe in vier stappen: (i) warmte toegevoerd aan de verdamper van de heat pipe veroorzaakt de verdamping van de vloeistof, (ii) de damp stroomt naar de condensor door het drukverschil, (iii) damp condenseert in het condensorgedeelte waar warmte wordt verwijderd uit de heatpipe, (iv) vloeistof

stroomt terug naar de verdamper met behulp van de statische drukhoogte en de centrifugale kracht veroorzaakt door rotatie.

Het ”heat pipe assisted annealing”concept is gepatenteerd en vervolgens verder onderzocht door Tata Steel Europe R&D. Een roterende heat pipe testinstallatie gevuld met water en geïntegreerd met staalbanden heeft het grootste deel van het eerdere werk opgeleverd. Deze testinstallatie diende als de proof-of-principle-installatie. Hiermee werd aangetoond dat warmte kan worden getransporteerd van een warme staalband naar een koude staalband met een roterende heat pipe. In deze context zijn verschillende lacunes geïdentificeerd om de kennis over de systeemcomponenten, en de conceptprestaties en haalbaarheid te vergroten.

Dit proefschrift richt zich op vier aspecten van de basisprincipes en de haalbaarheid van het ”heat pipe assisted annealing”concept: (i) de contactwarmteoverdracht tussen de staalband en de roterende heat pipe, (ii) het modelleren van de innerlijk dynamiek van een roterende heat pipe op een rekenkundig efficiënte manier, (iii) de toepasbare transportmedia voor het hoge temperatuurbereik, (iv) het gedrag van het ”heat pipe assisted annealing”systeem in zijn geheel. Deze aspecten worden bestudeerd op basis van een thermische engineering perspectief.

Het ”heat pipe assisted annealing”concept is afhankelijk van de effectieve warmteoverdracht van de staalband naar de roterende heat pipe en omgekeerd. Daarom is het belangrijk om de onderliggende fysica van deze warmteoverdracht te begrijpen en om de warmtestroom voor potentiële configuraties te kunnen voorspellen. In deze context wordt de contactwarmteoverdracht tussen een staalband en een roterende heat pipe experimenteel en numeriek onderzocht in Hoofdstuk 2. Het numerieke model is gebaseerd op gevestigde natuurwetten. Het resulteert in de berekening van de dikte en de druk van de gaslaag tussen de staalband en de heat pipe en beschouwt vervolgens verschillende mechanismen van warmteoverdracht. Het experimentele werk werd uitgevoerd op de proof-of-principle testinstallatie. Het model is gevalideerd met de experimentele resultaten. The contactwarmteoverdrachtscoëfficiënt varieerde tussen 4,000 to 20,000 W/(m^2.K). Het toonde een toename van de contactwarmteoverdracht met afnemende bandsnelheid en toenemende radiale spanning. Voor de beschouwde gevallen was conductie door de gaslaag het dominante warmteoverdrachtsmechanisme. Bovendien is een eenvoudige uitdrukking ontwikkeld voor de berekening van contactwarmteoverdracht via multipele regressieanalyse.

Het modelleren van een roterende heat pipe is een essentiële stap voor de gedetailleerde studie van de heat pipe assisted annealing technologie. Hoewel het modelleren van roterende heat pipes meermaals werd behandeld in veel publicaties in de literatuur, zijn deze modellen niet voldoende efficiënt om meerdere heat pipes verbonden met staalbanden gelijktijdig te kunnen simuleren. Op basis hiervan in Hoofdstuk 3 wordt een nieuw computationeel efficiënt engineering model ontwikkeld. In dit model kunnen de vloeistof en de damp-cellen radiaal van grootte veranderen. Dit maakt het volgen van de vloeistof / damp-grensvlak mogelijk zonder de noodzaak van ‘fine meshing’ of ‘re-meshing’ . Het model is ook aangepast aan capillaire heat pipes. Het model is gevalideerd met experimentele en numerieke studies uit de literatuur. De afwijking wordt berekend als ongeveer 2% voor

de numerieke en analytische studies en ongeveer 6% voor de experimentele studie.

Het heat pipe assisted annealing concept vereist het opereren van heat pipes in een temperatuurbereik van 25 °C tot 700 °C. Om in dit bereik te opereren, moeten verschillende vloeistoffen worden gebruikt voor verschillende temperatuurbereiken vanwege beperkingen van dampdruk, levensduur, prestatie en veiligheid. Deze vloeistoffen worden in Hoofdstuk 4 bestudeerd. Ten eerste wordt een selectie van de vloeistoffen gemaakt op basis van een literatuuroverzicht. Water, Dowtherm A, phenanthreen en cesium zijn uiteindelijk geselecteerd. Vervolgens is een levensduurtest met thermosifonen uitgevoerd om de stabiliteit van phenanthreen te testen. Aan het einde van een test van 3 maanden bij 460 °C werd thermische ontleding van phenanthrene waargenomen. Deze tests moeten echter worden herhaald met een beter initieel vacuüm en bij meerdere temperaturen. Ten slotte is Dowtherm A gebruikt in een testinstallatie van een roterende heat pipe om de toepasbaarheid en prestatie ervan te testen. Het is aangetoond dat Dowtherm A geschikt is om te worden gebruikt in een roterende heat pipe in het geselecteerde temperatuurbereik op voorwaarde dat een ringvormig stromingspatroon wordt vermeden.

Met de kennis verzameld uit de vorige hoofdstukken van dit proefschrift is een model van de ”heat pipe assisted annealing”productielijn ontwikkeld in Hoofdstuk 5. Het doel van dit model is om de energie-efficiëntie van het concept te kwantificeren voor verschillende aantallen heat pipes, en om het gedrag van het systeem in zijn geheel te onderzoeken. De simulaties werden uitgevoerd voor een vaste installatie-indeling met een variërend aantal heat pipes en een gemiddelde warmteoverdrachtshoek van 104°. De energieterugwinning voor de simulaties voor een staalband van 0.25 mm en een bandsnelheid van 6.133 m/s waren 76.5%, 73.4%, 69.4% en 63.9% voor een totaal aantal van 90, 75, 60 en 45 heat pipes. Het is aangetoond dat cesium heat pipes efficiënter dan organische heat pipes zijn. De simulatieresultaten tonen aan dat aan de thermische cyclus vereisten kunnen worden voldaan met deze nieuwe technologie.

Preface

The heat pipe assisted annealing concept has been invented by Geert Paulussen of Tata Steel Europe R&D. It has subsequently been patented by and further developed within Tata Steel Europe R&D where substantial knowledge on the subject has been acquired. This thesis builds upon this prior knowledge.

This PhD work is part of a collaboration project between Tata Steel, TU Delft and Drever International. The assistance of the collaborating project members has been indispensable for the execution of the project. The contribution of Geert Paulussen is especially acknowledged not only for his invention but also for his guidance throughout the PhD journey. Lastly, the direct contributions of Bob Meltzer, Karthikeyan Devendran, Mrunal Patki, Vinayak Krishnan, Stefan van Leeuwen and Frederik Verbeek, all of whom worked on this project for their MSc graduation or internship studies are gratefully acknowledged.

Metin Çelik
Amsterdam, September 2019

Nomenclature

A	Area, m^2
C	Compressibility parameter
$C_1 C_6$	Coefficients of polynomial velocity profile
C^*	Normalized compressibility parameter
c	Speed of light, m/s
c_p	Specific heat, J/(kg.K)
D	Bending stiffness per unit width, N.m
d	Thickness, m
E_b	Blackbody emissive power, W/m^2
E_p	Decomposition potential, V
F	View factor
f	Correction coefficient for capillary pressure
	Friction factor
Fr	Froude number
g	Gravity, m/s^2
Gr	Grashof number
H	Dimensionless gas layer thickness
H^*	Dimensionless gas layer thickness in uniform region
$\overline{H}$	Normalized gas layer thickness
H_e	Vickers hardness, Pa
H_{fg}	Latent heat, J/kg
h	Heat transfer coefficient, $W/(m^2.K)$
	Specific enthalpy, J/kg
	Planck's constant, J.s
$\overline{h}$	Average heat transfer coefficient, $W/(m^2.K)$
$\hbar$	Gas layer thickness, m
J	Radiosity, $W/^2$
K	Wick permeability, m^2
k	Thermal conductivity, W/(m.K)
k_b	Boltzmann's constant, J/K
k_s	Harmonic mean thermal conductivity, W/(m.K)
K	Integration constant
L	Length, m
L_c	Characteristic length, m
$\mathcal{L}$	Digital level reading from infrared camera
M	Molecular weight, kg/mol
$\mathcal{M}$	Figure of merit
m	Mass, kg
	Slope of roughness peaks
$\dot{m}$	Mass flow rate, kg/s
N	Number of surfaces
Nu	Nusselt number
$\overline{\mathrm{Nu}}_{\mathrm{L_c}}$	Nusselt number based on the characteristic length
p	Pressure, Pa
p_m	Pressure required for full contact, Pa
$\mathrm{Pé}$	Péclet number
Pr	Prandtl number

$\dot{Q}$	Heat flow, W
$\dot{Q}''$	Heat flux, W/m^2
$\mathcal{R}$	Arc of curvature, m
R	Thermal resistance, K/W
$\mathcal{R}_g$	Universal gas constant, J/(mol·K)
Ra	Surface roughness, m
$\mathrm{Ra}_{\mathrm{L_c}}$	Rayleigh number based on the characteristic length
r	Radius, m
	Radial coordinate
$\mathcal{r}$	Radius of the thermal resistance, m
Re	Reynolds number
S	Stiffness parameter
	Distance between the surfaces, m
$\overline{S}$	Normalized stiffness parameter
T	Temperature, m
$\mathcal{T}$	Specific tension, Pa
t	Time, s
u	Velocity, m/s
V	Volume, m^3
v	Velocity of the node, m/s
w	Width, m
$\mathcal{Z}$	Radial distance to the node, m
z	Axial coordinate

Greek alphabet

α	Thermal diffusivity, m^2/s
β	Perturbation parameter
	Thermal expansion coefficient, 1/K
γ	Compressibility factor
	Viscous term in momentum equation, kg/(m^2·s^2)
Δ	Difference
ΔE	Electromotive force difference, V
$\Delta E°$	Standard electromotive force difference, V
Δz	Length of the node in the axial direction, m
$\Delta z'$	Distance between the adjacent node centers, m
δ_{jk}	Kronecker delta
$\overline{\delta}$	Average pulled liquid layer thickness, m
ε	Emissivity
	Porosity
η_e	Energy efficiency
κ	Wrap angle, rad
θ	Angle of the liquid pool, rad
	Angle between surface normal and line connecting surfaces, rad
Λ	Camera factor
λ	Wavelength, m
μ	Dynamic viscosity, Pa.s
ν	Kinematic viscosity, m^2/s
ξ	Extended coordinate
$\overline{\xi}$	Normalized extended coordinate
ρ	Density, kg/m^3
σ	Stefan-Boltzmann constant, W/(m^2.K^4)
	Surface tension, N/m
Φ	Angular coordinate
ϕ	Dimensionless pressure
χ	Fill ratio
Ψ	Foil bearing number

ω	Rotational speed, rad/s

Subscripts

adb	Adiabatic
c	Critical
cap	Capillary
con	Contact
$cond$	Condenser
$conv$	Convection
dz	Dead zone
ec	End cap
eff	Effective
evp	Evaporator
f	Film
fw	Furnace wall
g	Gas
hp	Heat pipe
i	Inner
j,k	Surface indices
l	Liquid
o	Outer
ph	Phase change
rad	Radiation
s	Strip
sc	Solid contact
sur	Surface
w	Wall
wk	Wick
v	Vapor
∞	Ambient

Superscripts

i	Node index
r	Radial index
z	Axial index
Φ	Angular index

Abbreviations

CDHP	Capillary-driven heat pipe
CFD	Computational fluid dynamics
CMR	Carcinogenic, mutagenic or toxic to reproduction
CP	Commercially pure
CS	Carbon steel
HF	Heat flux
HPBB	Heat pipe building block
MS	Mild steel
RHP	Rotating heat pipe
SBB	Strip building block
SS	Stainless steel
St	Stainless
TC	Thermocouple
VOF	Volume of fluid

1

Introduction

1

1.1. Steel

1.1.1. Most used metal

There is no other material than steel in the world which interacted so closely and reciprocally with the Industrial Revolution. Steel is one of the pillars of our civilization. A peek into the history of steel following the advent of the Industrial Revolution reveals why this is the case.

The demand for steel rapidly increased with the advances in new manufacturing processes introduced during the Industrial Revolution. To meet this demand, consecutive minor and major improvements were made to the production of steel. These improvements, in turn, sped up the progress in various other manufacturing processes and industries. Production of pig iron in blast furnaces was already a well-known process before the Industrial Revolution. A number of breakthroughs in iron and steel production during the revolution led to its large-scale production. A noteworthy one is the puddling process which is based on stirring the molten iron with rods allowing it to mix with air. It was introduced during the First Industrial Revolution and it increased the quality and volume of the wrought iron production. The second leap was made with the Bessemer process which involves the blowing of air into the molten iron from the bottom part of the converter. It allowed for the large-scale conversion of pig iron to steel. The Bessemer process would later be recognized as the main driver of the Second Industrial Revolution. A better alternative to the Bessemer process, the open hearth furnace, was introduced in the second half of the 19^{th} century [1–3].

Before World War I, steel already replaced iron and other metals in railways, bridges, buildings and ships. It also became indispensable for industries such as agriculture, automotive and energy supply. In the meantime, steel industry itself greatly benefited from the advances in the steel production techniques. During the World Wars, it played a major role in the arms industry. New technologies and industries required a wide range of new steel grades. Steel industry responded to the increase in the amount and quality of demand with new process developments such as new blast furnace designs, basic oxygen steelmaking and continuous casting [1–3]. After periods of ups and downs due to the two World Wars and the Great Depression, steel supply and demand accelerated again and increased in the mid-1970s. Moreover, better steel alloying practices increased the versatility of steel. The increase in steel production picked up again after 1995 [4].

A look at the present day also reveals that steel is essential to the modern world. The production of crude steel more than doubled since 1995, reaching a rate of 1.689 billion tons per year by 2017 as shown in Figure 1.1 [4]. The dependence of modern civilization on steel becomes more established with each decade. Among many others, it is used in white goods, reinforced roads, automobiles, skyscrapers, food cans, batteries, excavation machines, etc. It is by now clear that the production rate of steel is tightly linked to the economic growth of a nation [5, 6].

The clear domination of steel over other materials is a natural result of its high performance in terms of mechanical and thermal characteristics, corrosion resistance, raw materials availability, energy consumption and recyclability. While these properties secure a privileged position for steel, the patterns of material needs and

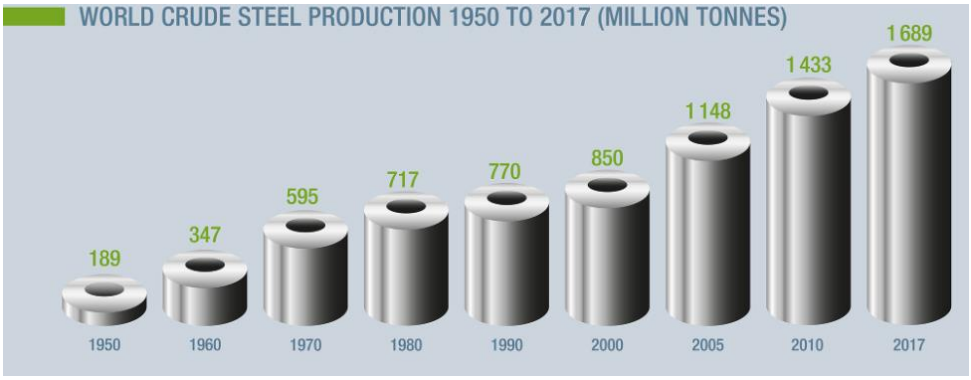

Figure 1.1: World crude steel production [4].

usage in the world are changing at an ever increasing rate [7]. To this fast-paced evolution, steel responds with its versatility. With its superior properties, adaptation to the changing needs and relatively low cost, it is guaranteed that steel will continue to be an essential material for the progress of mankind.

1.1.2. Production of steel

Steel production starts with the preparation of raw materials and includes a series of processes which lead to a variety of final products in different forms and grades. This route can be classified into two for practical purposes: 1) the upstream processes that entail the iron production, steelmaking and casting; 2) the downstream processes that comprise of rolling and finishing.

Conventionally, there are two main routes for the upstream part of the production (see Figure 1.2). The first one is called the blast furnace - basic oxygen furnace (BF-BOF) route which accounted for 71.6% of the total crude steel production in the world in 2017. The second one is called the electric arc furnace (EAF) route which was responsible for 28.0% of the crude steel output in the world in 2017. These figures are 59.7% and 40.3% for the BF-BOF and the EAF routes in the European Union, respectively [8]. These two routes are fundamentally different from each other and they should be explained separately.

The main raw materials to the BF-BOF route are iron ore and coal. Before being fed to the blast furnace for the conversion to pig iron, both of these raw materials are processed. The pyrolysis of coal in the coke oven results in the production of coke which has more favorable properties than coal for the reduction of iron ore. In addition to the coke, part of the coal is pulverized before being fed to the blast furnace. Iron ore, on the other hand, is treated in two ways: sintering and pelletizing. Both of these processes essentially provide agglomeration of iron ore. This improves the permeability and reducibility in the blast furnace [9, 10].

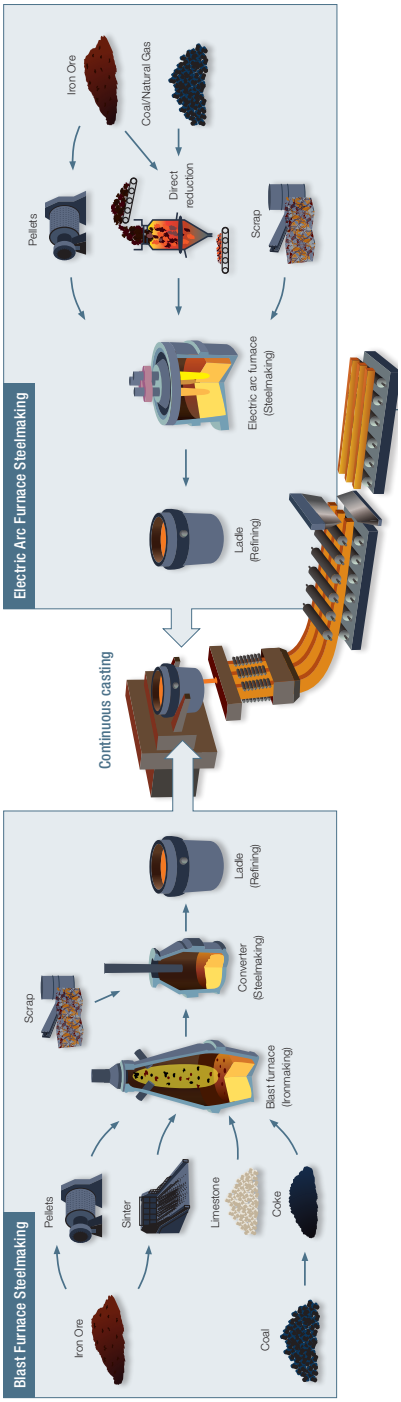

Figure 1.2: Two main routes for steelmaking [11].

The reduction of iron ore is carried out in the blast furnace. The sources of iron ore in the blast furnace are sinters, pellets and iron ore lumps. Coke and pulverized coal act as reduction agents as well as energy sources for the continuation of the process. The sources of iron ore and the reduction agents are introduced to the furnace in alternate layers along with hot air and fluxes (limestone and dolomite which help the separation of liquid iron from slag). In the furnace, in addition to the reduction of the iron ore, the melting of iron and the separation of liquid metal from the slag take place. The liquids (both liquid iron and slag) are tapped off from the bottom of the furnace. Blast furnace gas which is mainly composed of N_2, CO and CO_2 is obtained as a by-product [9, 12].

Liquid iron is transferred to the basic oxygen furnace mostly in torpedo ladles. The aim of the basic oxygen furnace is to convert the pig iron into steel by reducing the carbon content of the metal. This is accomplished by blowing pure O_2 into the metal. After the conversion is achieved, the converter is tilted and the liquid steel is transferred into the ladle. The refining of steel is continued in the ladle by the addition of alloying elements [9, 12, 13].

The other route for the steel production is the EAF route for which the input material is mainly ferrous scrap. Scrap is fed to the furnace along with fluxing agents such as lime and dolomitic lime. Melting is achieved with electric arcs and sometimes also with the help of oxygen lances and oxy-fuel burners. O_2 is fed to the liquid steel primarily for the reduction of carbon content and for increasing process efficiency. At the end of the process, liquid steel is tapped off and separated from slag [9, 10].

It should be noted that the EAF route is significantly less energy-intensive that the BF-BOF route. It results in less CO_2 emissions and it makes use of the recyclability of steel, leading to the more efficient use of resources. However, the use of EAF route is constrained by the availability of scrap as well as the demand for special products that require low residual element contamination [14, 15].

The last step of the upstream part of the production is casting which is basically described as the solidification of the liquid metal into a certain shape. In the steel industry, continuous casting became the standard method, replacing ingot casting. The transition from batches (casting ladles) to a continuous process (flow into the molds) is achieved via the tundish which is a large open container with nozzles at its bottom [16]. Liquid steel starts to solidify when it flows through the mold which is externally cooled. Once steel takes the shape of the mold, it is further guided by supporting rolls until it is finally cut into slabs [9].

The downstream part of the production starts with the reheating of slabs followed by their hot rolling. The rolling process essentially aims to reduce and level the thickness of the steel. As a general guideline, the strength of the steel decreases with increasing temperature. This suggests that steel is more easily rolled when its temperature is high. Therefore, hot rolling of steel is preceded by the reheating of slabs to around 1200 °C in furnaces [17]. The reheating of steel results in the formation of an oxide layer due to the reaction of hot steel surface with the furnace gases [18]. For this reason, the hot slab is first led to the descaler and then to the mills where the hot rolling process takes place. During hot rolling, hot steel

passes through the gap between two rolls rotating in opposite direction. The metal is deformed while passing through a series of rolls [13]. After the last set of rolls, the steel (now in the form of a strip rather than a slab) travels to the run-out-table where it is cooled with water applied to both the top and bottom surfaces [19]. It is subsequently coiled as a final product or for further processing.

In case the hot-rolled strip is further processed, it is first pickled in an acid bath in order to remove the scale on its surface. The pickled strip is sent to the cold rolling for further thickness reduction and uniformity. As the name implies, the strip is cold-worked with the help of hard work rolls and support rolls during this process [13]. This results in the strain hardening of steel [20]. In order to restore the properties of steel such as its ductility, it is heat treated either in a batch or a continuous process. This process is called annealing [21]. After annealing, the strip can be coated with a thin layer of zinc by its immersion to a zinc bath. This process is called galvanizing [22]. According to the final requirements of the product, it can also be coated with organic paintings.

1.1.3. Annealing of steel

When steel is plastically deformed by cold rolling, the grains in the metal become thinner and the number of dislocations increases. These changes in the microstructure of steel translate into an increase in its hardness. Heating the steel can initiate and advance the regrowth of the grains and can induce a reduction in the density of dislocations (see Figure 1.3). Therefore, to reduce the hardness of steel and to render it more workable, it can be thermally treated [21]. This process is called annealing.

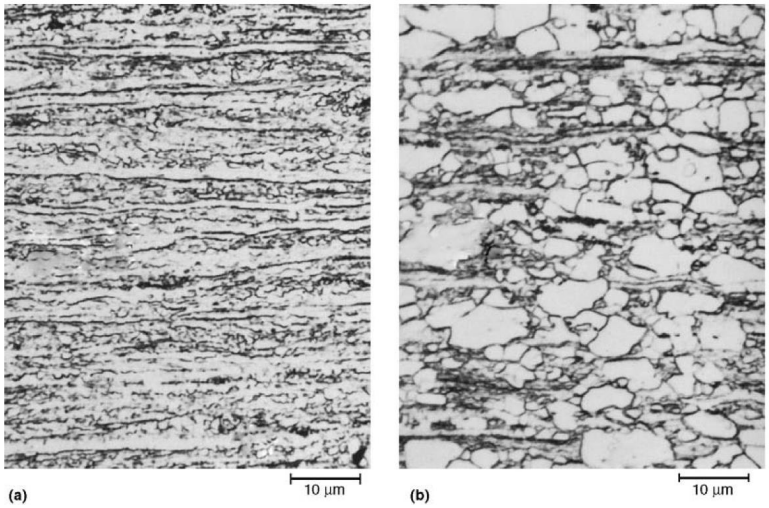

Figure 1.3: Grain growth in a cold-rolled steel following annealing at 550 °C a) for 2 min, b) for 15 min [1].

Steel is annealed either in bell-type furnaces (batch process) or in continuous

annealing furnaces (continuous process) [23]. The selection of furnace for a certain product depends on the steel grade, annealing cycle, steel quantity and overall scheduling [24]. The sketch of a typical continuous annealing furnace is shown in Figure 1.4.

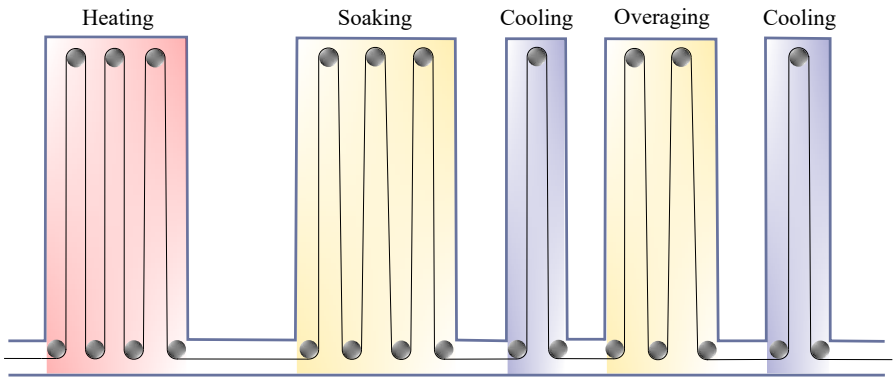

Figure 1.4: Continuous annealing furnace sketch.

Different heat treatment cycles combined with different initial conditions (ratio of carbon and other alloy elements, etc.) result in various steel grades due to phase transformation and the final composition of steel. Depending on the maximum temperature, annealing can be divided into three main categories: subcritical annealing, intercritical annealing and full annealing [24].

Subcritical annealing is carried out always below 723 °C which is the critical temperature for the onset of austenite formation. During subcritical annealing, recrystallization and grain growth are achieved. The softening rate of steel increases when the maximum temperature (soaking temperature) approaches the critical temperature. The duration of the soaking is also an important factor for the end properties of steel. The final microstructure of steel is not affected by the cooling rate [24].

Intercritical annealing takes place above the critical temperature of 723 °C where austenite begins to form. Austenite can transform back to ferrite and carbide when the steel is cooled down. Supercritical annealing, on the other hand, is performed above the upper critical temperature where full austenitization is achieved. For both the intercritical and the supercritical annealing, the cooling profile dictates the transformation to other phases and thus, it determines the final properties of the steel [24].

1.2. Heat pipe assisted annealing concept

Manufacturing of steel is very energy intensive. The average energy consumption estimated in 2016 was 20.3 GJ/t of steel produced [4]. Due to the environmental and economic consequences of this energy requirement, a central motivation of the steel industry is to improve energy efficiency. To accomplish the B2DS scenario,

1

steel industry is expected to reduce its specific final energy requirement to produce crude steel by 48% in 2060 [25].

A close look to the continuous annealing part of the production also reveals that it requires a lot of energy. The average energy consumption during continuous annealing is estimated as 1.0 GJ/t of steel annealed [26]. As a consequence, a large number of studies focused on more efficient annealing of steel through improved modelling, control and scheduling [27–34]. However, a more dramatic change in the energy consumption of the process is only possible with a paradigm shift in the design of the annealing furnace.

After the heating up of the steel strip to the soaking temperature, the energy introduced to the steel is extracted during the cooling section. The energy that is extracted during cooling has a low exergy and therefore it is not suitable for recovery. Moreover, none of the energy is retained in the steel itself. In a conventional continuous annealing line, the heating and the cooling stages are not linked to each other. In theory, thermally linking the cooling strip to the heating strip would enable a more energy efficient annealing process, as shown in Figure 1.5. This can be accomplished with one or multiple heat exchangers.

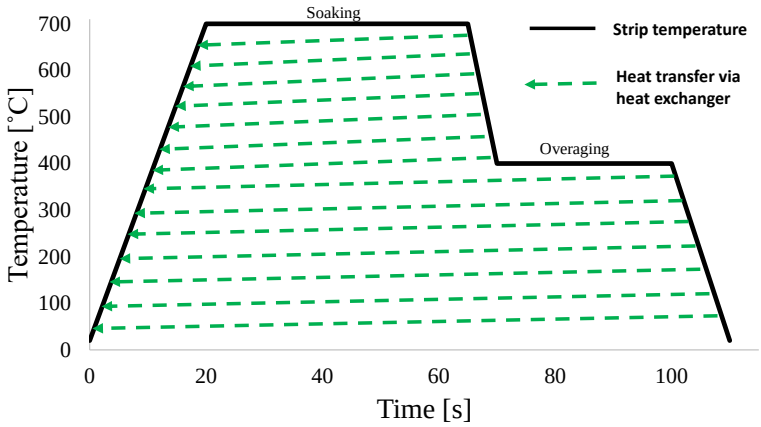

Figure 1.5: Subcritical annealing temperature profile and heat recovery.

An attempt to bring the heat from the cooling strip to the heating strip has been demonstrated by the concept called "steel strip annealing through roll regenerative furnace" by Drever International S.A. [35–37]. In this concept, the hot strip is cooled via a series of large conductive rolls which transfer the heat to a colder strip running in the counter direction. The heat transfer between the strip and the roll is achieved through contact heat transfer. The efficiency of the heat transfer depends on the contact heat transfer and thermal conductivity of the roll among many others. A schematic of this concept is shown in Figure 1.6. Although this concept successfully puts the aforementioned theory into practice, it has several limitations such as the small contact angle of the strips, thermal fatigue of the rolls and thermal imprinting of one strip to the other.

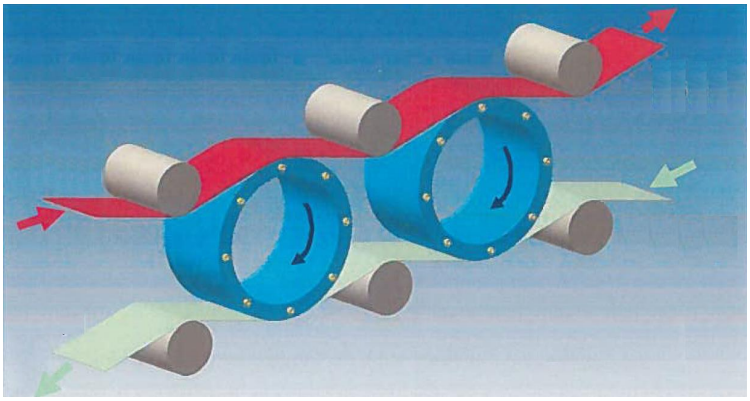

Figure 1.6: Steel strip annealing through roll regenerative furnace [36].

Therefore, an alternative technology for energy efficient annealing of steel that uses a similar principle was developed at Tata Steel IJmuiden R&D. This patented novel concept, called "heat pipe assisted annealing", aims to reduce the energy consumption to 30% of a conventional line [38]. In this concept, the heat exchanger is a rotating heat pipe which is a passive heat transfer device that makes use of a working fluid acting as an energy carrier. The strip being cooled is thermally linked to the strip being heated via multiple rotating heat pipes. The concept is shown in Figure 1.7.

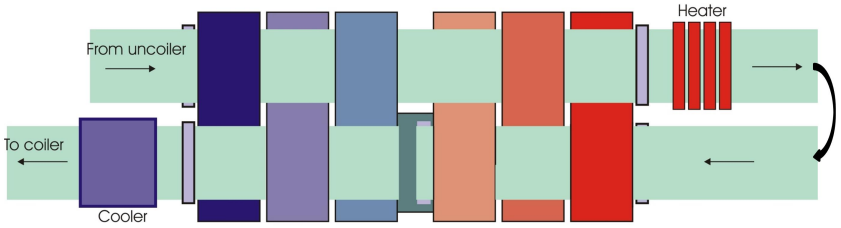

Figure 1.7: Heat pipe assisted annealing conceptual representation [39].

In the heat pipe assisted annealing concept, each heat pipe transports some of the total heat from the cooling strip to the heating strip. With a limited number of heat pipes, most of the heat can be reused in the process. In order to operate up to 700 °C, different working fluids need to be used for different temperature ranges due to constraints of vapor pressure and long-term fluid stability inside the heat pipes. Only final heating and cooling of the steel strip is performed in a conventional way. The strip being heated and the strip being cooled may be part of the same strip. In this case, the strip that is heated is reversed after the conventional heating section.

The heat pipe assisted annealing concept is suitable for the application of subcritical annealing where the cooling rate is not critical as opposed to the applications of intercritical and supercritical annealing. Therefore, the target material for this technology is selected as packaging steel.

1.3. Heat pipes

1.3.1. Working principles

A heat pipe is a highly efficient heat transfer device. It is a closed pipe which contains a fixed amount of working fluid that is fully sealed inside. The working fluid acts as a thermal energy carrier, transporting heat from one end of the heat pipe to the other [40–42]. The working principle and the sections of a heat pipe are summarized as follows in relation to Figure 1.8.

1. Heat added to the evaporator causes the liquid to evaporate and the local vapor pressure to increase.
2. Vapor travels to the condenser through the adiabatic section due to the induced pressure difference.
3. Vapor dissipates its heat in the condenser section condensing back to liquid and further promoting vapor transport due to local pressure decrease.
4. Liquid returns to the evaporator, completing the cycle.

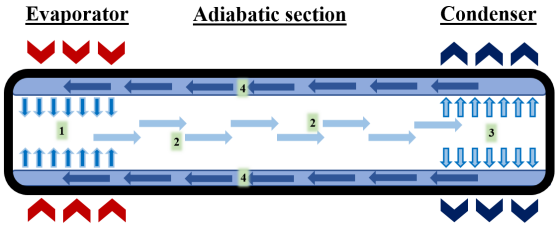

Figure 1.8: Heat pipe sections and working principle.

Various types of heat pipes deal with the transport of the liquid back to the evaporator in different ways. The most primitive type of heat pipe is the thermosyphon, where the liquid returns to the evaporator with the help of gravity. For this reason, the condenser should be located above the evaporator. This basic configuration also forms a pool of liquid at the evaporator unlike other heat pipe types. The most widely used type of heat pipe is the capillary-driven heat pipe where a wick structure is placed at the inner wall of the heat pipe. This wick structure provides a suitable environment for the liquid to return to the evaporator through capillary force. In an axially rotating heat pipe, on the other hand, the liquid returns to the evaporator by the centrifugal force and the static pressure head [42–44].

There are many other types of heat pipes (see Figure 1.9) using one or more of these principles, but differing from the aforementioned types due to their geometry

and associated characteristics. For instance, when the cross-section of the capillary-driven heat pipe is an annulus, the heat transfer area and the total capillary capacity of the heat pipe can increase. Such a heat pipe is called an annular heat pipe [45, 46]. When the heat pipe is flat and the evaporator is much smaller than the condenser which is spread out to the upper or the lower wall, it is called a vapor chamber [47]. Some heat pipes consist of a serpentine tube of capillary size and they work based on the growth and collapse of bubbles due to evaporation and condensation. These heat pipes are called oscillating or pulsating heat pipes [48]. In the loop heat pipes, on the other hand, the liquid and the vapor lines connecting the evaporator to the condenser are physically separated, creating a loop structure [49]. Some of these heat pipes are shown in Figure 1.9.

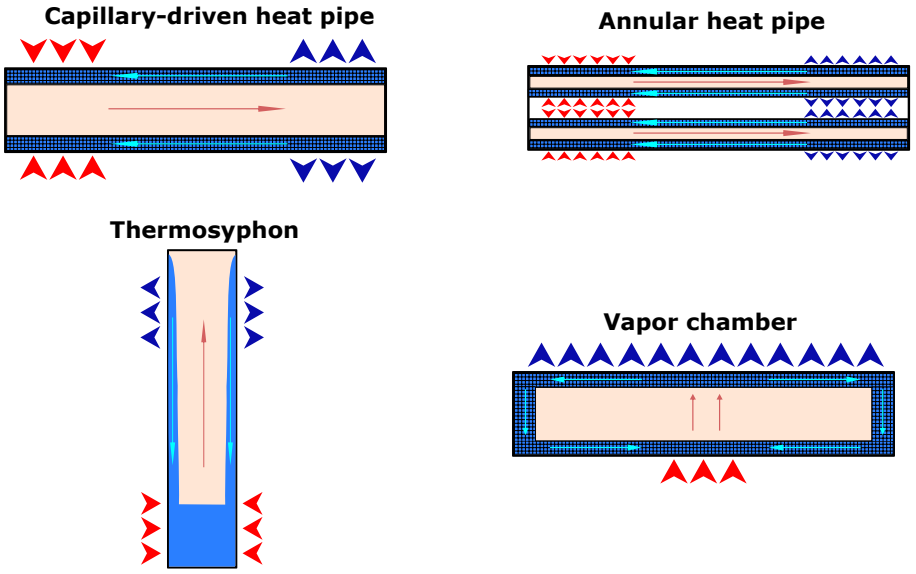

Figure 1.9: Various heat pipe types.

Heat pipes are orders of magnitude more efficient in transferring heat compared to other geometrically equivalent passive heat transfer devices such as the commercial solid thermal conductors. Moreover, they are more suitable for transient operation. There are several reasons for these advantages.

First of all, the overall thermal resistance of heat pipes remains relatively small even if the distance between the evaporator and the condenser is large. In other words, the same amount of heat can be transferred from one end of the heat pipe to the other with a rather low temperature drop. This is the case because, in addition to the conduction of heat through the wall, the wick and the liquid, heat pipes make use of the latent heat of vaporization and vapor transport to transfer heat. These two mechanisms combined result in a very low temperature gradient even though the heat transfer distance is large [50].

Second, a change in the heat flux during the operation of a conventional solid

thermal conductor results in a higher temperature change of the conductor compared to the temperature change of the heat pipe. An additional heat input to the heat pipe is partly accommodated by the increase in the rate of evaporation, without causing a large increase in the operating temperature. This is advantageous because it allows for an increase in the heat input by keeping the source temperature more or less constant [50].

Third, the heat pipes have a much faster thermal response time compared to the solid thermal conductors due to their low thermal inertia. Furthermore, the length of the heat pipe does not significantly affect the thermal response time, unlike solid thermal conductors [41].

1.3.2. Working fluid and operating range of the heat pipe

The working fluid is a critical part of the heat pipe. It should be selected with care to ensure the proper functioning of the heat pipe for a certain application. For instance, Nitrogen is reported to be a suitable working fluid for cryogenic applications between -203 to -160 °C, whereas the useful range for water is 30 to 200 °C and for Sodium it is 600 to 1,200 °C [42].

Since phase change is indispensable to the functioning of a heat pipe, the theoretical limits for the operation of a working fluid in two-phase lies between the triple point and the critical point. However, the practical operating range for a working fluid varies from this theoretical range due to the operating limits (heat transport limits at different operating temperatures) of heat pipes, lifetime of the working fluid, safety aspects, and thermophysical properties of the working fluid which influence its performance as an energy carrier.

Together with the heat pipe design, operating limits of the heat pipes strongly depend on the working fluid. The main operating limits are the viscous, sonic, entrainment, boiling and capillary limits. These limits are summarized in Figure 1.10. In order to remain inside the boundaries of these limits, the working fluid selection should be compatible with the foreseen operating temperatures and heat input / output.

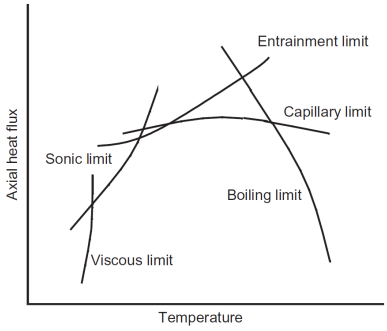

Figure 1.10: Heat pipe operating limits [42].

The viscous limit is usually reached at low vapor pressures, when the pressure difference necessary to transport the vapor from the evaporator to the condenser

is comparable in magnitude to the absolute pressure at the evaporator. In such a situation, viscous forces dominate the flow and the vapor pressure difference cannot overcome these forces. This may lead to the slow-down of the vapor flow or even to a total stagnation [41, 42, 51–53].

The sonic limit is reached when the vapor speed at the end of the evaporator approaches the speed of sound. This usually occurs when the heat pipe operates at relatively low temperature corresponding to low vapor pressure and vapor density. Since the vapor mass flow needs to be maintained to transport the heat from the evaporator to the condenser, a low vapor density results in high vapor speeds. This can significantly deteriorate the performance of the heat pipe and jeopardize the nearly-isothermal temperature distribution at the vapor region [41, 42, 51–53].

The entrainment limit occurs because the liquid and the vapor in a heat pipe flow in opposite directions. When the vapor speed is fairly high, the interfacial shear forces can exceed the surface tension forces acting on the liquid. This may hinder the flow of the liquid from the condenser to the evaporator, causing the evaporator to be devoid of liquid and therefore limiting the heat flux. As with viscous and sonic limits, entrainment is also common at relatively low temperatures [41, 42, 51–54].

The capillary limit only applies to the heat pipes using capillary force for driving the liquid from the condenser to the evaporator. When capillary pressure is not high enough to sustain sufficient amount of liquid flow to the evaporator, the evaporator can experience a dry-out leading to the failure of the heat pipe operation. To avoid this situation, the capillary pressure should be higher than the pressure losses caused by the viscous forces, phase transition and body forces [41, 42, 51–53, 55].

The boiling limit is different from the previously mentioned operating limits such that it is related to the radial flux rather than the axial flow. When the heat flux is very high and it results in excessive nucleate boiling of the liquid at the evaporator, a vapor film can form at the inner surface of the heat wall. This can significantly increase the thermal resistance of the heat pipe and lead to a significant change in its performance. In the presence of a wick structure, the vapor bubbles can hamper the liquid flowing to the evaporator [41, 42, 51–53].

The lifetime of the working fluid can be affected by two different processes which can produce undesired substances inside the heat pipe. These processes are the thermal degradation and the chemical reactions with the container / wick material of the heat pipe. Thermal degradation is relevant for the organic compounds as they can isomerize or decompose into other compounds. At increasingly high temperatures, the reaction rate increases. Some inorganic materials, on the other hand, can chemically react with the container and / or wick material [41].

These reactions can harm the performance of the heat pipe in two ways. The chemical reactions between the working fluid and the heat pipe material can lead to the formation of liquid or solid products that can deposit on the interior surface of the heat pipe [42]. More importantly, both the thermal degradation and the the reactions with the container material can result in the formation of non-condensable gases which can significantly result in the deterioration of the heat pipe performance.

During the heat pipe operation, the non-condensable gas is pushed towards the

condenser end due to the bulk vapor flow. Since it does not condense, it accumulates at the condense and diffuses towards the evaporator due to the concentration difference. Similarly, it tends to accumulate at the liquid / vapor interface due to the radial flow. This accumulation causes both a resistance to the condensation process and a decrease in the interface saturation temperature [56–58].

Safety is another crucial criterion for the selection of the working fluid. Safety aspects can be roughly divided into two. First one is the handling of the working fluid. For instance, mercury is a highly toxic material which should be handled with care. Some alkali metals, on the other hand, can react violently with air and water. The other aspect to safety is the high pressures that can form in the heat pipe. The exponential rise of vapor pressure with temperature needs to be taken into account while choosing the working fluid for a certain application and heat pipe design [42].

The thermophysical properties of the working fluid have a substantial influence on the heat pipe performance. Most important factors are summarized in Table 1.1. All these factors can be summed up with merit numbers assigned to each working fluid over a temperature range. However, it should be noted that this merit number varies for different heat pipe types [40, 42, 59].

Table 1.1: Fluid thermophysical properties affecting heat pipe performance.

Property	**Note**
Liquid viscosity	It directly affects viscous forces, thereby impacting the mass flow between condenser and evaporator.
Liquid density	A high density enables the storage of more heat in a smaller volume.
Liquid thermal conductivity	A high thermal conductivity reduces the thermal resistance through the liquid layer.
Heat of vaporization	A high heat of vaporization enables the transport of the same heat amount with a lower fluid amount.
Surface tension	Only relevant for capillary-driven heat pipes. It affects the capillary action in the wick.

1.3.3. Rotating heat pipes

A rotating heat pipe (RHP) can be simply described as a horizontally placed thermosyphon rotating around its axis of symmetry. Similar to the other types of heat pipes, it consists of three sections, namely the evaporator, the adiabatic section and the condenser. Conventionally, it does not include a wick structure. Therefore, it depends on centrifugal force to achieve working fluid circulation [41–43].

RHPs have been first proposed by Gray as an improvement to conventional heat pipes where the liquid pumping is limited by the capillary force [44]. Since its first proposal, it has been investigated in a large number of studies and has been used in various applications.

RHPs have been shown to be very effective for cooling of drill tips. In these studies, it has been shown that the integration of RHPs can minimize the usage of

cutting fluids which are seen as important sources of industrial pollution and which create technical problems such as the removal of fluid and safety [60, 61]. Similarly, rotating heat pipes have been successfully applied for the cooling of rotating electrical machines. In electric motors, for instance, thermal management is of utmost importance. Conventionally, active liquid cooling is used, however it requires complex design and it has high sealing risk. In this aspect, the use of RHPs seems to be very advantageous [62–65]. RHPs have also been investigated as an anti-icing system of the nose cones of turbofans. In this concept, the idea is to transfer the heat dissipated during the operation of the engine to the nose cone where ice accretion can occur due to subcooled water particles [66, 67].

Although applications of RHPs are not limited to the aforementioned literature sources, such applications show their effectiveness and potential for similar or various other uses.

In case the RHP has a cylindrical shape, the centrifugal force exploits the liquid head between the condenser and the evaporator to drive the liquid. In order to promote the liquid flow even more, RHPs can have a conical shape at the condenser or throughout. This conical shape inside an RHP is commonly referred to as a taper [41–43].

The performance of an RHP is affected by the combination of various factors, such as the heat pipe geometry, rotational speed, working fluid properties, fill ratio and heat transfer rate [59]. There are apparent differences between these factors and the ones affecting other types of heat pipes. Therefore, their examination can reveal crucial aspects of the RHP design and functioning.

A typical heat pipe can be considered as a network consisting of several components with different thermal resistances as seen in Figure 1.11 [43]. The same idea can be easily applied to an RHP with the wick resistances replaced by the liquid resistances.

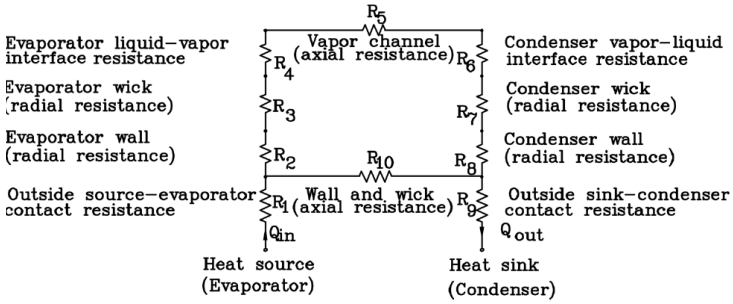

Figure 1.11: RHP as a network of thermal resistances [43].

From this perspective, the wall thermal resistances are determined by the container properties and dimensions. The vapor thermal resistance and the thermal resistances associated with phase change are usually negligible [40, 42]. The thermal resistances related to the heat transfer through the liquid layers are in most cases crucial. In a conventional heat pipe with a wick structure, these resistances

are lower because the wick structure increases the effective thermal conductivity of the liquid / wick component [68, 69]. For a rotating heat pipe, on the other hand, liquid layer thickness and working fluid properties are determining factors for the conduction heat transfer through the liquid layer. In the presence of natural convection at the evaporator, the heat transfer improves compared to the pure conduction case and the rotational speed as well as the heat flux become important factors for the thermal resistance [70–72].

Due to the importance of the liquid layer resistances, an understanding of the liquid layer distribution throughout the heat pipe is of utmost importance. In this respect, the first consideration should be the circumferential distribution of the liquid layer thickness due to the rotational speed. Flow pattern is typically estimated with the help of the Froude number ($\mathrm{Fr} = \omega^2 r/g$), a dimensionless number representing the ratio of the rotational acceleration to gravity. At relatively high rotational speeds, gravity becomes negligible compared to the centrifugal force and the liquid layer takes an annular form throughout the heat pipe. The onset of annular flow, complete annular flow and the collapse of annular flow are determined with the Critical Froude numbers which are functions of the fill ratio [73–76]. It should be noted that the calculation of critical Froude numbers does not include thermophysical properties (viscosity, surface tension, etc.) of the working fluid. However, this has been reported as the result of the previous studies rather than a simplification of the investigation [76].

When the flow pattern takes an annular form, the thermal resistance associated with the conduction through the liquid layer significantly increases. This increase is the result of a thick layer of liquid film all around the inner wall of the heat pipe. At lower rotational speeds, a pool of liquid forms at the bottom of the heat pipe and a thin layer of liquid is pulled to the upper part. This flow pattern is called rimming or stratified (see Figure 1.12). In this pattern, the thermal resistance of the liquid layer becomes lower compared to the annular flow pattern case. Although the effective area of heat transfer decreases due to the presence of the liquid pool, the thin layer of liquid provides better heat transfer efficiency [73–76]. The thickness of the thin liquid layer pulled towards to the upper part is a function of the heat pipe dimensions, rotational speed as well as the thermophysical properties of the liquid [74].

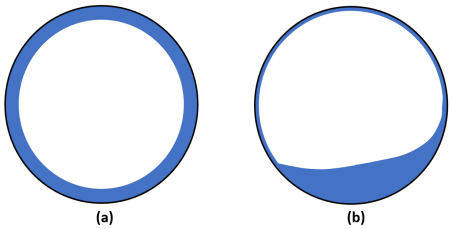

Figure 1.12: Flow patterns: a) annular, b) rimming.

For some applications, very high rotational speeds cannot be avoided or the amount of working fluid to be used needs to be limited. In these applications, the flow pattern inside the heat pipe will be annular. It is crucial that the liquid layer distribution along the axial direction of the heat pipe is calculated for these cases. This is because an optimum fill ratio should ensure that dry-out does not occur at the evaporator and at the same time it should minimize the liquid layer thermal resistance (see Figure 1.13). Moreover, for a given fill ratio and operational configuration, the viscous forces are highest when the flow is annular. This causes a larger liquid head between the evaporator and the condenser especially for low fill ratios, rendering the calculation of the axial liquid layer thickness distribution even more important.

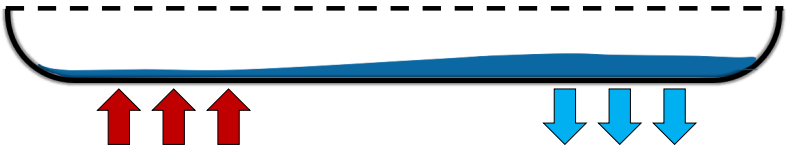

Figure 1.13: Liquid layer distribution in an RHP.

The liquid head between the evaporator and the condenser decreases with increasing rotational speed, considering that the amount of liquid transported from the condenser to the evaporator remains constant. This stems from the fact that the liquid transport is achieved through the liquid head and the rotational acceleration. When the rotational speed increases, so does the rotational acceleration, requiring less head for the same amount of liquid to be transported. Similarly, when the heat transfer increases, liquid flow rate also needs to increase. If the rotational speed remains constant, the liquid head will increase to satisfy the higher liquid flow rate. Another important aspect to consider is the effect of fill ratio when all the other parameters remain constant. If the same amount of liquid transport needs to be achieved, a larger liquid head will form if the fill ratio is lower, simply because the frictional losses will be higher for a thinner liquid film [71, 72, 77, 78].

As previously noted, the heat transfer through the liquid layer at the condenser section is limited to pure conduction. However, natural convection can play a role at the evaporator, significantly improving the heat transfer. Natural convection starts to play a role when the Rayleigh number, which allows for the comparison of natural convection to thermal conduction in a fluid layer, becomes sufficiently high (typically above 400). Natural convection is enhanced for higher fill ratios, heat fluxes and rotational speeds [70–72]. The enhancement of natural convection with higher fill ratios (thus with higher liquid film thickness) is especially important since an increase in the fill ratio leads to a significant change in the condenser thermal resistance whereas the thermal resistance at the evaporator is not as nearly influenced [70].

Among many potential improvements that can be made to the geometry of the RHP, two of them stand out by their simplicity and effectiveness. Both of these changes aim to reduce the liquid layer thickness at the condenser section, thereby

improving the heat transfer efficiency. The first one, and maybe the more common one, is the addition of a taper throughout the condenser section. The taper provides an artificial head that helps pump the liquid to the evaporator section. This reduces the liquid layer thickness at the condenser side and the associated thermal resistance [59, 79–82]. The second improvement is the addition of a chamber to the evaporator section (also called stepped-wall RHP). The presence of a chamber at the evaporator enables the accumulation of the liquid at the evaporator and in this way, it decreases the risk of a dry-out. This is advantageous because a lower amount of working fluid can be obtained at the condenser without risking an operational failure [75, 83, 84]. The accumulation of the working fluid at the evaporator also exploits the enhancement of natural convection with increasing liquid film thickness and thus, keeping the overall thermal resistance low.

1.4. Scope and objectives

The heat pipe assisted annealing concept has been patented and subsequently studied by Tata Steel Europe R&D. These studies mainly focused on proving the concept numerically as well as experimentally. The experimental setup which provided the bulk of the prior work is a water-filled rotating heat pipe with integrated steel strips. The primary aim of the proof-of-principle installation was to show that heat can be transported from a hot strip to a cold one with a rotating heat pipe. Moreover, some studies on strip tracking, strip tension development, heat transfer efficiency, heat transfer uniformity and heat pipe functioning.

These previous studies demonstrated that the concept works. However, to pave the way to a good understanding of the line concept with multiple heat pipes, several issues and gaps should be addressed. In this regard, a collaboration project between Tata Steel Europe, Drever International and TU Delft has been formed. The aim of this collaboration is to further the knowledge on the system components and the concept performance and feasibility.

The main objective of this thesis is to study the fundamentals and the feasibility of the heat pipe assisted annealing concept through a thermal engineering perspective. Although several other studies on strip tension, strip tracking and economic feasibility have been carried out by the project collaboration in parallel, they are not part of this thesis. In this regard, the research questions of this thesis are listed below.

1. What are the underlying physics governing the heat transfer between a moving steel strip and a rotating heat pipe and how can this be quantified?

2. How can one develop a transient rotating heat pipe model which provides sufficient details about its interior dynamics without experiencing long computational times?

3. What are the applicable working fluids for the high temperature range (150 °C to 700 °C) of the heat pipe assisted annealing concept?

4. What is the energy efficiency brought by the heat pipe assisted annealing

concept for different number of heat pipes and how does the system behave as a whole?

1.5. Outline

The research questions specified in the previous section are addressed in four chapters followed by an additional chapter with concluding remarks. The chapters are organized as follows:

In Chapter 2, the heat transfer between a steel strip and a rotating heat pipe is investigated. This investigation includes the development of an analytical model, the validation of the model with experiments and a parametric study of the results.

In Chapter 3, a transient numerical model describing the dynamics of a cylindrical rotating heat pipe is developed. The numerical model is also adapted to conventional capillary-driven heat pipes. The model is validated with data from the published literature and the results are discussed.

Chapter 4 focuses on the applicable working fluids for the high temperature range. The work comprises of the selection of suitable working fluids, followed by rotating heat pipe experiments with one of the selected working fluids and the experiments performed to determine the stability of working fluids.

Chapter 5 describes the modelling of the heat pipe assisted annealing line, which is basically a furnace enclosing a series of rotating heat pipes integrated with steel strips. Based on the requirements and the concept layout, the technical feasibility and the energy savings for various configurations are evaluated.

Finally, Chapter 6 reflects back on the main objective and sub-objectives. The learnings from this thesis work are summarized and a number of recommendations for further research are made.

References

[1] V. Smil, *Still the iron age: iron and steel in the modern world* (Butterworth-Heinemann, 2016).

[2] World Steel Association, *The white book of steel* (World Steel Association, 2012).

[3] D. Schauwinhold, M. Toncourt, R. Steffen, D. Janke, K. Schäfer, H. Jacobi, R. Hammer, R. Hentrich, L. Kucharcik, H. Wiegels, *et al.*, *Ullmann's Encyclopedia of Industrial Chemistry: Steel* (Wiley Online Library, 1994).

[4] World Steel Association, *World steel in figures 2018,* https://www.worldsteel.org/en/dam/jcr:f9359dff-9546-4d6b-bed0-996201185b12/World+Steel+in+Figures+2018.pdf (accessed: 2019-02-01).

[5] G. Dobrotă and C. Căruntu, *The analysis of the correlation between the economic growth and crude steel production in the period 1991-2011,* Metalurgija **52**, 425 (2013).

[6] L. Wårell and A. Olsson, *Trends and developments in the intensity of steel use: an econometric analysis,* in *Securing the Future & ICARD: 23/06/2009-26/06/2009* (Curran Associates, Inc., 2009).

[7] F. A. A. Crane, J. A. Charles, and J. Furness, *Selection and use of engineering materials* (Elsevier, 1997).

[8] World Steel Association, *Steel statistical yearbook 2018,* https://www.worldsteel.org/en/dam/jcr:e5a8eda5-4b46-4892-856b-00908b5ab492/SSY_2018.pdf (accessed: 2019-03-01).

[9] R. Remus, M. A. Aguado-Monsonet, S. Roudier, and L. Delgado Sancho, *Jrc reference report,* Best Available Techniques (BAT) Reference Document for Iron and Steel Production, Industrial Emissions Directive **75** (2010).

[10] P. Cavaliere and A. Silvello, *Ironmaking and steelmaking processes*, Vol. 173 (Springer, 2016).

[11] World Steel Association, *Overview of the steelmaking process,* https://https://www.worldsteel.org/en/dam/jcr:177c8e5c-e02a-4e08-9dc6-cce7372b41c2/Overview+of+the+Steelmaking+Process_poster.pdf (accessed: 2019-04-01).

[12] A. Ghosh and A. Chatterjee, *Iron making and steelmaking: theory and practice* (PHI Learning Pvt. Ltd., 2008).

[13] G. Béranger, G. Henry, and G. Sanz, *The book of steel,* Intercept Limited, P. O. Box 716, Andover, Hampshire SP 10 1 YG, UK, 1996. 1390 (1996).

[14] M. Yellishetty, G. M. Mudd, P. G. Ranjith, and A. Tharumarajah, *Environmental life-cycle comparisons of steel production and recycling: sustainability issues, problems and prospects,* Environmental science & policy **14**, 650 (2011).

[15] K. He and L. Wang, *A review of energy use and energy-efficient technologies for the iron and steel industry,* Renewable and Sustainable Energy Reviews **70**, 1022 (2017).

[16] Y. Sahai, *Tundish technology for casting clean steel: a review,* Metallurgical and Materials Transactions B **47**, 2095 (2016).

[17] W.-H. Chen, Y. Chung, and J. Liu, *Analysis on energy consumption and performance of reheating furnaces in a hot strip mill,* International Communications in Heat and Mass Transfer **32**, 695 (2005).

[18] J. H. Jang, D. E. Lee, M. Y. Kim, and H. G. Kim, *Investigation of the slab heating characteristics in a reheating furnace with the formation and growth of scale on the slab surface,* International Journal of Heat and Mass Transfer **53**, 4326 (2010).

[19] S.-J. Chen and A. A. Tseng, *Spray and jet cooling in steel rolling,* International Journal of Heat and Fluid Flow **13**, 358 (1992).

[20] I. Shakhova, V. Dudko, A. Belyakov, K. Tsuzaki, and R. Kaibyshev, *Effect of large strain cold rolling and subsequent annealing on microstructure and mechanical properties of an austenitic stainless steel,* Materials Science and Engineering: A **545**, 176 (2012).

[21] J. D. Verhoeven, *Steel metallurgy for the non-metallurgist* (ASM International, 2007).

[22] V. Kuklík and J. Kudlacek, *Hot-dip galvanizing of steel structures* (Butterworth-Heinemann, 2016).

[23] H. Pfeifer, *Industrial furnaces for steel processing–90 years of continuous improvement,* steel research international **89**, 1800306 (2018).

[24] J. Dossett and G. E. Totten, *ASM Handbook: Steel Heat Treating, Fundamentals and Processes*, Vol. 4A (ASM International, 2013).

[25] *International energy agency, Energy technology perspectives 2017, Catalysing energy technology transformations,* https://www.oecd.org/about/publishing/Corrigendum_EnergyTechnologyPerspectives2017.pdf, (accessed: 2019-03-01).

[26] J. A. Moya and N. Pardo, *The potential for improvements in energy efficiency and co2 emissions in the eu27 iron and steel industry under different payback periods,* Journal of Cleaner Production **52**, 71 (2013).

[27] S. Zareba, A. Wolff, and M. Jelali, *Mathematical modelling and parameter identification of a stainless steel annealing furnace,* Simulation Modelling Practice and Theory **60**, 15 (2016).

[28] N. Hajaliakbari and S. Hassanpour, *Analysis of thermal energy performance in continuous annealing furnace,* Applied Energy **206**, 829 (2017).

[29] H. Wu, R. Speets, F. Heeremans, O. Ben Driss, and R. Van Buren, *Non-linear model predictive control of throughput and strip temperature for continuous annealing line,* Ironmaking & Steelmaking **42**, 570 (2015).

[30] H. Wu, B. van Benschop, O. B. Driss, F. Frinking, and R. Speets, *Furnace combustion and control renovation to improve the productivity of a continuous annealing line,* Energy Procedia **120**, 454 (2017).

[31] M. Niederer, S. Strommer, A. Steinboeck, and A. Kugi, *Nonlinear model predictive control of the strip temperature in an annealing furnace,* Journal of Process Control **48**, 1 (2016).

[32] M. Niederer, S. Strommer, A. Steinboeck, and A. Kugi, *A simple control-oriented model of an indirect-fired strip annealing furnace,* International Journal of Heat and Mass Transfer **78**, 557 (2014).

[33] A. Sanz-Garcia, F. Antonanzas-Torres, J. Fernández-Ceniceros, and F. Martinez-de Pison, *Overall models based on ensemble methods for predicting continuous annealing furnace temperature settings,* Ironmaking & Steelmaking **41**, 51 (2014).

[34] S. Sahay and P. Kapur, *Model based scheduling of a continuous annealing furnace,* Ironmaking & steelmaking **34**, 262 (2007).

[35] J. M. Raick, *Method, device and system for the heat treatment of a moving metal strip,* (2010), US Patent App. 12/668,534.

[36] M. Renard and J.-M. Buchlin, *Energy efficient strip annealing through roll regenerative furnace,* Energy Procedia **120**, 380 (2017).

[37] J.-M. Buchlin, M. Delsipé, P. Planquart, and M. Renard, *Contact conductance determination using infrared thermography,* in *12th Int. Conf. on Quantitative InfraRed Thermography* (2014).

[38] C. T. Paulussen, G, *Heat pipe assisted strip treatment,* (2011), patent WO 2011012257 A1.

[39] G. Paulussen, *Tata Steel Europe R&D internal document,* (2009).

[40] Z. Zuo and A. Faghri, *A network thermodynamic analysis of the heat pipe,* International Journal of Heat and Mass Transfer **41**, 1473 (1998).

[41] G. P. Peterson, *An introduction to heat pipes: modeling, testing, and applications* (Wiley, 1994).

[42] D. Reay, R. McGlen, and P. Kew, *Heat pipes: theory, design and applications* (Butterworth-Heinemann, 2013).

[43] A. Faghri, *Review and advances in heat pipe science and technology,* Journal of heat transfer **134**, 123001 (2012).

[44] V. H. Gray, *The rotating heat pipe-a wickless, hollow shaft for transferring high heat fluxes.* (1969).

[45] A. Faghri and S. Thomas, *Performance characteristics of a concentric annular heat pipe: Part i—experimental prediction and analysis of the capillary limit,* Journal of heat transfer **111**, 844 (1989).

[46] A. Faghri, *Performance characteristics of a concentric annular heat pipe: Part ii—vapor flow analysis,* Journal of Heat Transfer **111**, 851 (1989).

[47] B. Xiao and A. Faghri, *A three-dimensional thermal-fluid analysis of flat heat pipes,* International Journal of Heat and Mass Transfer **51**, 3113 (2008).

[48] Y. Miyazaki, F. Polasek, and H. Akachi, *Oscillating heat pipes*, Tech. Rep. (SAE Technical Paper, 2000).

[49] Y. F. Maydanik, *Loop heat pipes,* Applied thermal engineering **25**, 635 (2005).

[50] G. Y. Eastman, *The heat pipe,* Scientific American **218**, 38 (1968).

[51] P. Nemec, A. Čaja, and M. Malcho, *Mathematical model for heat transfer limitations of heat pipe,* Mathematical and Computer Modelling **57**, 126 (2013).

[52] C. Busse, *Theory of the ultimate heat transfer limit of cylindrical heat pipes,* International Journal of Heat and Mass Transfer **16**, 169 (1973).

[53] C. Tien, *Fluid mechanics of heat pipes,* Annual review of fluid mechanics **7**, 167 (1975).

[54] C. Tien and K. Chung, *Entrainment limits in heat pipes,* Aiaa Journal **17**, 643 (1979).

[55] M. G. Mwaba, X. Huang, and J. Gu, *Influence of wick characteristics on heat pipe performance,* International journal of energy research **30**, 489 (2006).

[56] J. Huang, J. Zhang, and L. Wang, *Review of vapor condensation heat and mass transfer in the presence of non-condensable gas,* Applied thermal engineering **89**, 469 (2015).

[57] D. K. Edwards and B. D. Marcus, *Heat and mass transfer in the vicinity of the vapor-gas front in a gas-loaded heat pipe,* Journal of Heat Transfer **94**, 155 (1972).

[58] W. Anderson, R. Bonner, P. Dussinger, J. Hartenstine, D. Sarraf, and I. Locci, *Intermediate temperature fluids life tests-experiments,* in *5th International Energy Conversion Engineering Conference and Exhibit* (2007) p. 4808.

[59] C. Harley and A. Faghri, *Two-dimensional rotating heat pipe analysis,* Journal of Heat Transfer **117**, 202 (1995).

[60] T.-C. Jen, Y.-M. Chen, and G. Gutierrez, *Thermal performance of heat pipe drill: experimental study,* in *ASME 2003 Heat Transfer Summer Conference* (American Society of Mechanical Engineers, 2003) pp. 87–93.

[61] T. Jen, G. Gutierrez, S. Eapen, G. Barber, H. Zhao, P. Szuba, J. Labataille, and J. Manjunathaiah, *Investigation of heat pipe cooling in drilling applications.: part i: preliminary numerical analysis and verification,* International Journal of Machine Tools and Manufacture **42**, 643 (2002).

[62] R. Ponnappan, Q. He, J. Leland, R. Ponnappan, Q. He, and J. Leland, *Test results of a high speed rotating heat pipe,* in *32nd Thermophysics Conference* (1997) p. 2543.

[63] R. Ponnappan and J. Leland, *Rotating heat pipe for cooling of rotors in advanced generators,* in *6th Joint Thermophysics and Heat Transfer Conference* (1994) p. 2033.

[64] M. Kukharskii, *Closed evaporative cooling of rotating electrical machines,* Journal of engineering physics **27**, 1090 (1974).

[65] M. Groll, H. Krahling, and W. Munzel, *Heat pipes for cooling of an electric motor,* Journal of Energy **2**, 363 (1978).

[66] S. Gilchrist, D. Ewing, and C. Ching, *On the design of an aero-engine nose cone anti-icing system using a rotating heat pipe,* Journal of Thermal Science and Engineering Applications **1**, 022002 (2009).

[67] W. Lian and Y. Xuan, *Experimental investigation on a novel aero-engine nose cone anti-icing system,* Applied Thermal Engineering **121**, 1011 (2017).

[68] C. Ferrandi, F. Iorizzo, M. Mameli, S. Zinna, and M. Marengo, *Lumped parameter model of sintered heat pipe: Transient numerical analysis and validation,* Applied Thermal Engineering **50**, 1280 (2013).

[69] A. B. Solomon, K. Ramachandran, L. G. Asirvatham, and B. Pillai, *Numerical analysis of a screen mesh wick heat pipe with cu/water nanofluid,* International Journal of Heat and Mass Transfer **75**, 523 (2014).

[70] F. Song, D. Ewing, and C. Ching, *Fluid flow and heat transfer model for high-speed rotating heat pipes,* International Journal of Heat and Mass Transfer **46**, 4393 (2003).

[71] F. Song, D. Ewing, and C. Ching, *Experimental investigation on the heat transfer characteristics of axial rotating heat pipes,* International Journal of Heat and Mass Transfer **47**, 4721 (2004).

[72] F. Song, D. Ewing, and C. Ching, *Heat transfer in the evaporator section of moderate-speed rotating heat pipes,* International journal of heat and mass transfer **51**, 1542 (2008).

[73] L. Lin and M. Groll, *Critical conditions for collapse of annular flow in a rotating heat pipe with a cylindrical wall,* Heat transfer engineering **17**, 29 (1996).

[74] L. Lin and A. Faghri, *Heat transfer analysis of stratified flow in rotating heat pipes with cylindrical and stepped walls,* International journal of heat and mass transfer **40**, 4393 (1997).

[75] L. Lin and A. Faghri, *Condensation in rotating stepped wall heat pipes with hysteretic annular flow,* Journal of thermophysics and heat transfer **12**, 94 (1998).

[76] J. Baker, T. Oliver, L. Lin, R. Ponnapan, and J. Leland, *Correlations of critical froude number for annular-rimming flow in rotating heat pipes,* Journal of fluids engineering **123**, 909 (2001).

[77] R. Bertossi, N. Guilhem, V. Ayel, C. Romestant, and Y. Bertin, *Modeling of heat and mass transfer in the liquid film of rotating heat pipes,* International Journal of Thermal Sciences **52**, 40 (2012).

[78] H. Hassan and S. Harmand, *Effect of using nanofluids on the performance of rotating heat pipe,* Applied Mathematical Modelling **39**, 4445 (2015).

[79] H. Li, C. Liu, and M. Damodaran, *Analytical study of the flow and heat transfer in a rotating heat pipe,* Heat Recovery systems and CHP **13**, 115 (1993).

[80] T. Daniels and F. Al-Jumaily, *Investigations of the factors affecting the performance of a rotating heat pipe,* International Journal of Heat and Mass Transfer **18**, 961 (1975).

[81] R. Ponnappan, Q. He, and J. E. Leland, *Test results of water and methanol high-speed rotating heat pipes,* Journal of thermophysics and heat transfer **12**, 391 (1998).

[82] W. Lian, W. Chang, and Y. Xuan, *Numerical investigation on flow and thermal features of a rotating heat pipe,* Applied Thermal Engineering **101**, 92 (2016).

[83] L. Lin, *Cellular flow in a rotating heat pipe with stepped wall,* Heat Recovery Systems and CHP **11**, 63 (1991).

[84] M. Xie, Z. Xue, W. Qu, and W. Li, *Experimental investigation of heat transfer performance of rotating heat pipe,* Procedia Engineering **99**, 746 (2015).

2

Contact heat transfer between a steel strip and a rotating heat pipe

Part of this chapter has been published as:

1. M. Celik, K. Devendran, G. Paulussen, P. Pronk, F. Frinking, W. de Jong, and B. J. Boersma, *Experimental and numerical investigation of contact heat transfer between a rotating heat pipe and a steel strip*, International Journal of Heat and Mass Transfer, **122**, 529-538 (2018).
2. M. Celik, M. Patki, G. Paulussen, W. de Jong, and B. J. Boersma, *Dynamic Modelling of the Heat Pipe Assisted Annealing Line*, Journal of Heat Transfer, **141**(9), 091801 (2019).

2.1. Problem definition

The heat pipe assisted annealing line can be considered as a collection of building blocks comprising of one rotating heat pipe (RHP) and two strips wrapped around the heat pipe. A building block can be seen as a network of thermal resistances. Each thermal resistance causes a temperature drop when the heat is transferred from the hot strip to the cold strip. An example of such resistance network and typical shares of the individual resistances in the system can be seen in Figure 2.1. The relative importance of the resistances will vary for different designs and conditions. However, initial observations in the proof-of-principle test rig (see Figure 2.2) showed that the contact thermal resistance between the strip and the roll is not negligible.

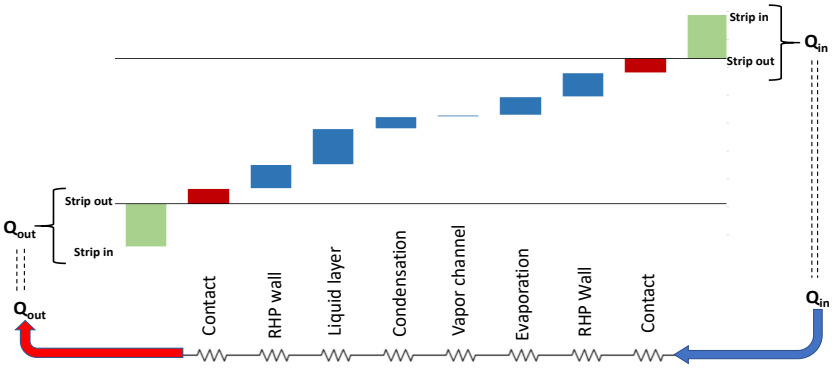

Figure 2.1: Building block as a network of resistances and exemplary shares of the individual resistances.

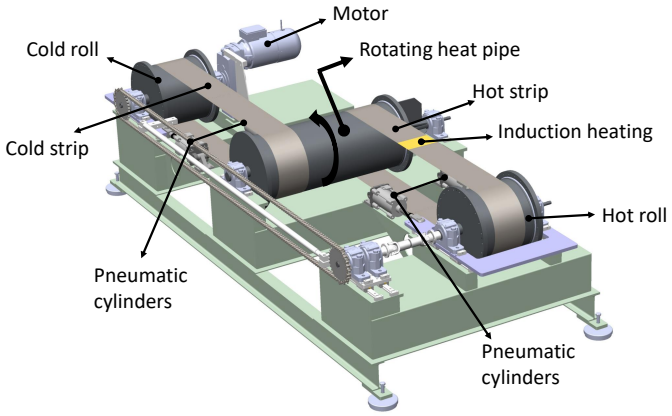

Figure 2.2: CAD view of the experimental setup.

When a strip is transported over a roll, gas is dragged in between these two surfaces. The gas compresses and forms a stable thin gas layer over the wrap angle. The gas layer forms a thermal resistance between the strip and the roll, thus limiting the heat transfer from one to the other. In the light of this information, this chapter addresses the following research question:

> *What are the underlying physics governing the heat transfer between a moving steel strip and a rotating heat pipe and how can this be quantified?*

On this ground, the current study aims to model and experimentally investigate the heat transfer between a steel strip and a rotating roll for possible configurations (strip speed, tension, RHP size, etc.) in the heat pipe assisted annealing line.

2.2. Literature review

The thickness of a gas layer between two surfaces moving at relative speed has been extensively studied in the context of foil bearings. However, these studies do not consider heat transfer between the surfaces and do not describe cases where relative motion is zero or near zero.

In the foil bearing studies, it has been observed that, with the exception of inlet and outlet region, a uniform gas layer thickness forms when the foil tension, foil width and the wrap angle are sufficiently large. This is explained by the compression of the entrained gas, finally reaching a pressure that is exactly counterbalanced by the ambient pressure and the strip tension [1, 2]. The presence of the uniform region renders the division of the problem into an inlet and outlet region possible. This approach allows for an asymptotic convergence of the inlet and outlet regions to the uniform gas layer thickness. A number of studies exploited this characteristic and offered analytical solutions to the estimation of the gas layer thickness between a stationary roll and a moving foil.

The most basic case is to consider the foil as infinitely wide and perfectly flexible and the gas as incompressible. These assumptions have been adopted Eshel et al. and the gas layer thickness for entrance and exit regions have been calculated with the help of perturbation theory [3]. Following this study, the assumptions were removed one by one and the solution methods have been reported in subsequent articles. For thick foils with high Young's modulus, the stiffness of the foil is taken into account and it is integrated into the solution [4, 5]. The numerical solution for compressing the gas layer is also provided, demonstrating that for most foil bearing applications, the assumption of incompressible fluid can be kept [6]. The effect of side leakage is shown to play a role when the gas layer thickness is large and the width of the strip is small. In the same study, web permeability is also investigated [7]. A review of these studies is provided by Wildmann [8].

For the specific case where the tension of the foil and the wrap angle is small, the problem can be solved at once, without dividing it into an inlet and an outlet branch [9–14]. This method also allows for the tension change due to friction between the foil and the roll over the wrap angle. In these studies, the foil is in physical contact

with the roll. The governing equations are solved numerically, without the use of perturbation theory, in contrast to the previously mentioned studies. Numerical methods to solve the coupled non-linear partial differential equations allowed for the study of various other geometries. The air entrainment is studied for a strip and a grooved roller by Ducotey et al. following the finite-difference method [15]. It is shown that grooved rollers can decrease the pressure build-up. Similar conclusions have been obtained by Kasikci et al [16]. A finite-difference study for a convex-roller is conducted by Jeenkour [17].

In addition to the determination of the gas layer thickness, the heat transfer between two macroscopically conforming surfaces should be studied for the problem at hand. Heat transfer between two rough surfaces is divided into the heat transfer across the gas gap and the heat transfer through solid contact. The complexity of the gap geometry can be overcome by simplifying the gap heat transfer as the heat transfer between the projected surfaces. The solid heat transfer is then determined using a correlation including contact pressure, surface parameters and thermal conductivities [18]. Results of analytical and experimental studies for the thermal resistance of gases are presented by Springer for various cases with different degree of rarefaction [19]. It is shown that the Navier-Stokes equations and the Fourier heat conduction laws are valid for most common cases where the number of collisions between the molecules is large compared to the number of collisions between the molecules and the body. The thermal gap conductance theory provided in the previous studies [18, 19] is experimentally studied and validated [20]. A comprehensive review of the subject is provided by Yovanovich [21].

The experimental investigation of contact heat transfer between a strip and a roll has not been widely addressed so far. One of the few studies concerns a dedicated roll regenerative furnace [22, 23]. In that study, a hollow shell is used as the roll and the strip velocities are relatively low. The contact heat transfer coefficient values that were reported are used in the modelling of a multi-roll heat exchanger with two strips moving in opposite direction [24].

2.3. Analytical model description

In the modelling part of this work, a novel methodology for quantifying the heat transfer is adopted. Since there is no straightforward way to calculate the heat transfer between two moving surfaces, the problem is divided into a gas entrainment and a heat transfer part.

The gas layer thickness between the two surfaces is found with an asymptotic approach. The asymptotic approach is based on dividing the problem into two parts (entry and exit regions) and integrating outward from a uniform region to the entry and exit regions. The asymptotic approach can be used because the wrap length is large enough to form a uniform gap region. The stiffness of the strip, the contact between the surfaces and the compressibility of the gas are incorporated in the model. The side leakage, on the other hand, is negligible for the considered cases and thus, it is not accounted for in the model. The model therefore is a combination of the approaches found in [5], [6] and [10]. However, the derivation of the governing equations is somewhat different. The solution for gas layer and

contact pressure is coupled with the contact heat transfer model described in [18]. With this combination, the contact heat transfer coefficient evolution along the wrap angle is found.

The analysis for the steel strip transported over a rotating heat pipe is simplified to the study of a strip traveling over a roll. The infinitely wide strip travels at velocity u_s and is tensioned with $\mathcal{T}_s$ over the roll radius r_o. The heat pipe is considered to be non-deformable whereas the strip can bend depending on the forces acting on it. As the heat pipe is freely suspending, its velocity is assumed to be equal to the velocity of the strip. The absolute pressure of the gas layer is p_g and its thickness is $\hbar$. The wrap angle is divided into three regions; namely the inlet region (A), the uniform region (B) and the outlet region (C). Tension on the strip is applied some distance away from the roll marked as (D) (see Figure 2.3).

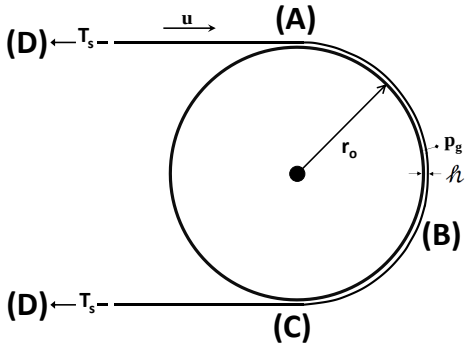

Figure 2.3: Simplified view of the system.

Taking Φ as the coordinate along the direction of the wrap angle, the general form of the steady state Reynolds lubrication equation is written as in Eq. 2.1:

$$\frac{\mathrm{d}}{\mathrm{d}\Phi}\left(\hbar^3\, p_g \frac{\mathrm{d}p_g}{\mathrm{d}\Phi}\right) = 12\mu\, u_s \frac{\mathrm{d}(p_g\, \hbar)}{\mathrm{d}\Phi} \tag{2.1}$$

Where μ is the dynamic viscosity of the gas, u_s is the strip velocity, p_g is the pressure of the gas layer and $\hbar$ is the thickness of the gas layer.

In order to solve the force equilibrium at constant speed, a balance equation for the strip is described in Eq. 2.2 [4]:

$$D\frac{\mathrm{d}^4\hbar}{\mathrm{d}\Phi^4} = p_g + p_{con} - p_\infty - \frac{\mathcal{T}_s\, d_s}{\mathcal{R}} \tag{2.2}$$

Where D is the bending stiffness per unit width, p_{con} is the contact pressure, p_∞ is the ambient pressure, d_s is the strip thickness, $\mathcal{R}$ is the arc of curvature of the strip and $\mathcal{T}_s$ is the strip specific tension. Contact pressure is described as a function

of the distance between the strip and the roll surfaces, $\hbar$, with an empirical relation as seen in Eq. 2.3 [10]:

$$p_{con} = \begin{cases} 0, & \hbar > Ra_{eff} \\ \left(\frac{\sqrt{p_m}}{Ra_{eff}}(Ra_{eff} - \hbar)\right)^2, & \hbar \leq Ra_{eff}. \end{cases} \tag{2.3}$$

Where p_m is the pressure required to force $\hbar$ to zero[1] and Ra_{eff} is the effective roughness of the two surfaces. The effective roughness Ra_{eff} is calculated with Eq. 2.4 [18].

$$Ra_{eff} = \sqrt{Ra_1 + Ra_2} \tag{2.4}$$

Where Ra_1 and Ra_2 are the roughness values of the involved surfaces. The curvature is described as in Eq. 2.5, when $\hbar <<< r_o$ [6]:

$$\frac{1}{\mathcal{R}} = \frac{1}{r_o} - \frac{\mathrm{d}^2\hbar}{\mathrm{d}\Phi^2} \tag{2.5}$$

Differentiating Eq. 2.2 and combining it with Eq. 2.5, the derivative of p_g is found as shown in Eq. 2.6:

$$\frac{\mathrm{d}p_g}{\mathrm{d}\Phi} = D\frac{\mathrm{d}^5\hbar}{\mathrm{d}\Phi^5} - \mathcal{T}_s\, d_s \frac{\mathrm{d}^3\hbar}{\mathrm{d}\Phi^3} \tag{2.6}$$

Combining Eqs. 2.6, 2.1 and 2.2, the governing equation Eq. 2.7 is obtained:

$$\frac{\mathrm{d}}{\mathrm{d}\Phi}\left(\hbar^3\, p_g \left(D\frac{\mathrm{d}^5\hbar}{\mathrm{d}\Phi^5} - \mathcal{T}_s\, d_s \frac{\mathrm{d}^3\hbar}{\mathrm{d}\Phi^3}\right)\right) = 12\mu\, u_s \frac{\mathrm{d}(p_g\, \hbar)}{\mathrm{d}\Phi} \tag{2.7}$$

The governing equation is worked into a different form introducing the following dimensionless parameters shown in Eq. 2.8 to Eq. 2.14 [5, 6]:

$$\beta = \frac{12\mu\, u_s}{\mathcal{T}_s\, d_s} \tag{2.8}$$

$$H = \frac{\hbar\, \beta^{-2/3}}{r_o} \tag{2.9}$$

[1]The value for p_m is taken as 281 MPa for stainless steel AISI 316 [25]. Although the materials used during the experiments are low carbon steel for strip and stainless steel AISI304 for the roll (see Table 2.2), the p_m value for a combination of these materials was not available.

$$C = \frac{p_a - p_{con}}{\mathcal{T}_s \, d_s / r_o} \tag{2.10}$$

$$S = \frac{D \, \beta^{-2/3}}{\mathcal{T}_s \, d_s \, r_o^2} \tag{2.11}$$

$$\phi = \frac{p_g - p_a + p_{con}}{\mathcal{T}_s \, d_s / r_o} \tag{2.12}$$

$$\xi = \frac{s \, \beta^{-1/3}}{r_o} \tag{2.13}$$

Where β is chosen as a perturbation parameter. It has a different constant value for each considered case and it is closely related to the gas layer thickness at the uniformity region [2]. The compressibility effects are represented by the compressibility parameter C. As the ambient pressure dominates over the force applied by the strip tension to the heat pipe, $1/C$ is expected to approach zero. Consequently, this converts the problem to an incompressible one [6]. S is the stiffness parameter, representing the ratio of the moment required to bend the strip to a radius of curvature of r_o and the moment of the strip tension about the center of the heat pipe [5]. H is the dimensionless gap, ϕ is the dimensionless pressure and ξ is an extended coordinate introduced to ensure consistent differentiation of other parameters. $\xi = 0$ corresponds to the initial and final point of contact of a perfectly flexible foil at the stationary situation, whereas ξ approaches $-\infty$ in the uniform region (B) and ∞ beyond the arc of contact. The selection of the powers $1/3$ and $2/3$ are made in a way that the β values are eliminated from the final equation to be derived.

The dimensionless parameters are used to convert Eq. 2.7 to Eq. 2.14:

$$\frac{\mathrm{d}}{\mathrm{d}\Phi}\left(H^3 \, (\phi + C)\left(S\frac{\mathrm{d}^5 H}{\mathrm{d}\xi^5} - \frac{\mathrm{d}^3 H}{\mathrm{d}\xi^3}\right)\right) = \frac{\mathrm{d}}{\mathrm{d}\Phi}\big(H(\phi + C)\big) \tag{2.14}$$

Integration of Eq. 2.14 leads to Eq. 2.15:

$$H^3(\phi + C)\left(S\frac{\mathrm{d}^5 H}{\mathrm{d}\xi^5} - \frac{\mathrm{d}^3 H}{\mathrm{d}\xi^3}\right) = H(\phi + C) + K \tag{2.15}$$

Where K is the integration constant. At the uniform region, as the gas layer thickness becomes constant, the derivatives of $\hbar$ and thus H, converge to zero. Therefore, when ξ nears $-\infty$ (uniform region), the left-hand side of Eq. 2.15 approaches zero. The right-hand side is worked out by writing ϕ in terms of the derivatives of H by combining Eqs. 2.2, 2.5 and 2.12, resulting in Eq. 2.16:

$$\phi = S\frac{\mathrm{d}^4 H}{\mathrm{d}\xi^4} + 1 - \frac{\mathrm{d}^2 H}{\mathrm{d}\xi^2} \tag{2.16}$$

With this form, when ξ nears $-\infty$, it is clear that ϕ approaches 1. This gives the integration constant shown in Eq. 2.17:

$$K = -H^*(1 + C) \tag{2.17}$$

Where H^* is defined as the dimensionless gas layer thickness at the uniform region. The resulting governing equation is therefore described with Eq. 2.18:

$$H^3\left(S\frac{\mathrm{d}^4 H}{\mathrm{d}\xi^4} + 1 - \frac{\mathrm{d}^2 H}{\mathrm{d}\xi^2} + C\right)\left(S\frac{\mathrm{d}^5 H}{\mathrm{d}\xi^5} - \frac{\mathrm{d}^3 H}{\mathrm{d}\xi^3}\right) = H\left(S\frac{\mathrm{d}^4 H}{\mathrm{d}\xi^4} + 1 - \frac{\mathrm{d}^2 H}{\mathrm{d}\xi^2} + C\right) - H^*(1 + C) \tag{2.18}$$

The defined dimensionless parameters in Eq. 2.8 to Eq. 2.13 can be normalized with the dimensionless gas layer thickness at the uniform region H^*, resulting in Eq. 2.19 to Eq. 2.22 [5, 6]:

$$\overline{H} = \frac{H}{H^*} \tag{2.19}$$

$$\overline{\xi} = \frac{\xi}{H^*} \tag{2.20}$$

$$\overline{S} = \frac{S}{H^{*2}} \tag{2.21}$$

$$C^* = (1 + C)H^* \tag{2.22}$$

Using these normalized terms, Eq. 2.18 can be worked into Eq. 2.23:

$$\overline{S}\frac{\mathrm{d}^5 H}{\mathrm{d}\xi^5} - \frac{\mathrm{d}^3 H}{\mathrm{d}\xi^3} = \pm\frac{\overline{H} - \frac{C^*}{\overline{S}\frac{\mathrm{d}^4 H}{\mathrm{d}\xi^4} - \frac{\mathrm{d}^2 H}{\mathrm{d}\xi^2} + C^*}}{\overline{H}^3} \tag{2.23}$$

The $\pm$ sign in Eq. 2.23 represents different equations for the inlet (+) and outlet regions (–). Towards the uniform region (B), $\overline{H}$ converges to 1 and its derivatives to 0. On the other hand, towards region (D), the gas layer thickness increases and the strip approaches a straight shape. This geometry requires the convergence of $\overline{H}'$ to

Table 2.1: Boundary conditions for the model.

Boundary conditions	
$\overline{\xi} \to -\infty$	$\overline{H} \sim 1$
$\overline{\xi} \to -\infty$	$\overline{H}' \sim 0$
$\overline{\xi} \to -\infty$	$\overline{H}'' \sim 0$
$\overline{\xi} \to \infty$	$\overline{H}' \sim \overline{\xi} H^*$
$\overline{\xi} \to \infty$	$\overline{H}'' \sim H^*$

$\overline{\xi} H^*$ far away from the roll[6]. This also implies that $\overline{H}''$ asymptotically approaches H^*. The boundary conditions are summarized in Table 2.1.

These boundary conditions are used to solve the 5$^{\text{th}}$ order ODE in Eq. 2.23 as a boundary value problem with MATLAB®. Air properties are obtained from FluidProp® at the average temperature of the strip and the heat pipe [26].

Through the solution of the above ODE, the thickness and the pressure distribution of the gas layer, the contact pressure as well as the extent of regions (A), (B) and (C) can be determined.

The heat transfer coefficient h at the uniform region (B) is calculated by the addition of individual contributions as shown in Eq. 2.24 [18].

$$h_{total} = h_{sc} + h_g + h_{rad} \tag{2.24}$$

Where h_{total} represents the heat transfer coefficient between the strip and the outer surface of the roll, h_{sc} is the heat transfer through solid contact, h_g is the heat transfer through the gas and h_{rad} is the heat transfer via radiation.

The surface fractions of the heat transfer coefficients in Eq. 2.24 are incorporated in their respective descriptions. The solid contact heat transfer area is a very small fraction of the total heat transfer area. As a result, the heat transfer area through gas is almost equal to the total heat transfer area. The solid contact heat transfer coefficient is calculated with Eq. 2.25 which is already based on the solid contact surface fraction [18]:

$$h_{sc} = 1.25 \frac{k_s\, m}{Ra_{eff}} \left(\frac{p_{con}}{H_e} \right)^{0.95} \tag{2.25}$$

Where k_s is the harmonic mean thermal conductivity of the surfaces, m is the slope of roughness peaks and H_e is the Vickers hardness of the strip. The heat transfer through gas, on the other hand, occurs via conduction. Natural convection is ignored as the $\mathrm{Gr}/\mathrm{Re}^2 < 1$, with Gr being the Grashof number and Re being the Reynolds number. The Knudsen number is less than 0.1 for all simulated cases, therefore the flow is in a continuum regime [19]. Consequently, the heat transfer coefficient through the gas layer is calculated with Eq. 2.26 [20]:

$$h_g = \frac{k_g}{\hbar} \tag{2.26}$$

Where k_g is the thermal conductivity of the gas.

The heat transfer coefficient for radiation is modelled with the radiation taking place between two gray parallel plates, as shown in Eq. 2.27 [27]:

$$h_{rad} = \frac{\sigma\left(T_1^4 - T_2^4\right)}{\left(\frac{1}{\varepsilon_1} + \frac{1}{\varepsilon_2} - 1\right)\left(T_1 - T_2\right)} \tag{2.27}$$

Where T_1 and T_2 are the temperatures of the surfaces, ε_1 and ε_1 are the emissivities of the surfaces and σ is the Stefan-Boltzmann constant. With these equations, the thickness of the gas layer, the gas layer pressure, the contact pressure and the heat transfer are described.

2.4. Experimental setup

The experimental setup used in this work is a rotating heat pipe with integrated steel strips built as the proof-of-principle of the heat pipe assisted annealing concept (see Figure 2.2). It was developed to study the combined heat transfer from the strip to the interior of the heat pipe, through the conducting heat pipe shell and from the inner surface of the heat pipe to the heat pipe working fluid. The steel strips are tensioned between the rotating heat pipe and auxiliary rolls with pneumatic cylinders. Induction is used to heat one of the strips (see Figure 2.4).

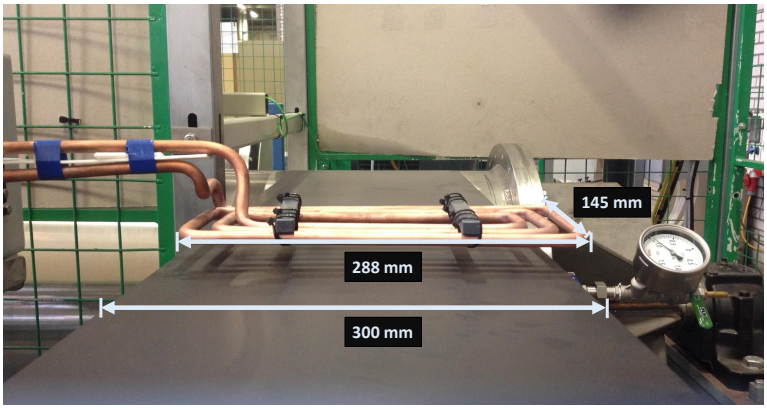

Figure 2.4: Strip heating with induction.

The heat pipe uses demineralized water as working fluid. Its operating temperature ranges from ambient temperature to 120 °C. At its highest operating temperature, the vapor pressure reaches 1.99 bar. The strip that is heated by induction

is fed to the evaporator section of the heat pipe and cools down as it transfers its heat to the heat pipe. The working fluid evaporates causing a local pressure increase. The increased pressure drives the vapor towards the condenser where it condenses. During condensation heat is released, which is absorbed by the cold strip. The liquid is driven back to the evaporator by means of centrifugal force and the head that is formed by evaporation and condensation. The specifications of the setup are given in Table 2.2.

Table 2.2: Setup specifications and experimental conditions.

Parameter	**Data**
Strip material	Cold rolled low carbon steel
Strip thickness	0.26 mm / 0.35 mm
Strip width	300 mm
Strip roughness (Ra)	0.37 µm
Heat pipe material	Stainless steel AISI 304
Heat pipe outer diameter	502 mm
Heat pipe wall thickness	6.5 mm
Heat pipe length	1210 mm
Heat pipe roughness (Ra)	0.75 µm
Water amount inside heat pipe	2 kg (1% fill ratio)
Maximum strip velocity	8 m/s
Maximum strip tension	69 MPa for 0.26 mm strip 52 MPa for 0.35 mm strip
Induction unit capacity	50 kW_e
Induction coil geometry	Rectangular loop of 288 x 145 mm

Other applications of RHPs found in the literature use heat pipes that are much smaller in size and in diameter-to-length ratio compared to the RHP considered in the current work. In this study, the size of the RHP is selected such that the diameter of 0.502 m ensures to avoid plastic deformation of tensioned strips and the length of 1.21 m helps accommodate the strips. This results in a diameter-to-length ratio of 0.41.

In order to study the contact heat transfer between the steel strip and the rotating heat pipe, the temperature evolution of the strip as it is being cooled is recorded with an infrared camera. The infrared camera is aimed at the first 45° of the wrap angle (see Figure 2.5). The infrared camera is a Cedip Jade 3 medium Wave camera 3-5 µm with a 50 mm lens and Sofradir MCT 320 x 240 pixel chip. It is set to record 2 frames per second. The steel strip is coated with an organic heat resistant coating to improve its emissivity for the wavelength employed by the infrared camera.

Additionally, the temperature inside the heat pipe is measured with three K-type thermocouples placed in the vapor channel at different axial locations (evaporator, adiabatic section and condenser). The system is driven by a frequency-controlled drive with an encoder control loop. The strip tension is applied by pneumatic cylin-

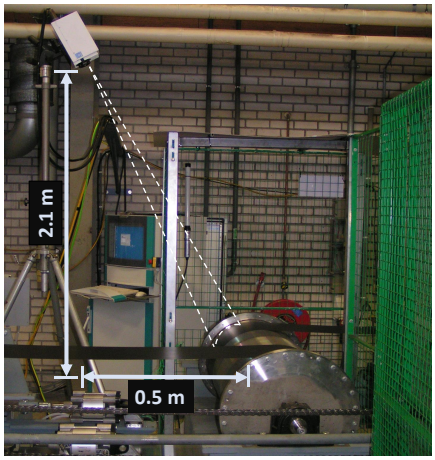

Figure 2.5: Measurement on the experimental setup.

ders, of which the pressure is set and logged. Applying the strip tension with pneumatic cylinders ensures that the total tension over both strip legs is maintained at any temperature. The sensor signals are recorded with a data logger every 3 seconds.

2.5. Experimental methodology and data processing

A summary of the experimental plan is given in Figure 2.6[2]. The parameters that are varied for the experiments are strip velocity, strip thickness and strip tension. In total, 29 cases are examined.

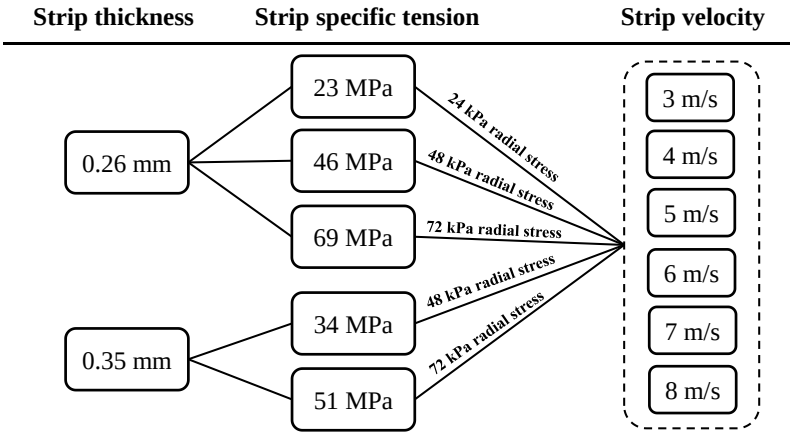

Figure 2.6: Experimental plan.

[2]The data point for 0.26 mm / 69 MPa / 5 m/s is not available.

For each experiment, a near steady-state is reached before recording the measurements. Each measurement is taken for a duration of 30 seconds, resulting in a video of 60 frames for the infrared camera and 10 data points for the other readings. The digital level readings from the infrared camera are converted to temperature readings with Wien's approximation of Planck's law for short wavelengths (See Appendix) [28]. The camera results are compensated for the changing angle of the observed strip. The data was analyzed to determine if near steady-state was actually reached and to determine the measurement precision.

Because the heat transfer coefficient and the gas gap cannot be directly measured, the descriptions are integrated into a system model describing the strip and the evaporator side of the heat pipe in the test setup. The model is a 2D, steady-state, finite difference model, describing the heat pipe evaporator, the heat pipe shell and the strip wrapped around it (see Figure 2.7).

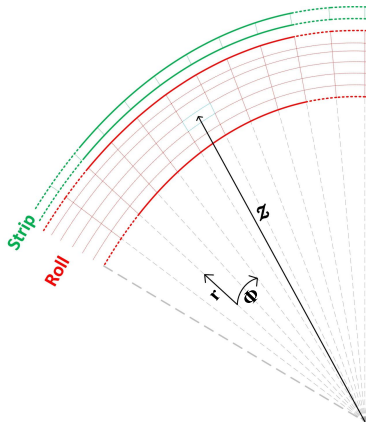

Figure 2.7: Finite difference model layout.

In the finite difference model, the strip is meshed only in the angular direction, as the relevant Biot number is less than 0.1. The roll, on the other hand, is meshed in both the angular and the radial directions. All the nodes are solved using a steady-state energy balance. The energy balance equation for an arbitrary node is shown in Eq. 2.28:

$$0 = \rho c_p v \frac{1}{\mathcal{Z}} \frac{\partial T}{\partial \Phi} + \frac{1}{\mathcal{Z}} \frac{\partial}{\partial \Phi} \left(k \frac{1}{\mathcal{Z}} \frac{\partial T}{\partial \Phi} \right) + \frac{\partial}{\partial r} \left(k \frac{\partial T}{\partial r} \right) \tag{2.28}$$

Where ρ is the density, c_p is the specific heat capacity, k is the thermal conductivity, v is the velocity of the node, $\mathcal{Z}$ is the distance from the center of the roll to the node and T is the temperature of the node. The angular coordinate is Φ, whereas the radial coordinate is r.

Eq. 2.28 is integrated over the nodes. The equations are discretized with the hybrid differencing scheme based on the Péclet number, which is the ratio of advec-

tion to conduction heat transfer ($\text{Pé} = (L_c\, u)/\alpha$). The hybrid scheme uses upwind differencing for $\text{Pé} \geq 2$ and switches to central differencing scheme for $\text{Pé} < 2$ [29]. The heat losses from the strip and the outer surface of the roll to the environment as well as the strip / roll interaction and the fixed vapor channel temperature inside the roll are imposed as boundary conditions.

Inputs to this model are the evaporator temperature, the strip velocity and the inlet strip temperature. The output of the model is the temperature evolution for the strip along the wrap angle. The actual heat transfer coefficient is sought by iterative adjustment of the modelled heat transfer coefficient. The iteration objective is the minimization of least squares of the strip temperature evolution along the observed arc of contact (see Figure 2.8).

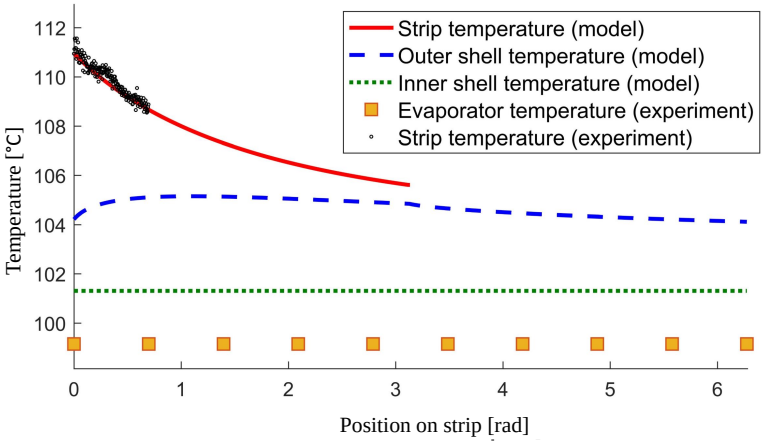

Figure 2.8: Example case with the data processing model (0.26 mm / 23 MPa / 3 m/s).

An uncertainty analysis is made for the calculated heat transfer coefficients. The experimental parameters that contribute to the uncertainty of the results are the uncertainty of the temperature readings from the thermocouple inside the heat pipe and the temperature readings from the infrared camera. Additionally, the uncertainties in the parameters used in the system model were examined [30] leading to the inclusion of the evaporation heat transfer coefficient (taken as 4,000 W/(m^2.K) [31] during the data processing) into the uncertainty analysis.

The experimental results are presented along with a 95% confidence interval. All the measured effects are attributed to variations in the actual heat transfer coefficient. It is observed that the uncertainty in the experimental results is much smaller for the cases where the thermal resistance between the strip and the roll is dominant (low contact heat transfer coefficient cases). For situations where this thermal resistance is low, uncertainty rapidly increases to very large values. This is because what is actually measured during the experiments is the overall thermal resistance of the system rather than the contact thermal resistance. The contact thermal resistance is however calculated from this overall thermal resistance. The

contribution of a low contact thermal resistance to the overall thermal resistance of the system (the contact, the heat pipe shell and the evaporation thermal resistances) is low and insensitive since the total resistance will be governed by the other resistances. This insensitivity results in a large uncertainty in the determination of the contact resistance.

Consequently, it is noted that the cases with lower heat transfer coefficients between the strip and the roll have a lower uncertainty (see Figure 2.9, Figure 2.10 and Figure 2.11).

2.6. Analytical model validation

The contact heat transfer coefficient depends on strip velocity, radial stress and gas properties. The heat transfer coefficients derived from the experiments and the model are given in Figure 2.9 to Figure 2.11 for different radial stresses applied on the roll. The figures are plotted with the same scale to enable easier comparison. Due to large error bars for some of the cases, the y-axis of the plots (heat transfer coefficient values) is limited to a maximum of 40,000 W/(m^2.K).

It should be noted that in all of the cases, the gas layer thickness is computed to be larger than the effective roughness of the two surfaces. The contact pressure is therefore calculated as zero via Eq. 2.3. This results in a solid heat transfer coefficient of zero due to Eq. 2.25. Since the roll is driven by the strips, it is deduced that the contact between the roll and the strips are only peak-to-peak contacts, yielding negligible solid-to-solid conduction. Conduction through the gas layer is the dominant heat transfer mechanism for the considered cases.

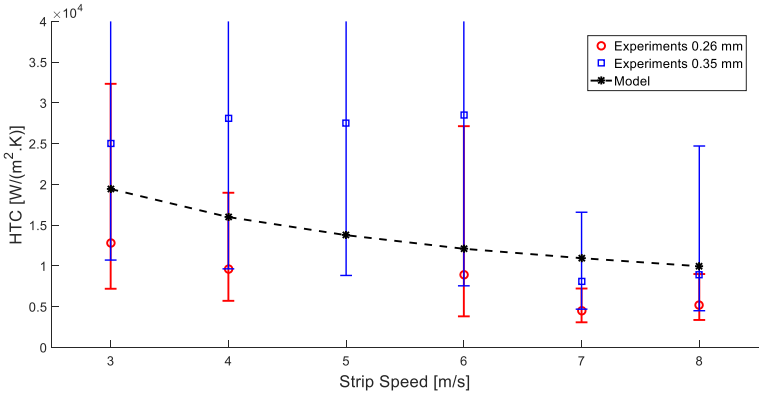

Figure 2.9: Heat transfer coefficients (HTC) with 72 kPa of radial stress applied by the strip to the heat pipe.

The results show that the model is in very good agreement with the experimental results for low radial stress cases (Figure 2.11). As the radial stress applied by the strip to the heat pipe doubles (Figure 2.10), the difference between the experimental and modelling results as well as the magnitude of the error bars substantially increase. At the highest radial stress cases (Figure 2.9), both the error bars and

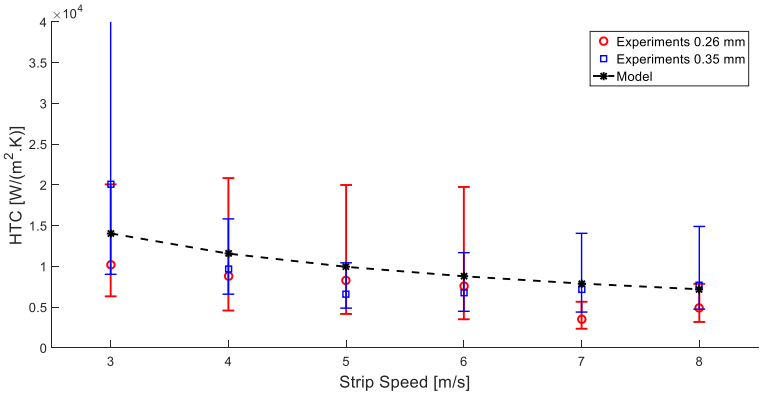

Figure 2.10: Heat transfer coefficients (HTC) with 48 kPa of radial stress applied by the strip to the heat pipe.

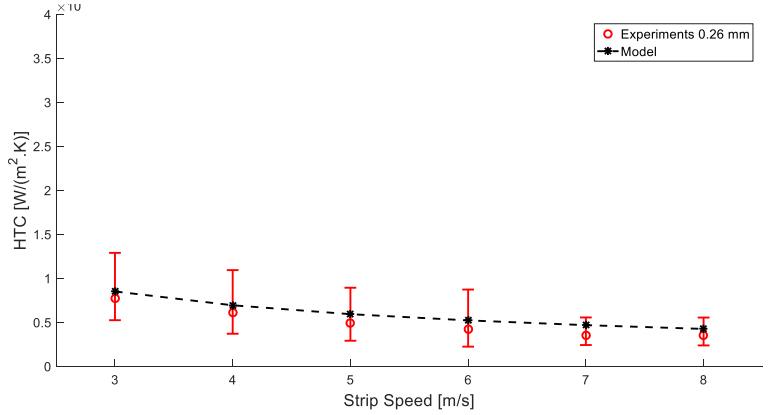

Figure 2.11: Heat transfer coefficients (HTC) with 24 kPa of radial stress applied by the strip to the heat pipe.

the difference between modelling and experimental results become very high. As previously explained, this is because the cases with lower contact heat transfer coefficient values give lower measurement errors and thus, are more precise.

When different data points in the same figure are compared, it is seen that the velocity increase causes the heat transfer to deteriorate. This trend is observed in the model as well as in the experiments. The reason for such a trend is an increase in the amount of gas entrained in the gap between the strip and the roll when the velocity is increased (see Eq. 2.1). In order to satisfy the force balance shown in Eq. 2.2, the pressure of the entrained gas needs to remain constant. This results in an increase in the gas layer thickness, h. A larger gas layer thickness results in a lower heat transfer coefficient, as shown in Eq. 2.26.

The effect of radial stress applied by the strip can be studied when the figures are

compared to each other. An increase in the radial stress improves the contact heat transfer coefficient due to the decrease in gas layer thickness as per Eqs. 2.2 and 2.26. Using the numerical model, the highest heat transfer coefficient is calculated as 20,000 W/(m^2.K) for the 72 kPa radial stress and 3 m/s strip velocity case. The lowest heat transfer coefficient is calculated to be around 4,000 W/(m^2.K) for the 24 kPa radial stress and 8 m/s strip velocity case.

During the experiments, the inlet region (A), where the heat transfer is expected to be limited, could not be discerned. This observation suggests that the extent of the inlet region (A) is relatively small. However, it is important to quantify it, as it reduces the uniform region and thus, the total heat transfer area. At the inlet region (A), the strip approaches the heat pipe until a certain distance between the two surfaces is obtained. According to Eq. 2.2, the tension force and the ambient pressure are counterbalanced by the increasing entrained gas pressure and the contact pressure. Inlet region (A) grows with increasing strip velocity, decreasing strip specific tension and increasing strip thickness, as per the governing equations.

The numerical model results show that the inlet region (A) is always smaller than 1° out of 180° for the configurations shown in Figure 2.6. Two such cases are illustrated in Figure 2.12.

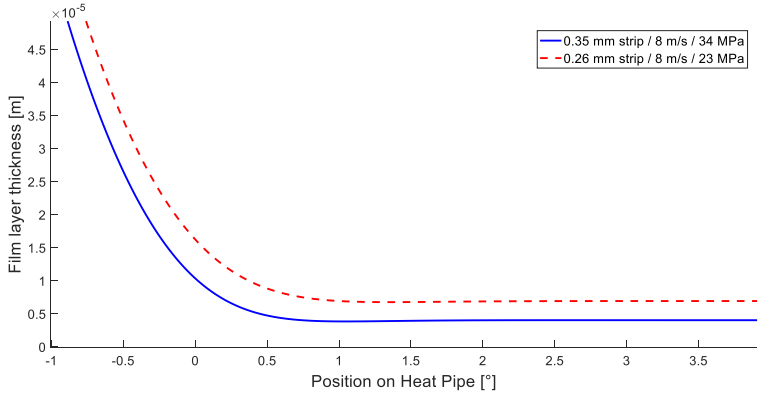

Figure 2.12: Gas layer thickness at the inlet region (A).

The outlet region (C), on the other hand, was not in the field of view of the infrared camera during the experiments. The numerical model results also show that the outlet region (C) is always smaller than 1°out of 180°(see Figure 2.13). The undulation behavior seen at the outlet region is expected to be more visible with increasing stiffness [5]. However, in Figure 2.13, the higher tension force applied to the thicker, and thus stiffer, strip flattens this behavior.

The extent of the entry and exit regions according to Figure 2.12 and Figure 2.13 shows that the uniform region (B) forms about 99% of the total contact area for all of the cases. This will allow for the calculation of the contact thermal resistance only through the wrap angle and the calculated contact heat transfer coefficient, neglecting the effect of entry and exit regions.

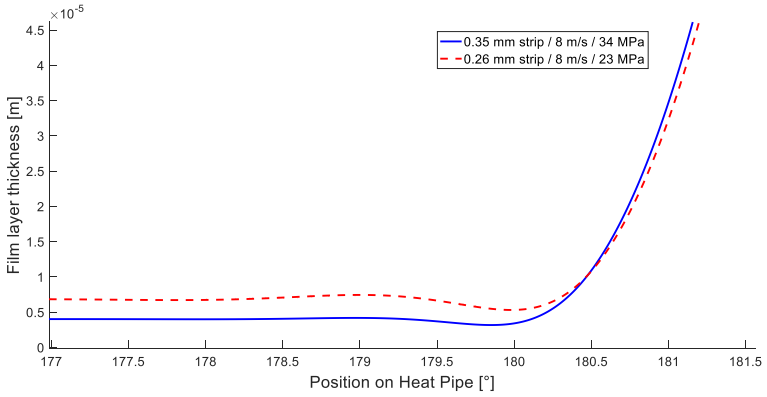

Figure 2.13: Gas layer thickness at the outlet region (C).

2.7. Parametric analysis

Since the first principle model is validated, the results of this model can be extended to various scenarios. In this way, the effect of different parameters can be examined.

As a first step, the effect of strip thickness is investigated in Figure 2.14. Since the same specific tension can be applied to a strip irrespective of its thickness, a thicker strip would result in a higher radial stress applied on the roll by the strip. This means that for a given specific tension and velocity, the contact heat transfer would improve for a thicker strip. This is clearly seen in Figure 2.14, where a thicker strip results in higher heat transfer coefficients.

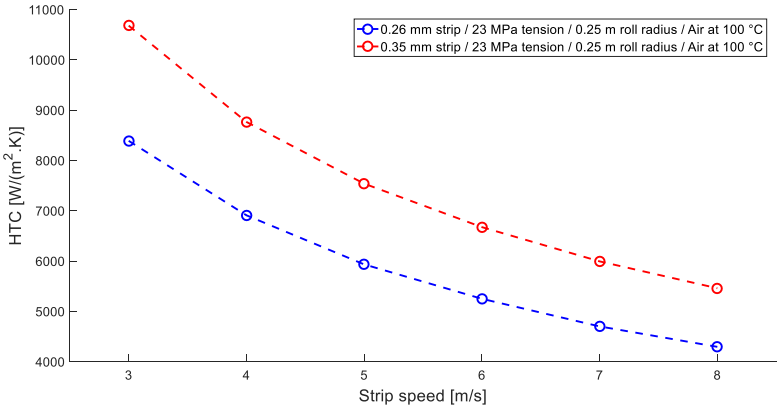

Figure 2.14: Strip thickness effect on contact heat transfer coefficient (HTC).

The effect of different gas properties on the heat transfer coefficient is examined in Figure 2.15. A different interstitial gas has two properties that are relevant

for the current study: viscosity and thermal conductivity. The increase in the viscosity of the gas causes more entrainment and thus, a thicker film layer. However, the increase in the thermal conductivity of the gas favors better heat transfer. All these effects combined, the use of an inert atmosphere similar to the one used in annealing lines (95% N_2 & 5% H_2) [32] and higher temperatures result in higher heat transfer coefficients. Moreover, radiative heat transfer plays a more important role at high temperatures.

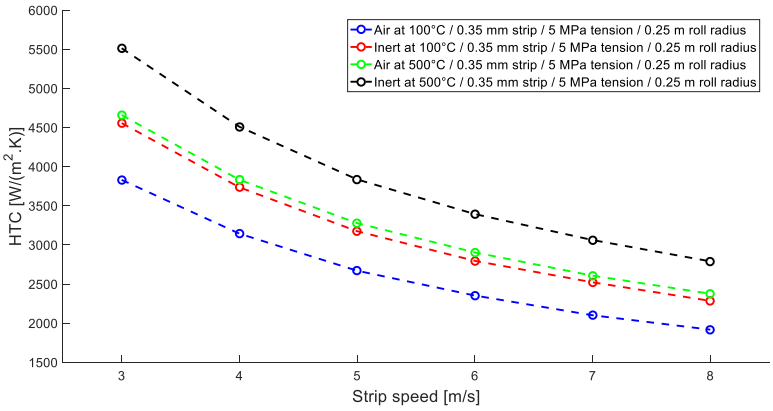

Figure 2.15: Gas properties effect on contact heat transfer coefficient (HTC).

The effect of different roll radius on the heat transfer coefficient is examined in Figure 2.16. A larger roll radius means that the radial stress applied on the roll by the strip is lower. Therefore, the heat transfer coefficient decreases with larger roll radius. It should also be noted that a larger roll radius means a larger contact area for heat transfer.

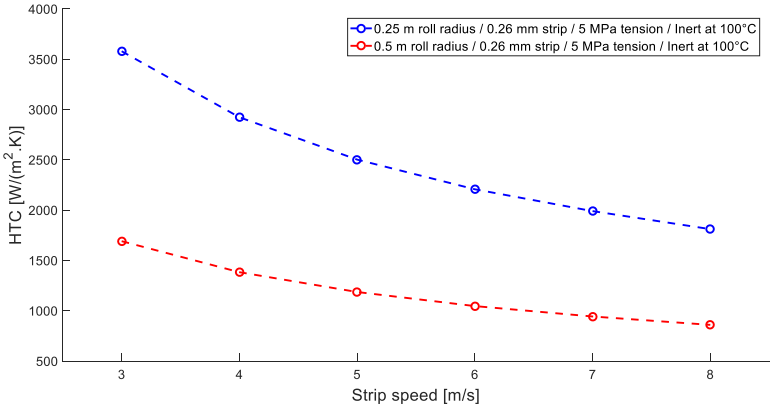

Figure 2.16: Roll radius effect on contact heat transfer coefficient (HTC).

The effect of radial stress and strip speed on heat transfer coefficient can also

be visualized with a contour plot. In Figure 2.17, the contour lines are obtained with the linear interpolation of the modelling results shown in Figure 2.9 to Figure 2.11. It is clearly seen that the heat transfer coefficient decreases with increasing speed and decreasing radial stress.

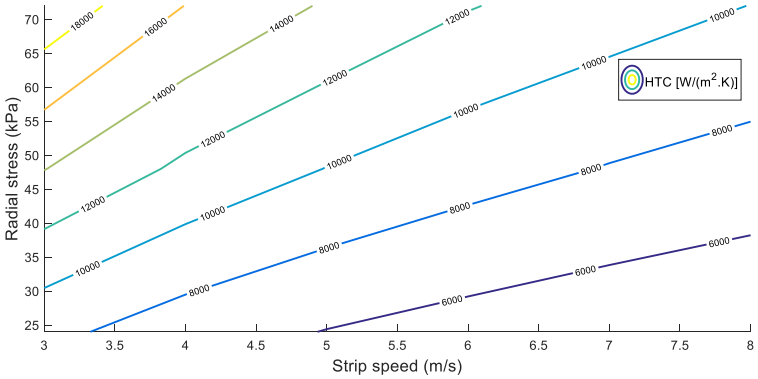

Figure 2.17: Effect of strip speed and radial stress on contact heat transfer coefficient (HTC).

2.8. Simplified expression development

In order to use the findings from this study in the dynamic modelling of multiple RHPs integrated to each other with steel strips (Chapter 5), an attempt to calculate the contact resistance in a faster way is made. As the reduction in the contact area due to entrance region is negligible for the current application, the analysis can be limited to a solution for the contact heat transfer coefficient. The contact resistance can then be calculated with Eq. 2.29.

$$R_{con} = \frac{1}{h_{total} A_{con}} \tag{2.29}$$

Where R_{con} is the contact thermal resistance and A_{con} is the contact area. Nusselt number is instrumental for the dimensionless analysis. It is defined as follows:

$$\mathrm{Nu} = \frac{h_{total}(2r_o)}{k_g} \tag{2.30}$$

Nusselt number is calculated for a training set which is created by running the numerical model with different parameters, namely strip thickness, specific tension, roll radius and gas properties (inert or air at different temperatures). A multiple regression analysis is made using this training set. The resulting Nusselt number correlation is as follows:

$$\mathrm{Nu} = 0.394\,\gamma^{-1}\,\Psi^{(-2/3)} \tag{2.31}$$

Where γ is the compressibility factor and Ψ is the foil bearing number. They are described in Eqs. 2.32 & 2.33.

$$\Psi = \frac{\mu\, u_s}{\mathcal{T}_s\, d_s} \tag{2.32}$$

$$\gamma = \left(0.084\left(\frac{\mathcal{T}_s\, d_s}{p_\infty\, r}\right)^2 - 0.25\left(\frac{\mathcal{T}_s\, d_s}{p_\infty\, r}\right) + 0.643\right) \tag{2.33}$$

Finally, the contact heat transfer coefficient can be found from the Nusselt number via Eq. 2.30. The simplified expression is applicable when the contact heat transfer is dominated by the conduction through the gas layer. The results generated by the simplified expression deviate from the results of the first principle model by less than 10%. The simplified expression is not applicable when solid-to-solid contact plays a role, side leakage is influential or when the entrance / exit regions are large relative to the uniform region.

2.9. Conclusions

In this chapter, the contact heat transfer between a water containing RHP and a moving steel strip is investigated both numerically and experimentally. The determination of the contact heat transfer coefficient for different parameters is instrumental in the implementation of the heat pipe assisted annealing concept and valuable for other studies related to the heat transfer between a roll and a strip.

The numerical model is developed based on first principles. The model consists of two main parts. The first part involves the solution of the Reynolds lubrication equation and the force balance of the strip. In this way, the gap between the strip and the roll is determined. The second part of the model considers different heat transfer mechanisms and calculates the contact heat transfer coefficient.

The experimental part of the current work is performed on a test rig comprising of a roll executed as a heat pipe over which a steel strip travels. The temperature evolution of the steel strip as it travels over the wrap angle is measured at various strip velocity, strip tension and strip thickness configurations. During the measurements, the behavior of the heat pipe is also tracked. As opposed to previous work in literature, the use of a heat pipe in the validation process allows for better isolation of the heat transfer between the strip and the roll from outside influence. This is the case because it allows for a Dirichlet boundary condition at the interior of the roll.

The results of this study show that the results of the first principle model are within the confidence limits of experiments. It is noted that the uncertainty of the experimental measurements becomes very high when the heat transfer coefficient between the strip and the heat pipe is high. The found heat transfer coefficient

ranges from 4,000 to 20,000 W/(m^2.K), showing an increase with decreasing strip velocity and increasing radial stress. The heat transfer is dominated by gas conduction between the heat pipe and the strip. There is no solid-to-solid heat transfer between the surfaces for the considered cases. The reduction of contact area due to strip bending and gas entrainment is found to be negligible for the examined cases.

A simplified expression is developed for the calculation of contact heat transfer through multiple regression analysis. The predictors for the analysis are the strip tension, strip thickness, strip speed, roll diameter and gas properties. The expression can be used when the entrance / exit regions can be neglected and when the gas conduction is dominant.

Several improvements can be considered for the experimental part of this work. An additional measurement for the roll surface temperature or for the heat flux through the heat pipe shell would provide less uncertainty in the experimental results. Moreover, the catalogue of reported heat transfer coefficient values can be extended with different entrained gas types and operating temperatures.

References

[1] L. Licht, *Preliminary experiments with foil bearings,* Journal of Basic Engineering **88**, 1 (1966).

[2] L. Licht, *An experimental study of elastohydrodynamic lubrication of foil bearings: Part 1—displacement in the central zone,* Journal of Lubrication Technology **90**, 199 (1968).

[3] A. Eshel and H. Elrod, *The theory of the infinitely wide, perfectly flexible, self-acting foil bearing,* Journal of Basic Engineering **87**, 831 (1965).

[4] E. J. Barlow, *Derivation of governing equations for self-acting foil bearings,* ASME J. Lubr. Technol **89**, 334 (1967).

[5] A. Eshel and H. Elrod, *Stiffness effects on the infinitely wide foil bearing,* Journal of Lubrication Technology **89**, 92 (1967).

[6] A. Eshel, *Compressibility effects on the infinitely wide, perfectly flexible foil bearing,* ASME Journal of Lubrication Technology **90**, 221 (1968).

[7] K. Ducotey and J. Good, *The effect of web permeability and side leakage on the air film height between a roller and web,* Journal of tribology **120**, 559 (1998).

[8] M. Wildmann, *Foil bearings,* Journal of Lubrication Technology **91**, 37 (1969).

[9] C. Lacey and F. Talke, *A tightly coupled numerical foil bearing solution,* IEEE transactions on magnetics **26**, 3039 (1990).

[10] C. Lacey and F. Talke, *Measurement and simulation of partial contact at the head/tape interface,* Journal of tribology **114**, 646 (1992).

[11] Y. Wu and F. Talke, *The effect of surface roughness on the head-tape interface,* Transactions-ASME Journal of Tribology **118**, 376 (1996).

[12] S. Muftu and R. C. Benson, *A study of cross-width variations in the two-dimensional foil bearing problem,* Journal of tribology **118**, 407 (1996).

[13] S. Müftü and J. J. Jagodnik, *Traction between a web and a smooth roller,* ASME J. Tribol **126**, 177 (2004).

[14] B. S. Rice, K. A. Cole, and S. Müftü, *A model for determining the asperity engagement height in relation to web traction over non-vented rollers,* Journal of tribology **124**, 584 (2002).

[15] K. Ducotey and J. Good, *A numerical algorithm for determining the traction between a web and a circumferentially grooved roller,* Journal of tribology **122**, 578 (2000).

[16] T. Kaşıkcı and S. Müftü, *Modeling the traction of a thin tape guided by a grooved roller,* in *ASME 2013 Conference on Information Storage and Processing Systems* (American Society of Mechanical Engineers, 2013) pp. V001T10A003–V001T10A003.

[17] P. Jeenkour, *A numerical study on air-entrainment between a web and a convex guide roller in a web transportation process,* Applied Mechanics and Materials **392**, 110 (2013).

[18] M. Yovanovich, *New contact and gap correlations for conforming rough surfaces,* in *AIAA 16th Thermophysics Conference, Palo Alto, CA* (1981).

[19] G. S. Springer, *Heat transfer in rarefied gases,* Advances in heat transfer **7**, 163 (1971).

[20] S. Song, M. Yovanovich, and F. Goodman, *Thermal gap conductance of conforming surfaces in contact,* Journal of Heat Transfer **115**, 533 (1993).

[21] M. M. Yovanovich, *Four decades of research on thermal contact, gap, and joint resistance in microelectronics,* IEEE transactions on components and packaging technologies **28**, 182 (2005).

[22] J.-M. Buchlin, M. Delsipé, P. Planquart, and M. Renard, *Contact conductance determination using infrared thermography,* in *12th Int. Conf. on Quantitative InfraRed Thermography* (2014).

[23] M. Renard and J.-M. Buchlin, *Energy efficient strip annealing through roll regenerative furnace,* Energy Procedia **120**, 380 (2017).

[24] J.-M. Buchlin and M. Renard, *Multi-roll heat exchanger,* (Eurotherm Seminar 106, Paris, France, 2016).

[25] N. Diomidis, J.-P. Celis, P. Ponthiaux, and F. Wenger, *Tribocorrosion of stainless steel in sulfuric acid: Identification of corrosion–wear components and effect of contact area,* Wear **269**, 93 (2010).

[26] P. Colonna and T. Van der Stelt, *Fluidprop: a program for the estimation of thermo physical properties of fluids,* Energy Technology Section, Delft University of Technology, Delft, The Netherlands, http://www.FluidProp.com, (2004).

[27] F. P. Incropera, A. S. Lavine, T. L. Bergman, and D. P. DeWitt, *Fundamentals of heat and mass transfer* (Wiley, 2007).

[28] D. P. DeWitt and G. D. Nutter, *Theory and practice of radiation thermometry* (John Wiley & Sons, 1988).

[29] H. K. Versteeg and W. Malalasekera, *An introduction to computational fluid dynamics: the finite volume method* (Pearson education, 2007).

[30] R. J. Moffat, *Describing the uncertainties in experimental results,* Experimental thermal and fluid science **1**, 3 (1988).

[31] V. H. Gray, A. Joslyn, and P. Marto, *Boiling heat transfer coefficients, interface behavior and vapor quality in rotating boiler operating to 475 G's*, NASA Technical Note TN D-4136 (NASA, 1968).

[32] H. Chandler, *Heat treater's guide: practices and procedures for irons and steels* (ASM international, 1994).

3

Heat pipe modelling

Part of this chapter has been published as:

M. Celik, G. Paulussen, D. van Erp, W. de Jong, and B. J. Boersma, *Transient Modelling of Rotating and Stationary Cylindrical Heat Pipes: An Engineering Model*, Energies, **11**(12), 3458 (2018).

3.1. Problem definition

The main objective of this thesis, namely *studying the fundamentals and the feasibility of the heat pipe assisted annealing concept*, can only be achieved through a detailed dynamic model of the whole heat pipe assisted annealing plant. Therefore, modelling of a rotating heat pipe (RHP) is an indispensable step for the realization of this objective.

In this context, the requirements of the RHP model to be developed are listed below.

- The model should be transient since the overarching model of the whole plant will also be transient.
- The model should describe the interior dynamics of the heat pipe with sufficient details (e.g. liquid height, liquid velocity, vapor velocity, vapor pressure, temperature distribution under the influence of current state and externally imposed loads, etc.).
- The model should be fast enough to allow for relatively low computational cost of the dynamic model consisting of ~100 heat pipes linked to each other with strips.

RHP modelling has been the subject of many studies and publications. However, as it is explained in the following section, these models are not aligned with the requirements of the current application. Most of these models are steady-state or transient CFD models of tapered RHPs necessitating high computational costs or faster analytical models limited to steady-state cases of cylindrical RHPs. Therefore, this chapter deals with the following research question:

> *How can one develop a transient rotating heat pipe model which provides sufficient details about its interior dynamics without experiencing long computational times?*

Modelling of other types of heat pipes can also be instrumental in developing an RHP model. A look at the modelling of capillary-driven heat pipes (CDHP) shows that lumped parameter models are as common as CFD models. Lumped parameter models have a much lower computational cost than the CFD models, however they come at the expense of a significant loss of detail. Nonetheless, the lumped parameter models are important in showing that heat pipes can be modelled in a simpler way although the underlying physics is relatively complex with phase-change and fluid flows in two phases.

In the light of this information, the aim of this chapter is to develop a heat pipe model that meets the aforementioned requirements. The model will be applicable to both CDHPs and RHPs as long as they are cylindrical.

3.2. Literature review

In order to predict the transient behavior of heat pipes and to improve their designs, various numerical methods have been developed. For the dynamic modelling

of CDHPs, these methods range from thermal network analysis to detailed computational fluid dynamics (CFD).

A transient analytical lumped model has been developed by Faghri et al. [1] where the heat pipe has been considered as one lumped mass with a uniform temperature. Zuo et al. [2] described the heat pipe as a collection of lumped masses with specific thermal resistances (see Figure 3.1). This model allows for the simplification of the governing equations to first-order linear ordinary differential equations (ODEs). In this way, the analysis of the system becomes relatively simple. The results obtained with this model are sufficiently accurate. The dynamic behavior of a flat plate heat pipe has been described by Xuan et al. [3], who solved the transient conduction equation for the wall and the wick region, whereas a lumped model is used for the vapor phase. The vapor flow is neglected in this work. Tsai et al. solved the energy equations by dividing the heat pipe into three control volumes: wall and wick at the evaporator, wall and wick at the condenser and the working fluid [4]. Another lumped parameter approach has been adapted by Ferrandi et al. [5], which also accounts for liquid and vapor flow and storage. In their work, the governing equations for fluids are solved by assuming that each phase is held in two tanks (evaporator and condenser) with a communication path connecting them.

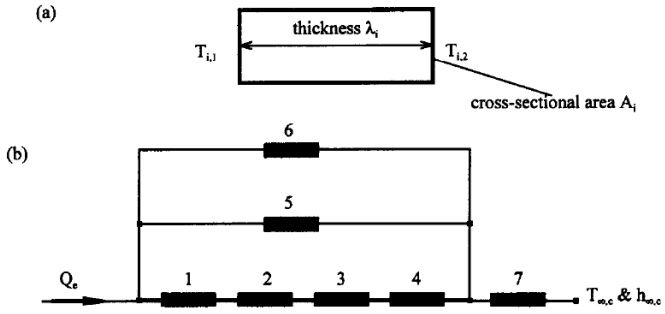

Component	Descriptions
Q_e	Evaporator heat input
1	Evaporator wall (radial direction)
2	Evaporator wick (radial direction)
3	Condenser wick (radial direction)
4	Condenser wall (radial direction)
5	Adiabatic wick (axial direction)
6	Adiabatic wall (axial direction)
7	Convective cooling condition (condenser outer surface)

Figure 3.1: System analysis in [2], a) A one-dimensional heat conductor, b) A heat pipe network system.

Wits and Kok [6] used a control volume element approach to model the transient behavior of a flat miniature heat pipe. In this control volume method, the liquid and the vapor at the evaporator and the condenser are separately lumped into

two control volumes and the governing equations are solved. Tournier et al. [7] developed a two-dimensional transient model in which the energy and momentum discontinuities at the liquid / vapor interface are incorporated. In this work, special attention is paid to the prediction of liquid pooling and the curvature of the liquid meniscus. Solomon et al. [8] presented a transient CFD model where Navier–Stokes equations are solved for a very fine mesh with the assumption of a laminar and incompressible two-dimensional flow.

For RHPs, steady-state modelling has been extensively addressed [9–11], with recent studies focusing on the use of nanofluids [12, 13]. On the other hand, transient modelling studies are scarce. A detailed dynamic model is presented by Harley et al. [14], which solved the continuity, momentum, and energy equations for an axisymmetric geometry on a fixed grid. In this model, the set of highly non-linear equations are solved using the SIMPLE algorithm [15]. Baker et al. [16] have solved the Navier–Stokes equations and the energy equation using the volume of fluid (VOF) model to predict the liquid-vapor interface. A more recent study by Lian et al. [17] also describes the transient behavior of the heat pipe with Navier–Stokes equations and VOF using a novel phase-change model. For all these studies, the modelled RHPs have a conical shape at the condenser or throughout.

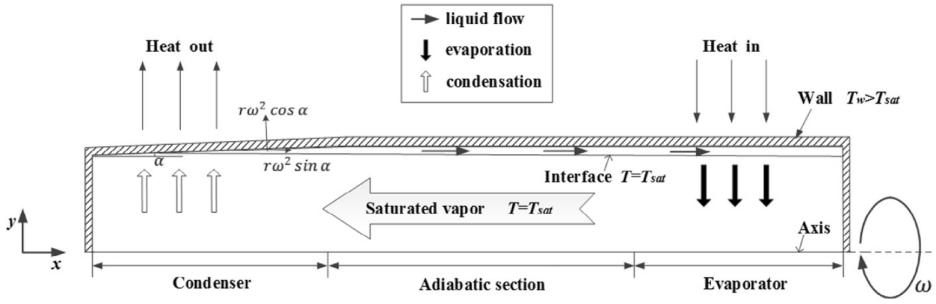

Figure 3.2: Modelled RHP geometry [17].

It is not a coincidence that all of the transient RHP models are CFD studies, whereas the transient CDHP models can vary in methodology, from lumped capacitance models to control volume approaches and to CFDs. This is because the liquid layer distribution along the axial direction should be known for a reasonable estimation of the thermal characteristics of the RHP. The information on the liquid layer distribution is also beneficial for CDHPs, but not a must, as the thermal resistance associated with the liquid / wick is usually low and is not a strong function of the liquid layer thickness. It is crucial for the working fluid circulation but in most cases not influential for the thermal behavior of the system due to the high thermal conductivity of the wick structure.

For RHPs, on the other hand, the dominant thermal resistance can easily be the liquid layer due to the lack of the wick structure. The thermal resistance associated with the liquid layer is directly coupled to the thickness of the liquid both at the condenser (only conduction) and at the evaporator (conduction and / or natural

convection) [18]. This requires a detailed modelling of the heat pipe interior and the obvious choice has been CFD rather than a lumped capacitance approach for transient models. For steady-state cases, analytical models are feasible [11].

3.3. Numerical model description

3.3.1. Model geometry

The model geometry is a 2D representation of a cylindrical heat pipe, making use of its symmetry along the angular direction. The three main components of the model are the heat pipe wall, the liquid, and the vapor, each modelled as a single lumped mass in the radial direction. They are all axially meshed to a desired number of cells, irrespective of the heat pipe section they belong to. All of the wall cells are governed by the same set of equations. The same is valid for all liquid cells and all vapor cells. The connection of a group of cells is shown in Figure 3.3.

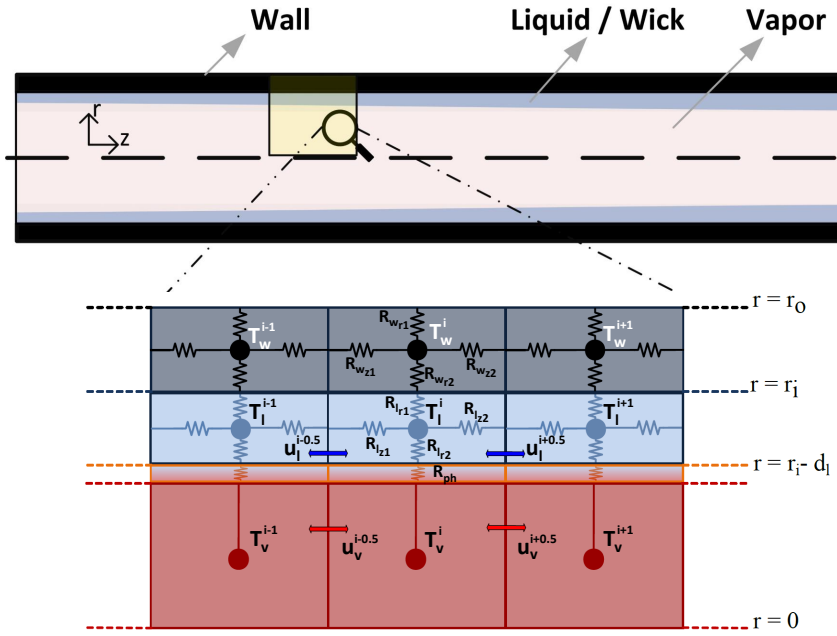

Figure 3.3: Model geometry and cells.

Each node in Figure 3.3 is a lump mass characterized by a unique thermodynamic state. The resistances are associated with thermal conduction through the material and the phase change. As can be seen in the figure, the mesh is staggered such that the temperatures and pressures are located at cell centers, whereas velocities are located at cell faces. The liquid and the vapor mesh can grow and shrink in the radial direction. In this way, the location of the interface for an axial location can change in time and liquid head can be incorporated in the model. The architecture

of the nodes and their connections allow the same equations to be used throughout the whole heat pipe.

3.3.2. Model assumptions and simplifications

In order to create a practical, applicable and yet sufficiently detailed model of the heat pipe functioning, several simplifications and assumptions are made. These simplifications and assumptions follow out of the selected model geometry. They are itemized below with the relevant references from similar studies when applicable:

- An axisymmetric geometry is chosen, requiring the omission of gravity, which is unidirectional in reality.
- A one-dimensional approach is taken for the flow of liquid and vapor.
- The heat input and output to the lumped masses through the resistances are linearly approximated [2, 14].
- The vapor is treated as an ideal gas [8, 14].
- The liquid and the vapor are incompressible [14, 19].
- Thermal expansion of the heat pipe container and the wick is neglected.
- The liquid layer thickness is much smaller than the radius of the heat pipe [11, 14].
- The dynamics of the vapor is much faster than the dynamics of the other components [2]. Therefore, the vapor is assumed to be always saturated, taking into account the mass flows of the phase change and its associated latent heat.
- The pressure drop of the vapor is much smaller than the pressure drop of the liquid along the heat pipe [7, 11, 20].
- For rotating heat pipes without a wick structure, the thermal conduction through the liquid in the axial direction is neglected [9–11].
- For the liquid component of the rotating heat pipes without a wick structure, the heat transfer in the radial direction is taken to be dominant over the heat transfer in the axial direction [10, 11, 14].

3.3.3. Governing physics

Following the model geometry (Figure 3.3) and the simplifications (Subsection 3.3.2), the governing equations for the different components are formulated.

Firstly, the thermal resistances in the radial and axial directions shown in Figure 3.3 are defined according to Eqs. 3.1 and 3.2:

$$R_{radial} = \frac{\ln(r_o/r_i)}{2\pi\, k\, \Delta z} \tag{3.1}$$

$$R_{axial} = \frac{\Delta z}{k\, A} \tag{3.2}$$

where R_{radial} and R_{axial} are the thermal resistances at the radial and axial directions respectively, r_o and r_i are the outer and inner radii of the given resistance respectively, k is the thermal conductivity of the component, Δz is the length of the resistance in the axial direction and A is the cross-sectional area of the cell in the axial direction. In case of CDHP, the effective thermal conductivity of the liquid / wick is calculated using Eq. 3.3 [8].

$$k_{eff} = k_l \left(\frac{(k_l + k_{wk}) - (1-\varepsilon)(k_l - k_{wk})}{(k_l + k_{wk}) + (1-\varepsilon)(k_l - k_{wk})} \right) \tag{3.3}$$

where ε is the porosity of the wick and the subscripts l and wk represent liquid and wick, respectively.

Wall component

Following the definition of the thermal resistances, the transient energy equation for a wall component is defined as in Eq. 3.4 in its discretized form in space.

$$m_w^i\, c_{p_w}^i \frac{\mathrm{d}T_w^i}{\mathrm{d}t} = \dot{Q} + \frac{T_l^i - T_w^i}{R_{w_{r2}}^i + R_{l_{r1}}^i} + \frac{T_w^{i-1} - T_w^i}{R_{w_{z2}}^{i-1} + R_{w_{z1}}^i} + \frac{T_w^{i+1} - T_w^i}{R_{w_{z1}}^{i+1} + R_{w_{z2}}^i} \tag{3.4}$$

where c_p is the specific heat capacity, m is the mass of the node, T is the temperature, t is the time, $\dot{Q}$ is the external heat flow to / from the node, the subscript w represents the heat pipe wall and the superscript i points to the index of the node. The relevant thermal resistances are shown in Figure 3.3. This equation shows that the change in the energy content of a wall component depends on the external heat flow to / from the node as well as the heat conduction through it.

Liquid component

For the liquid component, the governing equations for mass, momentum and energy are simultaneously solved. All these equations are presented in their discretized forms in space. The continuity equation for a given liquid node is described in Eq. 3.5.

$$\varepsilon \frac{\mathrm{d}\left(\rho_l^i V_l^i\right)}{\mathrm{d}t} = \varepsilon\, \rho_l^{i-0.5} A_l^{i-0.5} u_l^{i-0.5} - \varepsilon\, \rho_l^{i+0.5} A_l^{i+0.5} u_l^{i+0.5} - \dot{m}_{ph}^i \tag{3.5}$$

where ρ is the density, V is the volume, u is the velocity and $\dot{m}_{ph}$ is the phase change rate. Porosity for a wickless RHP is taken as 1 ($\varepsilon = 1$). Upwind scheme can be used for the computation of properties at the cell interfaces.

The phase change rate $\dot{m}_{ph}$ and the cross-sectional area of the liquid node A_l are defined with Eqs. 3.6 and 3.7.

$$\dot{m}_{ph} = \frac{T_l^i - T_v^i}{\left(R_{l_{r2}}^i + R_{ph}^i\right) H_{fg}} \tag{3.6}$$

$$A_l^i = \pi\left(r_i^2 - \left(r_i - d_l^i\right)^2\right) \tag{3.7}$$

where H_{fg} is the latent heat, r_i is the inner radius of the heat pipe, d_l^i is the thickness of the liquid layer and the subscript v represents vapor. The thermal resistances are illustrated in Figure 3.3. The thermal resistance associated with phase change, R_{ph}, is often neglected as it is orders of magnitude lower than the other thermal resistances shown in Figure 3.3 [21]. However, it can be accounted for in the simulation of heat pipes filled with alkali metal due to low liquid thermal resistance [22].

The liquid momentum equation is defined with Eq. 3.8.

$$\frac{\mathrm{d}\left(\rho_l^{i+0.5} u_l^{i+0.5}\right)}{\mathrm{d}t} = -\frac{\Delta p_l}{\Delta z'} - \frac{\rho_l^{i+1}\left(u_l^{i+1}\right)^2}{\Delta z'} + \frac{\rho_l^i \left(u_l^i\right)^2}{\Delta z'} + \gamma_l \tag{3.8}$$

where $\Delta z'$ is the distance between the adjacent node centers, Δp_l is the pressure difference between adjacent nodes and γ is the viscous term of the momentum equation. The second and the third terms on the right-hand side are the convective terms. In order to calculate the liquid velocities at the cell centers (see the convective terms), Eq. 3.9 is used.

$$u^i = \frac{u^{i-0.5} + u^{i+0.5}}{2} \tag{3.9}$$

The pressure term and the viscous term are evaluated differently for CDHPs and RHPs. For an CDHP, the pressure term is calculated using Eq. 3.10.

$$\Delta p_{l_{CDHP}} = f\frac{2\sigma}{r_{cap}} \tag{3.10}$$

where $2\sigma/r_{cap}$ is the maximum capillary pressure [23] with σ being the surface tension and r_{cap} being the capillary radius. f is a correction coefficient accounting for the change in contact angle fluid-wick between adjacent nodes. This change is commonly approximated as the difference in the liquid fill ratio of the wick between adjacent nodes [5, 6].

The viscous term for a CDHP is calculated with the well-established equation for laminar flows [21].

$$\gamma_{l_{CDHP}} = -\frac{\mu_l}{K}\,\varepsilon\,u_l \tag{3.11}$$

where μ is the viscosity and K is the wick permeability.

For the rotating heat pipe, on the other hand, the pressure term is calculated using Eq. 3.12.

$$\Delta p_{l_{RHP}} = \left(d_l^{i+1}\rho_l^{i+1} - d_l^i\rho_l^i\right)\omega^2\,r_i \tag{3.12}$$

where ω is the rotational speed. It should be noted that in the studies concerning RHPs with a taper, the slope of the liquid film is often assumed to be much lower than the taper angle [9, 14]. Therefore, the hydrostatic pressure gradient is neglected. In a cylindrical RHP however, it is crucial to account for the slope of the liquid film as it is the main driving force for the liquid flow from the condenser to the evaporator.

The calculation of the viscous term is not as straightforward as it is for the CDHP. In order to calculate the viscous term for the liquid flow, the axial velocity profile throughout the liquid film should be known. However, in the model only the average velocity for the liquid is calculated. Since the liquid velocity at an axial location can be defined as a second order polynomial in the radial coordinate [14, 24], the velocity profile is approximated using a quadratic equation.

$$u_l(r) = C_1 r^2 + C_2 r + C_3 \tag{3.13}$$

With three unknowns (C_1, C_2 and C_3), one needs three equations and / or boundary conditions to solve the velocity profile. The velocity profile is solved using the following equations.

$$r = r_i \rightarrow u_l = 0$$

$$r = r_i - d_l \rightarrow \frac{\partial u_l}{\partial r} = 0 \tag{3.14}$$

$$u_l = \frac{\int_0^{2\pi}\int_{r_i-d_l}^{r_i} u_l\,r\,\mathrm{d}\Phi\,\mathrm{d}r}{\pi\left(r_i^2 - \left(r_i - d_l\right)^2\right)}$$

Where the first equation is the no-slip boundary condition at the inner wall [9–11], the second equation is the negligible shear stress boundary condition at the liquid/vapor interface [11, 25] and the third equation describes the average velocity

as the velocity profile integrated over the liquid film divided by the cross-sectional area.

Once the velocity profile is known, the viscous term is calculated by integrating the expression in Eq. 3.15 over the control volume of the relevant node and then dividing it by the node volume.

$$\gamma = \frac{\int_{CV} \mu \left(\frac{1}{r} \frac{\partial}{\partial r} \left(r \frac{\partial u}{\partial r} \right) \right)}{V} \tag{3.15}$$

The resulting expression for the viscous term is found as shown in Eq 3.16.

$$\gamma_{l_{RHP}} = \frac{\mu_l \left(4C_1 r_i^2 + 2C_2 r_i - 4C_1 (r_i - d_l)^2 - 2C_2 (r_i - d_l) \right)}{\left(r_i^2 - (r_i - d_l)^2 \right)} \tag{3.16}$$

Finally, the energy equation for the liquid is described with Eq. 3.17.

$$\rho_l^i \, V_l^i \, \varepsilon \, c_{p_l}^i \frac{\mathrm{d}T_l^i}{\mathrm{d}t} + \left[m_{wk}^i \, c_{p_{wk}}^i \frac{\mathrm{d}T_l^i}{\mathrm{d}t} \right] = \frac{T_w^i - T_l^i}{R_{w_{r2}}^i + R_{l_{r1}}^i} + \frac{T_v^i - T_l^i}{R_{ph}^i + R_{l_{r2}}^i} + \left[\frac{T_l^{i-1} - T_l^i}{R_{l_{z2}}^{i-1} + R_{l_{z1}}^i} + \frac{T_l^{i+1} - T_l^i}{R_{l_{z1}}^{i+1} + R_{l_{z2}}^i} \right] \tag{3.17}$$

Where the terms in brackets are only applicable to the CDHP with a wick structure. Porosity for the wickless RHP is taken as 1. The relevant resistances are shown in Figure 3.3.

For the evaporator section of an RHP, the liquid thermal resistance needs to be calculated by taking natural convection into consideration alongside thermal conduction wherever applicable. This can be done with the mixed convection evaporator model described by Song et al. [18, 26] and Bertossi et al. [11] when the corresponding Rayleigh number exceeds a value of 400. Below this value, natural convection does not play a role as the prevailing heat transfer mechanism is conduction. The liquid resistance in the presence of natural convection is calculated as follows:

$$R_{l,evp} = \frac{\ln\left(\frac{r_i}{r_i - d_l} \right)}{2\pi \, \mathrm{Nu_m} \, k_l \, \Delta z} \tag{3.18}$$

Where $\mathrm{Nu_m}$ is defined as:

$$\mathrm{Nu_m}^{7/2} = \mathrm{Nu_f}^{7/2} + \mathrm{Nu_n}^{7/2} \tag{3.19}$$

Where $\mathrm{Nu_f}$ is taken as 1 due to relatively low liquid flow Reynolds number and $\mathrm{Nu_n}$ is defined as:

$$\mathrm{Nu_n} = 0.133\mathrm{Ra}^{0.375} \tag{3.20}$$

The Rayleigh number (Ra) for a rotating heat pipe is calculated with Eq. 3.21.

$$\mathrm{Ra} = \frac{\beta\,\rho_l\left(r_i\,\omega^2\right)\Delta T\,d_l^3}{\mu_l\,\alpha_l} \tag{3.21}$$

Where β is the thermal expansion coefficient and α_l is the thermal diffusivity.

Vapor component

Similar to the liquid component, the governing equations for the vapor component are the continuity, momentum, and energy equations. The continuity equation for a vapor node is presented in Eq. 3.22. Together with Eq. 3.5 where the continuity equation for a liquid node is defined, the total mass inside the heat pipe is conserved.

$$\frac{\mathrm{d}\left(\rho_v^i\,V_v^i\right)}{\mathrm{d}t} = \rho_v^{i-0.5}A_v^{i-0.5}u_v^{i-0.5} - \rho_v^{i+0.5}A_v^{i+0.5}u_v^{i+0.5} + \dot{m}_{ph}^i \tag{3.22}$$

The vapor momentum equation is described with Eq. 3.23.

$$\frac{\mathrm{d}\left(\rho_v^{i+0.5}u_v^{i+0.5}\right)}{\mathrm{d}t} = -\frac{\Delta p_v}{\Delta z'} - \frac{\rho_v^{i+1}\left(u_v^{i+1}\right)^2}{\Delta z'} + \frac{\rho_v^i\left(u_v^i\right)^2}{\Delta z'} + \gamma_v \tag{3.23}$$

where Δp_v is the vapor pressure difference between adjacent nodes. It is computed with Eq. 3.24 through the use of Antoine equation for the calculation of vapor pressures.

$$\Delta p_v = 10^{A-\frac{B}{T_v^{i+1}+C}} - 10^{A-\frac{B}{T_v^i+C}} \tag{3.24}$$

where A, B and C are Antoine equation constants.

Similar to the momentum equation of a liquid node, the second and the third terms on the right-hand side describe the convective terms. The viscous term is calculated in a way similar to the one in liquid without a wick structure. The velocity profile throughout the vapor core is represented with a second order polynomial as shown in Eq. 3.25.

$$u_v(r) = C_4 r^2 + C_5 r + C_6 \tag{3.25}$$

For three unknowns (C_4, C_5 and C_6), three equations / boundary conditions are described.

$$r = r_i - d_l \rightarrow u_v = u_l$$

$$r = 0 \rightarrow \frac{\partial u_v}{\partial r} = 0 \tag{3.26}$$

$$u_v = \frac{\int_0^{2\pi} \int_0^{r_i - d_l} u_v \, r \, \mathrm{d}\Phi \, \mathrm{d}r}{\pi \left(r_i - d_l\right)^2}$$

where the first equation is the symmetry condition at the heat pipe center, the second equation is the no-slip boundary condition at the liquid / vapor interface [7, 14] and the third equation describes the average velocity of the vapor. As in the viscous term calculation for liquid, the viscous term for vapor can be found by integrating the expression in Eq. 3.15 over the control volume of the relevant node and then dividing it by the node volume. In this way, the viscous term for vapor flow is found as shown in Eq. 3.27.

$$\gamma_v = \frac{\mu_v \left(4C_4 \left(r_i - d_l\right)^2 + 2C_5 \left(r_i - d_l\right)\right)}{\left(r_i - d_l\right)^2} \tag{3.27}$$

Following the assumption of much faster vapor dynamics compared to other components, the vapor energy equation is calculated with the ideal gas law as shown in Eq. 3.28.

$$\frac{p_v^i}{T_v^i} = \frac{\rho_v^i \, \mathcal{R}_g}{M} \tag{3.28}$$

where $\mathcal{R}_g$ is the universal gas constant and M is the molecular weight of the fluid.

3.3.4. Boundary conditions

The boundary conditions at the outer wall surface can be either of Type-II or Type-III.

$$r = r_o \rightarrow$$
$$-k\frac{\mathrm{d}T}{\mathrm{d}r} = \dot{Q}'' \;||\; -k\frac{\mathrm{d}T}{\mathrm{d}r} = 0 \;||\; -k\frac{\mathrm{d}T}{\mathrm{d}r} = (h_{conv} + h_{rad})(T_\infty - T_{w_{r_o}}) \quad (3.29)$$

where r_o is the outer radius of the heat pipe, $\dot{Q}''$ is the heat flux, h_{conv} is the convective heat transfer coefficient, h_{rad} is the linearized radiative heat transfer coefficient and finally T_∞ is the ambient temperature.

The boundary conditions applied to the end caps of the heat pipe are:

$$z = 0 \;\&\; z = L_{hp} \rightarrow u_l = u_v = 0 \;\&\; \frac{\mathrm{d}T}{\mathrm{d}z} = 0 \quad (3.30)$$

where L_{hp} is the heat pipe length. The boundary condition at the symmetry line is:

$$r = 0 \rightarrow \frac{\mathrm{d}T}{\mathrm{d}r} = 0 \quad (3.31)$$

Additionally, the boundary conditions described in Eqs. 3.14 and 3.26 for the calculation of the viscous terms apply.

3.3.5. Numerical solution

The governing equations are comprised of first-order ODEs and algebraic equations. This is a stiff problem, especially due the fast dynamics of the vapor compared to other components. Therefore, the system of equations is solved implicitly with the "MATLAB ode15i" function.

The mesh size in the axial direction can be changed according to the level of detail requested from the model. The accuracy deteriorates at a low number of computational cells especially when the liquid height is non-linear along the heat pipe length. This is usually the case when the fill ratio is very low, the heat flux is high and the heat pipe is long.

3.4. Model validation

The model presented in the previous section is validated for CDHP and RHP. For CDHP, the validation is made for a transient case where the predictions are compared to the results from an experimental and a numerical work. For RHP, the predictions at steady-state are compared to the outcomes of an experimental work as well as to the steady-state analytical and numerical simulations. In this way, the validity of the developed model is tested for different types of heat pipes at different conditions. After the validations, the computational efficiency of the model is investigated. Finally, the effect of operating temperature on vapor dynamics and the effect of rotational speed on liquid height distribution are studied.

3.4.1. Transient behaviour validations

To validate the dynamic predictions of the presented model, the experimental results of Huang et al. [27] and the numerical results of Ferrandi et al. [5] for a cylindrical copper-water heat pipe with a copper screen-wick is used. The copper heat pipe has an outer diameter of 1.91 cm and an inner diameter of 1.73 cm. The length of the heat pipe is 89 cm, with a long evaporator section of 60 cm and shorter condenser section of 20 cm. A water jacket is used to achieve convective cooling at the condenser. All the other parameters used in the experiment or derived from the experiment (e.g., effective power throughput, convective heat transfer coefficient in the cooling jacket, etc.) are given in detail in [5].

The temperature evolution predictions of the presented model, its comparison with the experimental and numerical results of previous works and boundary condition at the evaporator are shown in Figure 3.4. For both the presented model and the experimental results from [27], displayed temperatures are the average of the sections. In this case, the modelled heat pipe is divided into only nine cells in the axial direction.

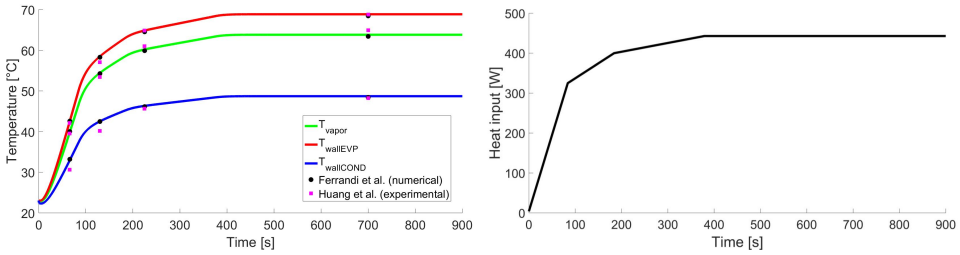

Figure 3.4: Transient modelling results: a) Comparison with Ferrandi et al. [5] and Huang et al. [27]; b) Heat input at the evaporator.

As seen in Figure 3.4, the presented model shows excellent agreement with the numerical results of [5] and the experimental results of [27]. The reason for the small difference of 2.0% between the current model and the experimental results is attributed to the measurement uncertainty as well as the derived parameters. Since these derived parameters are extracted from [5], the deviation between the results of [5] and the current model is limited to 0.5% only.

3.4.2. Steady-state behaviour validations

To validate the results of the current model at steady-state, first, the results of the analytical work by Bertossi et al. [11] for a rotating heat pipe are used. Following this validation, the results of the experimental work and the numerical work by Song et al. [10, 18] are compared to the current model.

In [11], the simulated RHP has an inner diameter of 0.4 cm and a length of 20 cm. The model results are investigated for different fill ratios and heat inputs, keeping the rotational speed fixed at 3,000 RPM and the temperature difference between the evaporator and adiabatic section wall temperatures at 10 °C. Since model parameters such as the fluid properties are explicitly documented in [11],

differences between the model predictions would be caused by the underlying assumptions and model limitations (e.g., mesh size) only.

The results of the liquid height distribution and the heat flow along the heat pipe are compared in Figure 3.5. As stated in Subsection 3.3.5, a finer mesh in the axial direction is required for very low fill ratios. Therefore, the axial mesh number is 108 for the lowest fill ratio case and 36 for all other cases.

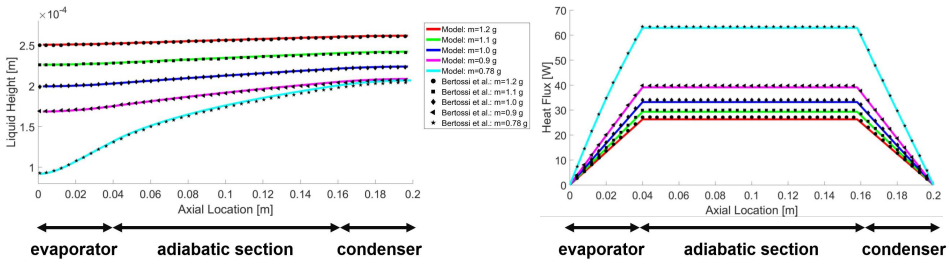

Figure 3.5: Steady-state modelling results and comparison with Bertossi et al. [11]: a) Liquid height distribution; b) Heat flow along the heat pipe.

Again, the agreement between the presented model and the reference steady-state model [11] is excellent. The average deviation in the heat flow along the heat pipe between the two models is calculated as 2.1%. This deviation is attributed to the fact that the conduction in the liquid layer is approximated as a conduction through a plane layer in Bertossi et al [11]. In the presented model, thermal resistance through the liquid layer is calculated with the radial resistance as given in Eq. 3.1. In the results, it is seen that a heat flow of 63 W is required to obtain 10 °C difference between the evaporator and the adiabatic section for the lowest fill ratio case, whereas this value is only 26 W for the highest fill ratio. This is caused by the higher thermal resistance of the liquid component when the liquid film is thicker as it is observed in Figure 3.5.

Another validation is performed for a copper-water cylindrical RHP with an outer diameter of 25.4 mm and a total length of 400 mm [18]. The heat pipe is filled with 6.3 g of distilled water and the rotational speed is 4,000 RPM. During the experiments, heat is applied with an inductor coil, whereas a water jacket is used for cooling. For both the experiments and the numerical model, overall thermal resistance of the heat pipe is plotted against varying heat input. During the validation, natural convection at the evaporator is accounted for [10].

The results of the current model, the experiments from [18] and the numerical model from [10] are shown in Figure 3.6. The uncertainties of the thermal resistances caused by measurement errors are computed for a 95% confidence interval.

It is seen that the agreement of the current model with the experimental results is good. All of the calculated thermal resistances are within the uncertainty limits of the experimental results. The predictions of the current model are also in line with the results of the numerical model by Song et al. [10], having an average deviation of 6.2%. Some of this deviation can be attributed to the fact that axial conduction

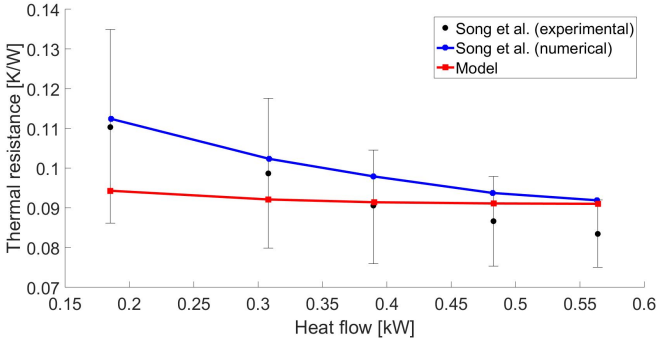

Figure 3.6: Overall thermal resistance results and comparison with the experiments by Song et al. [18] and the numerical model by Song et al. [10]

through the copper wall is not accounted for in [10]. This results in estimating a higher overall thermal resistance compared to the prediction of the current model.

3.5. Results and discussion

The results of the presented model are explored in more detail at various boundary conditions for both CDHP and RHP.

A heat pipe with container material SAE 304 using water as a medium was examined. The heat pipe has a length of 0.2 m, inner diameter of 0.045 m and a wall thickness of 1 mm. In the case of the CDHP, the wick is also made of SAE 304 and it has a thickness of 1 mm. The wick porosity is 0.9, the wick permeability is 0.0015 mm^2 and the effective pore radius is 54 µm, similar to the wick properties reported in [7]. The fill ratio is 4.4%. The lengths of the evaporator and the condenser are 0.05 m each. The heat input and output are fixed at 200 W.

3.5.1. Effect of Operating Temperature on Vapor Dynamics

For a heat pipe operating at steady-state, the operating temperature and the heat flow have a direct influence on the vapor velocity. Using the presented model, the effect of the operating temperature on vapor dynamics is investigated for four cases. The operating temperatures for these four cases are 50 °C, 75 °C, 100 °C and 120 °C, respectively. For all cases, same amount of heat is transferred. The simulation results for the vapor velocity along the heat pipe are shown in Figure 3.7.

It is observed that the vapor velocity shows an increasing trend when the operating temperature becomes lower. The maximum vapor velocity was obtained with the vapor temperature of 50 °C where the vapor velocity was 0.7 m/s. This is caused by a low vapor density because of the low vapor pressure at low temperature. To be able to calculate the vapor velocity is especially important in order to avoid the sonic limit. At or near the sonic limit, the temperature distribution along the vapor channel becomes significantly non-isothermal. The results also show that

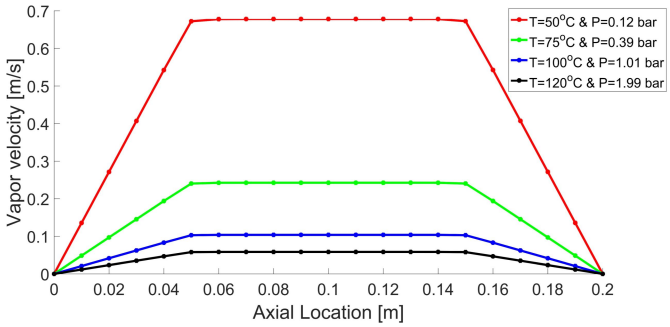

Figure 3.7: Vapor velocity along the heat pipe at different operating temperatures.

the vapor velocity profile at the evaporator and the condenser is nearly linear, which together with the boundary conditions of a uniform heat flux at the evaporator and condenser implies that the evaporator and condenser temperatures are uniform.

3.5.2. Effect of Rotational Speed on Liquid Height Distribution

The rotational acceleration, along with the liquid head, is the driving force of liquid transport from the condenser to the evaporator for a rotating heat pipe. An increase in the rotational speed allows for the same amount of liquid transported with a lower liquid head. Five cases with rotational speeds of 250, 300, 500, 750, and 1,000 RPM are compared in Figure 3.8.

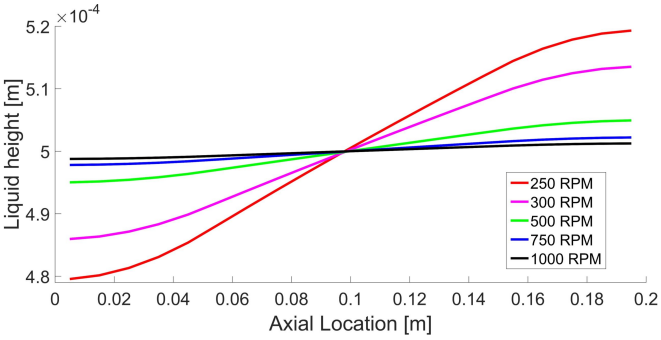

Figure 3.8: Liquid height distribution along the heat pipe.

The comparison between the cases clearly shows that the head required to replace the same amount of liquid is much lower when the rotational speed is increased. With a rotational speed of 250 RPM, the required head is 40 µm, whereas it is only 2.5 µm for a rotational speed of 1,000 RPM. Therefore, while determining the minimum fill ratio for a rotating heat pipe application, the effect of the centrifugal force on the liquid height distribution needs to be taken into account. For heat pipes operating at lower rotational speed, more liquid is needed to prevent dry-out.

3.5.3. Computational efficiency

In order to quantify the computational efficiency of the model, two cases presented in 3.4.2 are executed using different mesh sizes until they reached steady-state. The comparison between different mesh sizes is made in terms of computational time and relative error in the computed heat transferred through the heat pipe. The results are presented in Table 3.1, in reference to the execution with the finest mesh (80 cells in the axial direction).

Table 3.1: Computational efficiency.

Case	Mesh size	Computational time	Relative error
m = 1.2 g	80	100% (Ref)	0% (Ref)
	40	28.7%	<0.01%
	20	9.0%	0.01%
	10	3.2%	0.06%
m = 0.9 g	80	100% (Ref)	0% (Ref)
	40	29.4%	0.04%
	20	9.6%	0.16%
	10	3.4%	0.55%

It is observed that a doubling in the mesh size approximately triples the computational time. On the other hand, the relative error does not change significantly for the tested cases when the mesh size is halved. As noted in Section 3.3.5, the accuracy is compromised more when the fill ratio is lower. However, the relative error is kept at an acceptable level even with the lowest mesh size.

3.6. Conclusions

In this chapter, a new engineering model applicable to both cylindrical CDHPs and RHPs has been developed. The numerical model describes the transient behavior of the heat pipe with a 2D axisymmetric geometry.

The model offers sufficient accuracy and level of detail concerning the interior dynamics of the heat pipe in combination with fast execution. At each axial location, the heat pipe is divided into three components, namely the wall, the liquid and the vapor. The liquid and the vapor cells in each axial location are allowed to change size radially so that the total volume is conserved. This gives the unique advantage to track the liquid / vapor interface without the need for fine meshing or re-meshing. In order to achieve this, the equations for mass, momentum and energy are adapted to the meshing method.

The developed model shows excellent agreement with experimental, numerical and analytical studies found in the literature for CDHPs and RHPs. The model can be used to efficiently explore load cases, for example changing operating temperature and rotational speed.

With this model, the interior dynamics of cylindrical heat pipes can be simulated with a low computational cost and high accuracy. This will be instrumental in the

modelling of the whole heat pipe assisted annealing plant. It is also beneficial for engineering and design applications where the information that is supplied by thermal network models is not detailed enough, yet the computational cost of CFD cannot be afforded.

References

[1] A. Faghri and C. Harley, *Transient lumped heat pipe analyses,* Heat Recovery Systems and CHP **14**, 351 (1994).

[2] Z. Zuo and A. Faghri, *A network thermodynamic analysis of the heat pipe,* International Journal of Heat and Mass Transfer **41**, 1473 (1998).

[3] Y. Xuan, Y. Hong, and Q. Li, *Investigation on transient behaviors of flat plate heat pipes,* Experimental Thermal and Fluid Science **28**, 249 (2004).

[4] T.-E. Tsai, G.-W. Wu, C.-C. Chang, W.-P. Shih, and S.-L. Chen, *Dynamic test method for determining the thermal performances of heat pipes,* International Journal of Heat and Mass Transfer **53**, 4567 (2010).

[5] C. Ferrandi, F. Iorizzo, M. Mameli, S. Zinna, and M. Marengo, *Lumped parameter model of sintered heat pipe: Transient numerical analysis and validation,* Applied Thermal Engineering **50**, 1280 (2013).

[6] W. W. Wits and J. B. Kok, *Modeling and validating the transient behavior of flat miniature heat pipes manufactured in multilayer printed circuit board technology,* Journal of heat transfer **133**, 081401 (2011).

[7] J.-M. Tournier and M. El-Genk, *A heat pipe transient analysis model,* International Journal of Heat and Mass Transfer **37**, 753 (1994).

[8] A. B. Solomon, K. Ramachandran, L. G. Asirvatham, and B. Pillai, *Numerical analysis of a screen mesh wick heat pipe with cu/water nanofluid,* International Journal of Heat and Mass Transfer **75**, 523 (2014).

[9] T. Daniels and F. Al-Jumaily, *Investigations of the factors affecting the performance of a rotating heat pipe,* International Journal of Heat and Mass Transfer **18**, 961 (1975).

[10] F. Song, D. Ewing, and C. Ching, *Fluid flow and heat transfer model for high-speed rotating heat pipes,* International Journal of Heat and Mass Transfer **46**, 4393 (2003).

[11] R. Bertossi, N. Guilhem, V. Ayel, C. Romestant, and Y. Bertin, *Modeling of heat and mass transfer in the liquid film of rotating heat pipes,* International Journal of Thermal Sciences **52**, 40 (2012).

[12] Z. Uddin, S. Harmand, and S. Ahmed, *Computational modeling of heat transfer in rotating heat pipes using nanofluids: A numerical study using pso,* International Journal of Thermal Sciences **112**, 44 (2017).

[13] H. Hassan and S. Harmand, *Effect of using nanofluids on the performance of rotating heat pipe,* Applied Mathematical Modelling **39**, 4445 (2015).

[14] C. Harley and A. Faghri, *Two-dimensional rotating heat pipe analysis,* Journal of Heat Transfer **117**, 202 (1995).

[15] S. Patankar, *Numerical heat transfer and fluid flow* (CRC press, 1980).

[16] J. Baker, R. Ponnappan, and J. Leland, *A computational model of transport within a rotating heat pipe,* in *37th Aerospace Sciences Meeting and Exhibit* (1999) p. 1070.

[17] W. Lian, W. Chang, and Y. Xuan, *Numerical investigation on flow and thermal features of a rotating heat pipe,* Applied Thermal Engineering **101**, 92 (2016).

[18] F. Song, D. Ewing, and C. Ching, *Heat transfer in the evaporator section of moderate-speed rotating heat pipes,* International journal of heat and mass transfer **51**, 1542 (2008).

[19] N. Zhu and K. Vafai, *Analysis of cylindrical heat pipes incorporating the effects of liquid–vapor coupling and non-darcian transport—a closed form solution,* International Journal of Heat and Mass Transfer **42**, 3405 (1999).

[20] M. Aghvami and A. Faghri, *Analysis of flat heat pipes with various heating and cooling configurations,* Applied Thermal Engineering **31**, 2645 (2011).

[21] D. Reay, R. McGlen, and P. Kew, *Heat pipes: theory, design and applications* (Butterworth-Heinemann, 2013).

[22] G. Hansen, E. Næss, and K. Kristjansson, *Analysis of a vertical flat heat pipe using potassium working fluid and a wick of compressed nickel foam,* Energies **9**, 170 (2016).

[23] P. Nemec, A. Čaja, and M. Malcho, *Mathematical model for heat transfer limitations of heat pipe,* Mathematical and Computer Modelling **57**, 126 (2013).

[24] S. Chan, Z. Kanai, and W. Yang, *Theory of a rotating heat pipe,* Journal of nuclear energy **25**, 479 (1971).

[25] L. Lin and A. Faghri, *Heat transfer in micro region of a rotating miniature heat pipe,* International Journal of Heat and Mass Transfer **42**, 1363 (1999).

[26] F. Song, D. Ewing, and C. Ching, *Experimental investigation on the heat transfer characteristics of axial rotating heat pipes,* International Journal of Heat and Mass Transfer **47**, 4721 (2004).

[27] L. Huang, M. S. El-Genk, and J.-M. Tournier, *Transient performance of an inclined water heat pipe with a screen wick,* ASME-PUBLICATIONS-HTD **236**, 87 (1993).

4

Heat pipe at high temperatures

4.1. Introduction

As stated in Subsection 1.3.2, the working fluid is a critical component of the heat pipe operation. Being the thermal energy carrier of the system, its thermophysical properties should be compatible with the application to guarantee proper functioning.

The temperature range that has to be covered for the heat pipe assisted annealing project is very large: from 25 °C to 700 °C. Even considering the theoretical limits for the operation of working fluids (between the triple point and the critical point), this temperature range requires the employment of multiple working fluids. The practical ranges for working fluids are even more constraining due to the operating limits of rotating heat pipes (RHPs), namely the viscous limit, the sonic limit, the entrainment limit and the boiling limit (see Figure 1.10.

Additionally, there are application specific constraints to the selection of working fluids. These can be summarized as: performance of the working fluid, safety aspects (working fluid handling and vapor pressure) and life time of the working fluid (which can deteriorate due to thermal degradation and chemical reactions with the shell material). Considering all these aspects, it is relatively easy to choose a working fluid for the low temperature range as it has been widely investigated and applied. There is a consensus around water as a high performance working fluid for the temperature range from 25 °C to 150 °C. For the higher temperature range, however, the selection requires a more detailed investigation.

Therefore, the current chapter aims to answer the following research question:

> *What are the applicable working fluids for the high temperature range (150 °C to 700 °C) of the heat pipe assisted annealing concept?*

First, a literature review is made to select the working fluids. In the second part of this chapter, a life time test is carried out to test the stability of a specific working fluid (phenanthrene). This life time test is performed in thermosyphons. At the final part of the chapter, another selected working fluid (Dowtherm A) is used in a rotating heat pipe setup to test its applicability and its performance. These tests were done for the temperature range between 150 °C and 350 °C.

4.2. Working fluid selection

A systematic approach is adopted for the selection of the working fluids. As described above, there are a number of criteria that determine the suitability of a working fluid for a certain application. On this ground, the working fluids are evaluated with respect to each of these criteria. Since water is a well-tested high performing working fluid for the low temperature range, the focus will be on higher temperatures (> 150 °C).

4.2.1. Vapor pressure

The investigation on the suitability of working fluids for higher temperatures focuses on three different material groups: organics, halides and elements. The practically applicable range for a number of working fluids for high temperatures is shown in

Figure 4.1 [1–6]. As a reference, water is also added to the figure. In this figure, the suitability of the working fluids is either judged based on experience or based on the vapor pressures of the fluids with the lowest allowed vapor pressure to be 0.01 bar and the highest corresponding to the pressure at 100 °C below the critical point [2]. It should be noted that a vapor pressure lower than 0.01 bar can also be feasible as long as the sonic and the viscous limits are avoided.

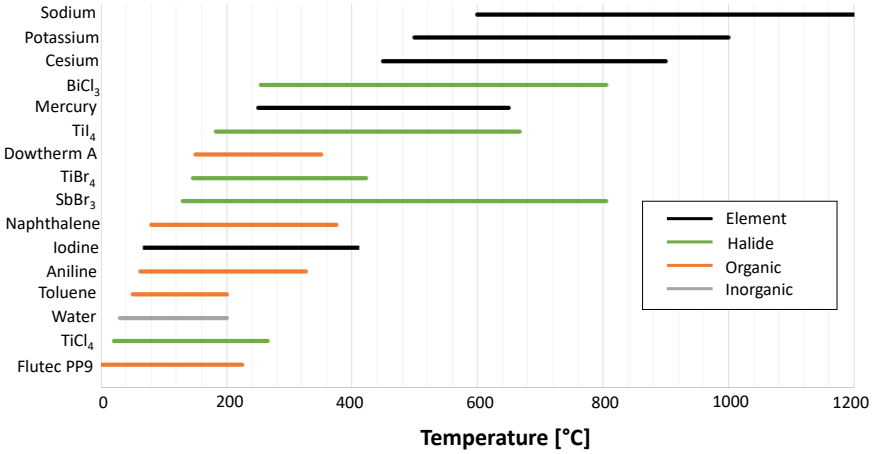

Figure 4.1: Selection of intermediate / high temperature working fluids and indicative temperature ranges.

As shown in Figure 4.1, organics mainly cover the intermediate temperatures and they mainly consist of aromatic compounds such as toluene, aniline, naphthalene and Dowtherm A (a eutectic mixture of biphenyl and diphenyl ether). The halides and the elements are suitable for both intermediate and high temperatures.

4.2.2. Life time

With the vapor pressures as the starting point, the next step is to evaluate the life time of the working fluids. For the organics, thermal decomposition is critical, whereas chemical reactions with the shell material mostly play a role for the halides and metals. The main concern with thermal decomposition and chemical reactions with the shell material is that they create non-condensable gases causing the performance of the heat pipe to drop and in some cases to render part of the heat pipe completely ineffective. The effect of the non-condensable gases in an RHP is illustrated in Subsection 4.4.3. In other cases, polymerization of an organic fluid is a problem and can result in a significant increase in the liquid viscosity, ultimately decreasing the fluid circulation capacity [7]. Yet another failure mode is caused by the accumulation of the solid deposit at the evaporator, creating hot spots and disturbing normal functioning of the heat pipe [1, 8].

Life time of working fluids is usually determined with long duration tests in capillary-driven heat pipes or thermosyphons at the target temperature or short

duration tests at elevated temperatures. During the tests, the temperature difference between the evaporator and the condenser of the heat pipe is measured. An increase in this temperature difference during the test points to the formation of non-condensable gases. Another diagnosis method can be a destructive analysis at the end of the life time test where the working fluid and the shell material are examined.

Organic fluids have the tendency to isomerize and / or break into smaller molecules. This tendency increases with higher concentration levels of impurity [9]. Moreover, following the Arrhenius equation, the reaction rates increase with increasing temperatures. This is clearly illustrated in the tests carried out by Anderson et al. [10] where Dowtherm A is tested at both 400 °C and 450 °C and the temperature difference between the evaporator and the condenser are plotted against test duration [7].

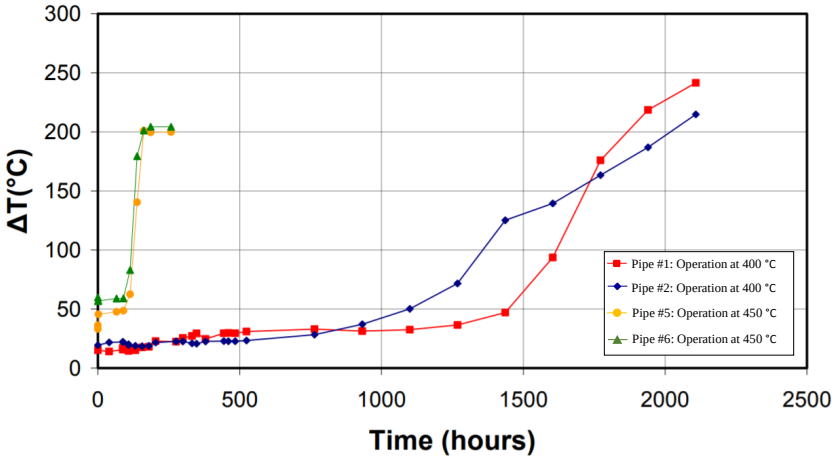

Figure 4.2: Elevated temperature life time tests with Dowtherm A / 304 SS [7]. *(legends added to the figure)

The life time tests on most common organic compounds for the intermediate temperature range are compiled in Table 4.1 [1]. A similar comprehensive list is also available in [7, 11]. All of the organic fluids in Table 4.1 qualify as aromatic compounds. This is because the compounds with an aromatic ring structure tend to be more stable compared to long-chained hydrocarbons [12].

Table 4.1: Life time tests of organics.

Fluid	Shell	T [°C]	t [h]	Outcome	Ref.
Toluene	Ti 99.4	250	8,760	OK	[13]
	CuNi10Fe	280	8,760	OK	[13]
	St35	250	26,280	OK	[13]

[1] In shell materials, CS: carbon steel, SS: stainless steel, St: stainless, MS: mild steel.

	13CrMo44	250	26,280	OK	[13]
	SS 316L	280	26,280	OK	[13]
Naphthalene	Al	218	3,570	OK	[12]
	CS	217	3,570	OK	[12]
	St35	270	26,280	OK	[13]
	13CrMo44	270	26,280	OK	[13]
	Ti 99.4	300	8,760	OK	[13]
	SS 316L	320	8,760	OK	[13]
	CuNi10Fe	320	8,760	OK	[13]
	Ti	320	3,000	OK	[14]
o-terphenyl	CS	273	27,796	OK	[12]
	CS	283	3,570	OK	[12]
	Al	290	672	Fail	[12]
o-terphenyl / m-terphenyl	13CrMo44	320	8,760	Fail	[13]
	13CrMo44	400	8,760	Fail	[13]
	SS 316L	350	8,760	Fail	[13]
	SS 316L	400	8,760	Fail	[13]
Biphenyl	CS	267	1,675	OK	[12]
	Al	275	2,014	Fail	[12]
	13CrMo44	250	8,760	OK	[13]
	SS 316L	270	8,760	OK	[13]
	13CrMo44	400	8,760	Fail	[13]
	SS 316L	400	8,760	Fail	[13]
	SS 316	350	5,520	OK	[15]
	SS 304	475	72	Fail	[16]
	SS 304	465	100	Fail	[16]
	SS 304	422	366	Fail	[16]
Dowtherm A	MS	250	8,383	OK	[16]
	SS 304	268	24,500	OK	[16]
	SS 304	400	1,200	OK	[16]
	SS 304	391	1,200	OK	[16]
	St34	340	~ 13,000	Fail	[17]
	St37	210	~ 17,500	OK	[17]
	Al	200	~ 13,000	OK	[17]
	SS 304	345	1,000	OK	[7]
	SS 304	450	180	Fail	[7]
	SS 304	400	1,770	Fail	[7]
	Ti	406	~ 2,000	Fail	[7]
	SS	399	144	Fail	[9]

In Table 4.1, it is seen that naphthalene is suitable up to 320 °C, whereas Dowtherm A is mostly stable up to around 300 °C. There are mixed results for Dowtherm A between 300 °C and 400 °C and above 400 °C it decomposes in a relatively short period of time. Another organic fluid, o-terphenyl, is stable up to 283 °C. Toluene is another promising organic fluid stable up to 280 °C.

There are some aromatic compounds that have not been tested. A prominent candidate is phenanthrene for which the boiling point is 336 °C. Phenanthrene has been reported as a very stable compound and therefore, it can also be considered as a potential working fluid [18].

As for the halides and elements, the summary of life time tests is shown in Table 4.2 [2]. Again, a more comprehensive list can be found in [7, 11].

Table 4.2: Life time tests of halides and elements.

Fluid	Shell	T [°C]	t [h]	Outcome	Ref.
$SnCl_4$	Al	165	2,210	Fail	[12]
	CS	152	3,570	OK	[12]
	CS	156	27,750	OK	[19]
$TiBr_4$	CP-Ti	380	20,040	Fail	[11]
$TiCl_4$	Al	165	2,210	Fail	[12]
	Ti	227	4,019	OK	[20]
	Hastelloy	300	59,184	OK	[11]
$AlBr_3$	Hastelloy	400	58,992	OK	[11]
	Al	227	4,290	Fail	[20]
	CP-Ti	227	1,100	Fail	[20]
$GaCl_3$	CP-Ti	340	19,632	Fail	[11]
$SbBr_3$	Al	227	5,000	Fail	[20]
$SbCl_3$	CS	203	5,000	Fail	[19]
Mercury	SS	330	10,000	OK	[21]
Cesium	Ti	400	~ 2,000	OK	[1]
	Nb1%/Zr	1000	8,700	OK	[1]
Potassium	Nb1%/Zr	~ 550	~ 4,000	OK	[22]
	SS 304	510	6,100	OK	[1]
	SS 347	650	6,100	OK	[1]
	Ni	600	16,000	OK	[1]
Sodium	Inconel 718	700	~ 87,000	OK	[23]
	SS	700	~ 87,000	OK	[23]
	Hastelloy	715	~ 33,000	OK	[1]
	Nb1%/Zr	1,100	~ 1,000	OK	[1]

[2] In shell materials, CS: carbon steel, SS: stainless steel, CP: commercially pure.

It is seen in Table 4.2 that elements covering the high temperature range are fairly stable. Halides, on the other hand, show a strong dependecy on the temperature as well as on the heat pipe shell material.

First Saaski et al. [12] and then Tarau et al. [24] have described a simple model to calculate the tendency of a certain halide to react with a heat pipe shell material based on the electromotive force difference of the reaction between the working fluid and the shell material. Such a reaction can be described as follows:

$$\alpha M_a + \beta M_b H_c \rightleftharpoons \alpha M_a H_d + \beta M_b \tag{4.1}$$

Where α and β are stoichiometric coefficients, M_a is the metallic container, $M_b H_c$ is the working fluid halide and $M_a H_d$ and M_b are the products of the reaction. The electromotive force difference for a hypothetical corrosion cell of two electrodes each consisting of a pure metal and its halide (one electrode with M_a and $M_a H_d$ and the other electrode with $M_c H_c$ and M_b) would correlate with the spontaneity of the reaction or a lack thereof. With the assumption that the electromotive force difference is equal to the standard electromotive force difference, it can be expressed as the difference in the decomposition potentials of the two halides as shown in Eq. 4.2.

$$\Delta E = \Delta E^\circ = E_{p_{M_a H_d}} - E_{p_{M_b H_c}} \tag{4.2}$$

Where ΔE is the electromotive force difference, ΔE° is the standard electromotive force difference and E_p is the decomposition potential. A positive ΔE° implies that the reaction can occur spontaneously, whereas a negative ΔE° shows that the probability of the reaction shown in Eq. 4.1 is low.

The theory is in good agreement with the experimental data. Therefore, the combinations of halides and shell materials can be further investigated. In general, aluminium is not a suitable shell material whereas molybdenum, iron and carbon steel are suitable shell materials. Stainless steel is a favorable shell material in most cases, with the exception of bismuth trichloride, antimony trichloride and tin tetrachloride [24]. A major limitation of this theory is that it is not time-dependent. It should also be noted that a thin coating of the interior surface of a heat pipe with a favorable material can increase the pairing possibilities.

4.2.3. Performance

As explained in Subsection 1.3.2 of this thesis, the thermophysical properties of a working fluid directly affect the heat pipe performance in terms of its heat transfer capacity and efficiency. For an RHP, liquid viscosity is important such that a viscous fluid requires a larger pressure difference between the condenser and the evaporator to ensure working fluid circulation when all the other conditions are the same. A higher liquid density is favorable as it allows for the storage of more energy

in a smaller volume. Therefore, a higher liquid density increases the merit of the working fluid. A high liquid thermal conductivity is crucial as it reduces the thermal resistance through the liquid layer. This is especially important for the condenser where only thermal conduction plays a role in the heat transfer through the liquid layer. Finally, a high latent heat of vaporization allows for the same amount of energy transport with a lower fluid amount.

Conventionally, the performance of a working fluid has been summarized with a figure of merit for capillary-driven heat pipes and thermosyphons. The same logic has been applied to RHPs by Daniels et al. [25]. It has been described as follows:

$$\mathcal{M} = \frac{\rho_l^2 H_{fg} k_l^3}{\mu_l} \tag{4.3}$$

Where ρ_l is the liquid density, H_{fg} is the latent heat of vaporization, k_l is the liquid thermal conductivity and μ_l is the liquid viscosity.

This merit number is derived based on the assumption that the efficiency of the condenser directly determines the heat pipe performance. Although this is not always correct and especially the extent of natural convection at the evaporator as well as the flow pattern strongly affect the overall performance of the heat pipe, the figure of merit is a strong indicator of the performance of a working fluid (see Table 1.1). In this respect, the figures of merit of several working fluids near their boiling points are displayed in Figure 4.3 [3].

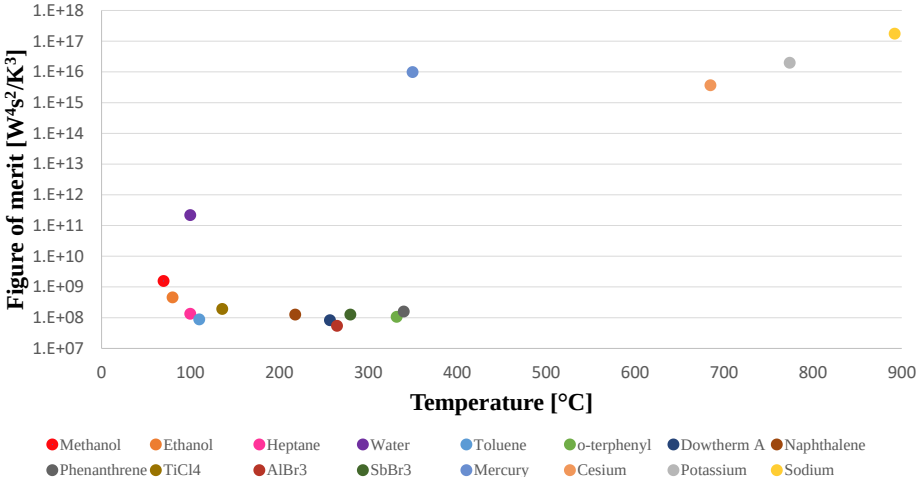

Figure 4.3: Figure of merit for a number of working fluids in RHP near their boiling points.

In Figure 4.3, it is clearly seen that water outperforms any other liquid at the lower temperature range. This is largely caused by its high latent heat and relatively

[3] Liquid properties are obtained from [1, 2, 15, 26–31].

high thermal conductivity. Organics and halides perform poorly, especially due to their low thermal conductivity. Similarly, elements have orders of magnitude higher merit figures mainly due to their extremely high thermal conductivity which is at least two orders of magnitude higher than that of organics and halides.

4.2.4. Safety

The safety aspects of an RHP are in general no different compared to other types of heat pipes. A good summary of the safety considerations for all types of heat pipe is provided in [1].

First and foremost, it should be remembered that in most cases heat pipes are pressure vessels. Therefore, the thickness of the heat pipe shell should be designed according to the shell material as well as the working fluid and maximum operating temperature. However, the heat pipe shell is a thermal resistance and its thickness directly influences the performance of the heat pipe. Moreover, in some cases, the heat pipe weight is crucial. This is the case in the heat pipe assisted annealing application as well, since the RHPs are relatively large and are only supported from the two ends. A heavy weight can cause buckling in the long-term. Consequently, the pressure inside the heat pipe should not exceed a certain threshold. In this respect, water is especially dangerous as its vapor pressure increases relatively faster than many other fluids. For the current application, the aim is to not exceed 5 bar interior vapor pressure to avoid thick walls and buckling.

Another safety aspect to consider is the reactivity and toxicity of working fluids. Although mercury is a very favorable working fluid with respect to its vapor pressure covering most of the intermediate region and its very high performance, it is highly toxic. Naphthalene is also undesirable as it is classified as carcinogenic, mutagenic or reprotoxic (CMR). Most alkali metals and halides, on the other hand, react violently with air and water [1, 32]. Although continuous annealing takes place in an atmosphere composed of N_2 and H_2, this reactivity should be kept in mind to minimize potential failure.

4.2.5. Preliminary selection

Taking into account life time, safety and performance of the working fluids, a selection that covers the whole temperature range from room temperature to 700 °C can be made. The criteria that weigh the most are safety and life time of the working fluids.

For the temperature range from 25 °C to 150 °C, water outperforms any other working fluid. At temperatures higher than 150 °C, water should be avoided mainly due to its rapidly increasing vapor pressure. Water, in combination with stainless steel, generates H_2 inside the heat pipe. However, high permeation rate of H_2 can result in self-venting [33]. It is not clear whether the temperature range covered with water will be of relevance to the current application. This will further be discussed in Chapter 5.

For the intermediate temperature range, there is no consensus on the working fluids with good environmental and toxicity properties. The options for this range are mercury, halides and organics. Due to its high toxicity, mercury is elim-

inated. Halides can provide an option mostly with a thin coating inside the heat pipe to prevent chemical reaction with the shell material. They also tend to be stable with superalloys. However, both of these options are relatively expensive and they should not be the immediate choice. Moreover, halides are highly reactive. Although this is not per se an insurmountable problem, it increases the risk of failure. Therefore, as a first option, the intermediate temperature will be covered by organic fluids. Looking at the life time tests, Naphthalene and Dowtherm A are proven options. Since naphthalene is classified as CMR, Dowtherm A will be selected. Dowtherm A is stable at the temperatures up to 300 °C and potentially up to 350 °C for 1 year. Organics covering the temperature range between 300 °C to 450 °C are more scarce. A prominent option is phenanthrene which has not yet been tested so far. However, it has been reported to be very stable. Therefore, it is selected as the working fluid to cover the temperature range between 300 °C and 450 °C. It should be noted that its stability is recommended to be further tested.

Finally for the higher end of the range, alkali metals are proven options. Although they are highly reactive, they have no other alternatives. In this respect, the vapor pressure of cesium seems suitable for the temperature range between 450 °C and 700 °C. Cesium can also operate below 450 °C as long as viscous and sonic limits are avoided. An alternative to cesium can be potassium, which can operate at a slightly higher temperature range compared to cesium.

All in all, the vapor pressures of the selected working fluids and the temperature range they cover are shown in Figure 4.4

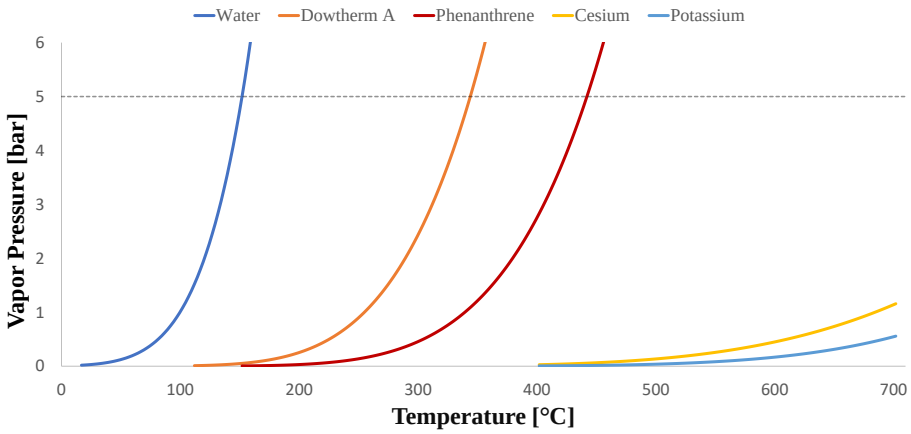

Figure 4.4: Preliminary selection of the working fluids for the heat pipe assisted annealing line.

It is clear that there is no alternative to cesium and potassium for the high temperatures. In case further investigation on organics demonstrates that they are not suitable due to stability issues, their applicability window should be limited or halides should be used in combination with a thin coating. Due to the similar merit numbers of organics and halides, a drastic difference in performance is not expected whether halides or organics are used for the heat pipe assisted annealing

concept.

4.3. Working fluid stability experiments

Phenanthrene has been determined as a potential working fluid for the temperature range from 300 °C to 450 °C as explained in Section 4.2. Although it has been previously reported as a stable aromatic hydrocarbon [18], it is not tested before in a conventional life time test like other organics shown in Table 4.1. The aim of this section is to understand whether phenanthrene is adequately stable in long-term for the maximum intended temperature. This is accomplished through experiments. Functional requirements of the experiments are listed below.

- Phenanthrene should be constantly kept at 450 °C (~ 5.5 bar) for a duration of at least 3 months.
- The container for phenanthrene should be made of stainless steel, as it is the intended heat pipe material for the final line.
- Phenanthrene should be at saturated condition at all times and should not interact with components other than the container material.
- Temperature gradient caused by the presence of the non-condensable gas inside the heat pipe should be detected.

4.3.1. Experimental setup and methodology

Following these functional requirements, the testing methodology is determined. The basic idea is to test the performance of thermosyphons filled with phenanthrene before and after they are subjected to a high temperature. To do this, first, thermosyphons are tested with a known amount of heat input, at steady-state and at a relatively low temperature. The temperature distribution along the heat pipe wall in different axial locations are measured. Then, they are placed in a furnace at around 450 °C for a duration of 3 months (see Figure 4.5). The heat pipes are later tested in the same setup and conditions as they were before being placed in the furnace. Any deterioration of performance indicated by a thermal gradient will signal the decomposition of phenanthrene. Finally, the thermosyphons can be subject to a destructive test for the identification of decomposed material.

The thermosyphons are made of stainless steel (type 316L). They have a length to diameter ratio that is bigger than the heat pipes that are expected to be used in the heat pipe assisted annealing line. The length to diameter ratio (L/D ratio) of the heat pipe is important such that a greater L/D ratio enables easier detection of non-condensable gases. The non-condensable gases reveal themselves under load either as a temperature gradient between the evaporator and condenser of the heat pipe or as a complete blocking of part of the condenser. The greater the L/D ratio, the more accentuated these effects are. The length of the thermosyphons is limited by the size of the furnace to be used. Consequently, the length of the thermosyphons vary between 145 mm to 165 mm. To keep the L/D ratio as desired, the inner diameter is selected as 10.22 mm.

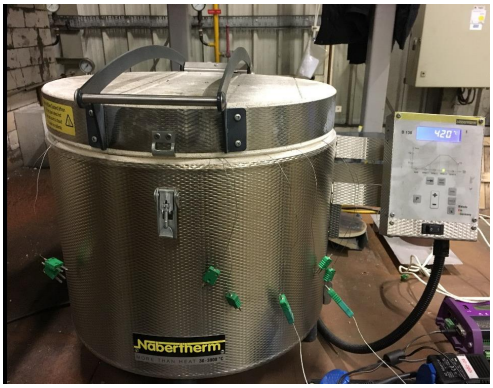

Figure 4.5: Nabertherm furnace used in life time tests.

A heating wire suitable for high temperatures is used for the supply of the thermal load to individual thermosyphons during the initial and final performance tests. The heating wire does not supply uniform heating. This is problematic because it would negatively affect the reliability of the temperature measurement at the evaporator. Therefore, the heating wire is wound over a copper sleeve which is soldered to the evaporator of the thermosyphons. The heat input is controlled with a PLC. The heating wire is covered with insulation. The adiabatic section is also covered with the same insulation material. As for the cooling, natural convection is used. For some of the tests, the condenser part is also partially covered to increase the surrounding temperature and to make sure that phenanthrene does not freeze at the condenser.

The temperatures along the thermosyphon are measured with K-type thermocouples attached to the wall at 6 different axial locations. 2 of the thermocouples measure the temperatures at the evaporator outer wall and they are placed inside the grooves between the copper sleeve and the thermosyphon. One thermocouple is welded on the wall at the adiabatic section and it measures the wall temperature which is representative of the vapor temperature inside the thermosyphon. The remaining three thermocouples are welded to the condenser outer wall. The temperatures are logged every 5 seconds. The experimental setup is shown in Figure 4.6.

In total, 10 thermosyphons are produced. Before filling and permanently closing the heat pipes, they are cleaned with acetone and outgassed in the furnace at a temperature of 450 °C. Once the thermosyphons are outgassed, filling and sealing are carried out. 6 thermosyphons are filled with phenanthrene (one with 99.5% purity and 5 with 98% purity). With the filled amount, the evaporator of the thermosyphons is fully covered with the working fluid at the operating temperatures. The other 4 thermosyphons are filled with Dowtherm A. Dowtherm A is expected to deteriorate at 450 °C in a relatively short period of time [7]. It is thus introduced to the test as a control, to validate that the testing method can detect non-condensable gas formation.

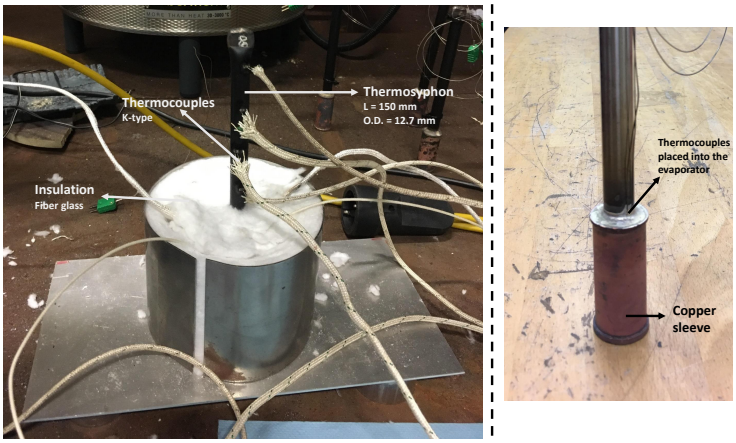

Figure 4.6: Tests with thermosyphons.

The specifications of the setup and experiments are given in Table 4.3.

Table 4.3: Setup specifications.

Parameter	Data
Thermosyphon material	SS 316L
Thermosyphon length	145 mm - 165 mm
Evaporator length	51.2 mm
Adiabatic section length	25 mm - 30 mm
Condenser length	64 mm - 90 mm
Thermosyphon O.D.	12.7 mm
Thermosyphon wall thickness	1.24 mm
Heat input	10 W - 25 W
Insulation material	Fiber glass
Phenanthrene amount	4.1 g
Dowtherm A amount	4.0 g
Furnace temperature	460 °C
Test duration	3 months

4.3.2. Results and discussion

The initial tests carried out before the thermosyphons are placed inside the furnace show that there are various amounts of non-condensable gas inside each thermosyphon. This is due to the failure of a proper filling and sealing procedure which resulted in a certain amount of air trapped inside the thermosyphon. As it will be explained in Subsection 4.4.2, the same problem is also present in the larger RHP setup. An example for the temperature distribution of a thermosyphon with a large amount of air trapped is shown in Figure 4.7 for two different operating

temperatures.

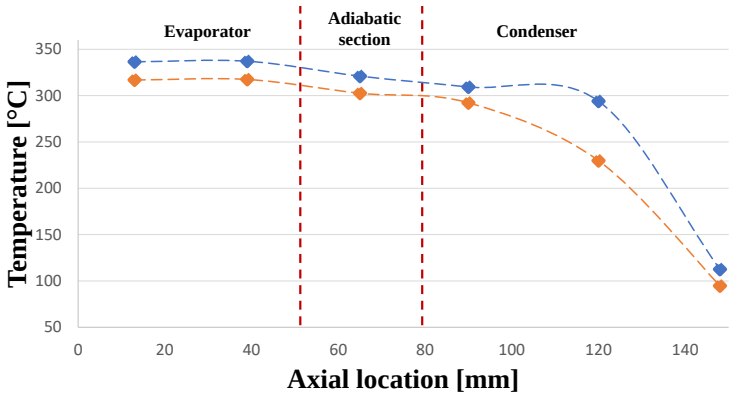

Figure 4.7: Temperature distribution of a thermosyphon with non-condensable gas.

In Figure 4.7, the presence of non-condensable gas is visible as a large temperature gradient at the condenser of the heat pipe. When the operating temperature is higher, the effective length of the condenser becomes larger, as expected. Higher operating temperatures bring about higher vapor pressures of the working fluid. This implies a smaller ratio of non-condensable gas to vapor, resulting in the lower impact of non-condensable gas. A similar behavior has been investigated and modelled for naphthalene thermosyphons by Mantelli et al. where non-condensable gas weakens the thermal performance of the thermosyphon [34].

The presence of air in all of the filled and sealed thermosyphons is problematic in two ways: first, it can make the detection of the generation of non-condensable gas more difficult and second, it may cause the generation of non-condensable gas due to oxidation rather than thermal decomposition. Still, the tests are carried out.

After the initial tests and before the thermosyphons are placed inside the furnace, two of the thermosyphons (one with phenanthrene 98% and the other with Dowtherm A) are spared for destructive test. The other thermosyphons are placed inside the furnace. After three months, they are tested again at similar conditions as before.

The tests carried out for the detection of the non-condensable gas showed that the performance of all of the 8 thermosyphons significantly deteriorated. The thermal performance of a Dowtherm A thermosyphon and a phenanthrene thermosyphon are shown in Figures 4.8 and 4.9, respectively. In these figures, the same thermal load is applied to each thermosyphon before and after they were exposed to high temperature for 3 months.

In these figures, the generation of non-condensable gas is visible in two ways. The first one is the larger temperature gradient at the condenser section for the thermosyphons which were exposed to high temperature for 3 months. This can also be interpreted as a decrease in the length of the active region of the condenser. Another way of looking at the effect of the non-condensable gas is by

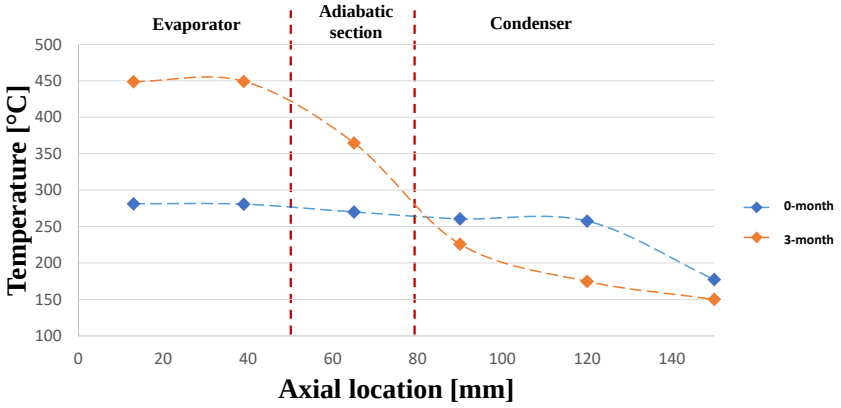

Figure 4.8: Temperature distribution of a Dowtherm A thermosyphon before and after exposure to high temperature for 3 months.

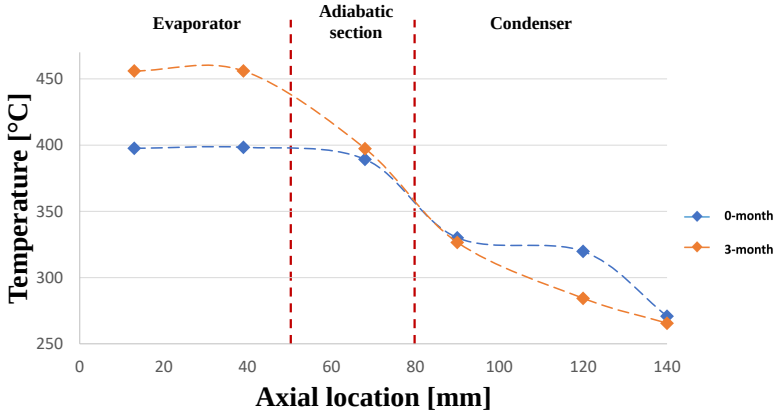

Figure 4.9: Temperature distribution of a phenanthrene thermosyphon before and after exposure to high temperature for 3 months.

observing the evaporator temperature. Because a similar amount of heat (not exactly the same amount due to the losses through the insulation) is applied during the tests and steady-state is reached, the condenser should reject a similar amount of heat during the initial and final tests. Since the overall thermal resistance of the thermosyphon substantially increases due to the presence of the non-condensable gas, the evaporator temperature increases further to accommodate the condenser temperature.

When the thermosyphons have been cut after the final tests, it was observed that the thermosyphons subject to long-term high temperature had an overpressure inside (inside pressure above ambient pressure). Moreover, all of the Dowtherm A and a high proportion of phenanthrene have been converted into char. Nor the overpressure neither the conversion of a high amount of Dowtherm A and phenanthrene are not likely to occur only by oxidation as the oxygen level inside the heat pipe is limited. Therefore, it is clear that both materials have thermally decomposed. However, it is not clear whether the oxidation process itself and its products facilitated the decomposition.

Additionally, Dowtherm A that has been used as the working fluid in the RHP setup explained in Section 4.4 has been analyzed with gas chromatography (GC). The fluid had a total operating time of approximately 80 hours and a maximum operating temperature of 350 °C. It was also exposed to air during operation. The GC analysis showed the presence of phenol, naphthalene and dibenzofuran in the sample. This points to the breakdown of Dowtherm A to smaller aromatic compounds. These aromatic compounds are illustrated in Figure 4.10.

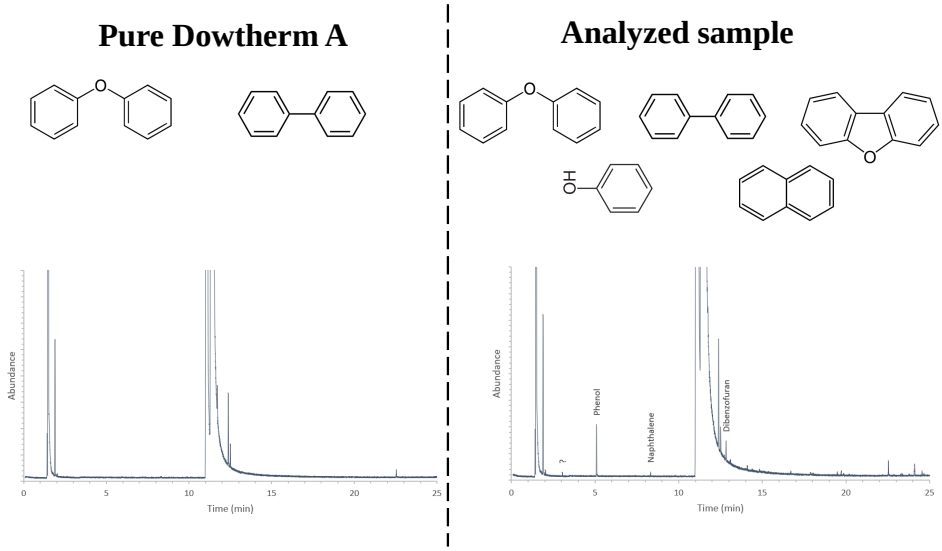

Figure 4.10: GC analysis results for the Dowtherm A sample.

In the light of the above information, it is concluded that the method used in this section proves to be useful in the detection of non-condensable gases. How-

ever, it is suggested that the life time tests with phenanthrene are repeated with several improvements. First, a much better vacuum should be established in the thermosyphons. Second, phenanthrene should be tested at multiple temperatures, not only at the maximum temperature of the intended temperature range. Finally, intermediate performance tests should be made (e.g. every month) before the final performance test. The same procedure can be applied to Dowtherm A thermosyphons at a lower temperature range (e.g. 300 °C to 350 °C).

4.4. Rotating heat pipe experiments

As motivated in Section 4.2, Dowtherm A has been selected as a potential working fluid for the temperature range of 150 °C to 350 °C. Dowtherm A has been previously tested and used in thermosyphons [35–38], however it has not been tested as a potential working fluid in an RHP setup before. Dowtherm A has a low figure of merit number (see Figure 4.3). Therefore, the objective of this section is to first understand whether Dowtherm A is an applicable working fluid for the RHP and then, to test its performance at different conditions, especially to interpret the implications of its low figure of merit number.

4.4.1. Literature review

There have been numerous experimental studies on RHPs published in the literature. The objectives of these studies were understanding the physics involved, generating results for model validation and evaluating the performance of the heat pipes. With respect to design, axially rotating RHP setups that were investigated can be classified into three: perfectly cylindrical RHPs, tapered RHPs and RHPs with a modified design (stepped wall or with wick / coil structure).

An important early study by Marto featured an RHP with a stepped evaporator and a tapered condenser with a 1° inclination filled with water, ethanol or Freon [39]. In this comprehensive study, an important outcome was that a higher rotational speed increases the overall performance of the tapered RHP characterized by total thermal resistance. Moreover, the detrimental effect of non-condensable gas is shown to decrease with increasing operating temperature. This is expected as the ratio of non-condensable gas amount to vapor amount decreases with increasing operating temperature. Daniels et al. used a similar RHP geometry with Arcton-113 (trichlorotrifluoroethane) and acetone to study the effects of non-condensable gas on the temperature distribution and heat load characteristics [40]. Similarities with stationary heat pipes have also been shown. Ponnapan et al. worked on a tapered RHP at moderate (7,000 RPM) and high (30,000 RPM) rotational speeds [41, 42]. The RHP was filled with water and methanol and the merits of these working fluids were compared. For moderate rotational speeds, the maximum heat transport capacity with water was almost two times as it was with methanol. Similar observations have been made at high rotational speeds as well. An interesting conclusion at high rotational speeds was that the Nusselt condensation film theory did not agree well with the experimental results.

Different condenser geometries have been compared to each other by Marto et

al. and it was shown that both tapered condenser and an internally finned condenser considerably outperformed an ordinary cylindrical condenser configuration [43]. In another study, Marto et al. investigated the effect of different types of fins such as straight axial fins, spiralled fins and helical corrugations [44]. The best heat transfer performance was reached with spiralled fins, which not only increased the heat transfer area but also facilitated the liquid flow back to evaporator. The performance increase with longitudinal grooves in the condenser compared to a perfectly cylindrical condenser has been shown by Vasiliev et al. [45]. Heat transfer characteristics of a coil-inserted RHP have been studied by Lee et al. [46]. Similar to spiral fins, a coil helped with the pumping of the liquid to the evaporator, especially at low rotational speeds. Several studies used RHPs with a wick structure to help the liquid flow back to evaporator [47–49].

As suggested in the review by Peterson [50], earlier studies on cylindrical RHPs with or without a stepped evaporator mainly focused on the flow pattern of the working fluid. Experimental studies were no exception. An experimental study by Krivosheev et al. showed that beyond a certain rotational speed, the flow pattern becomes annular and the thermal resistance of the heat pipe significantly increases [51]. Moreover, between the formation of the annular flow and its collapse, a hysteresis region is found. Semena et al. measured the liquid layer thickness by electric contact and demonstrated the existence of a hysteresis region [52]. In the same study, an expression for the liquid layer thickness is developed.

Hashimoto et al. performed visualization experiments with an acrylic heat pipe to study the variation of the flow regime with rotational speed [53]. The critical Froude number for the collapse of annular flow is studied by Lin et al. [54]. In another study, Lin et al. examined the heat transfer at the condenser of a stepped wall heat pipe in the hysteresis region [55]. In yet another study, the liquid film thickness distribution and the corresponding heat transfer coefficients were examined by Lin et al. via a cylindrical and stepped wall RHP [56]. Analytical expressions purely based on a hydrodynamic analysis were obtained in the same study and they showed excellent agreement with the experimental results in the non-annular flow regimes that were obtained in [57]. With both of these studies, it was shown that heat rate effects can be neglected while quantifying the liquid layer thickness and the associated heat transfer coefficients in non-annular flow regimes. Previous studies on the Froude number defining the collapse of the annular flow are extended with the calculation of the critical numbers for the onset and complete formation of annular flow by Baker et al. through a set of experiments with an acrylic RHP [58].

A set of experiments on cylindrical and tapered RHPs has been carried out by Song et al. [59, 60]. In these studies, it was found that the heat transfer mechanism at the condenser section can be modelled reasonably well by considering radial conduction only, whereas at the evaporator, natural convection plays a role at sufficiently high Rayleigh number. Accordingly, a model to predict the thermal resistance at the evaporator was developed. It was shown that natural convection considerably improves the heat transfer at the evaporator section of the RHP compared to the condenser section (see Figure 4.11). In [61], methanol, ethanol and

water were tested in a tapered RHP considering natural convection heat transfer at the evaporator. A good agreement with the model proposed by Song et al. [59] has been found with water as working fluid. With methanol and ethanol, the agreement with the model was poor. In two recent experimental studies, Xie et al. investigated the performance of stepped wall heat pipe filled with ammonia [62], whereas Lian et al. carried out experiments on an RHP with a cone-shaped condenser [63].

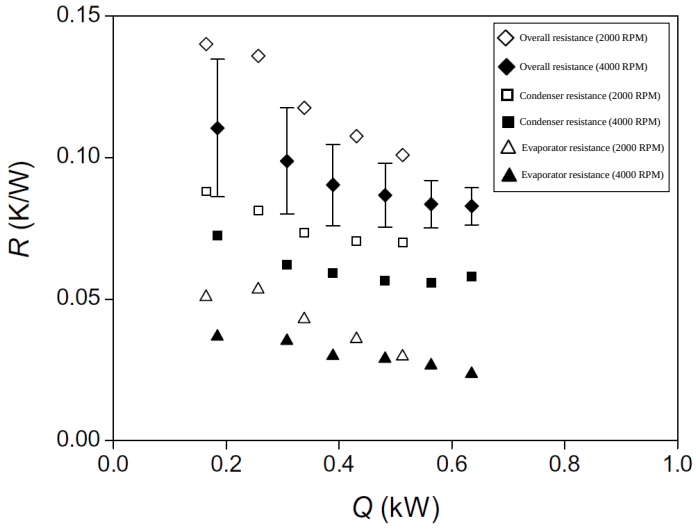

Figure 4.11: Thermal resistance at the evaporator and condenser sections of a cylindrical RHP [59]. *(legends added to the figure)

4.4.2. Experimental setup

Previous studies and applications of RHPs (summarized in Subsections 1.3.3 and 4.4.1) did not focus on the intermediate and high temperature applications of RHPs. Heat pipe assisted annealing application requires the use of RHPs in the intermediate and high temperatures as well. However, selected working fluids in the intermediate range have a low figure of merit as shown in Figure 4.3. In the light of this information, an RHP setup suitable to be used at the intermediate temperature range (between 150 °C and 350 °C) with Dowtherm A is designed and built.

The RHP that is manufactured in the current study has an effective working length of 497 mm and it is made of SS 316. It has an inner diameter of 44 mm, yielding an L/D ratio of 11.3. The wall thickness is selected to be 8 mm, relatively large to accommodate heat flux sensors at different axial locations. The heat pipe is connected to the motor on one side, and to the slip ring on the other side in order to transfer the measured signals to the data logger. The heat pipe is supported on both sides by specially designed bearing blocks suitable for high temperature and thermal elongation in the radial and axial directions (see Figure 4.12). The maximum rotational speed that can be reached is 1090 RPM. The evaporator has a length of 158 mm, whereas the condenser is 187 mm. At the evaporator end of

the heat pipe, there is a 63 mm region of dead zone where very low heat input / output is present. This region was necessary to accommodate the heating oven.

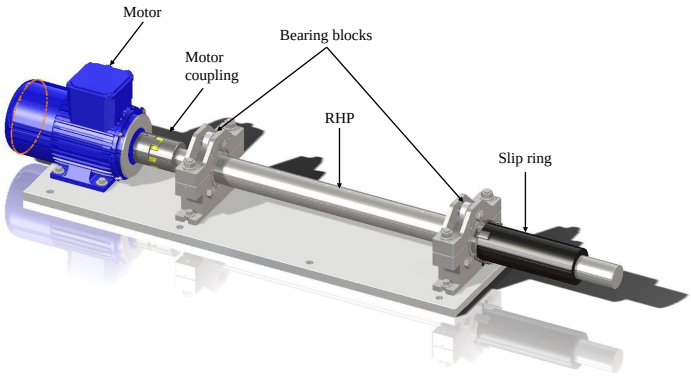

Figure 4.12: CAD view of the experimental setup.

Heating is achieved via IR heaters, 6 quartz lamps 12 mm O.D., having the same length as the evaporator and capable of reaching a maximum temperature of 900 °C. The IR heaters are shielded with steel hemicylinders to form an oven. The evaporator section of the heat pipe is coated with a heat-resistant organic black paint to increase the effectiveness of the heating. Cooling, on the other hand, is achieved via forced convection with air. To isolate the condenser section from the adiabatic section, a cooling duct is placed. Moreover, mist cooling nozzles are placed in the cooling duct. However, they were never use as sufficient cooling was achieved with air only. The adiabatic section is insulated with fiber glass. The setup can be seen in operation in Figure 4.13.

There are 4 K-type thermocouples inside the heat pipe measuring the vapor temperature at different axial locations. One of these thermocouples is placed in the middle of the evaporator, one is in the middle of the adiabatic section and the other two are at the condenser section. Unfortunately, the 5^{th} thermocouple placed at the end of the condenser was damaged. Inside the wall of the heat pipe, there are 6 heat flux sensors measuring the heat flux at different axial locations. The first two heat flux sensors are at the beginning and the middle of the evaporator, respectively. The third heat flux sensor measures the heat flux at the intersection of the evaporator and the adiabatic section, whereas the fourth sensor is placed at the adiabatic region. Finally, the last two sensors are at the condenser. Exact locations of the sensors are shown in Table 4.4. Each heat flux sensor consists of 4 thermocouples connected to each other in series. One of these thermocouples also measures the temperature. In this way, wall temperatures at different axial locations are also measured. All of the thermocouple leads are directed to a hollow axis placed at the center of the heat pipe. This hollow axis exits the heat pipe and the leads are then connected to the slip ring. Additionally, pressure inside the heat pipe is measured with a sensor. Data from the sensors are collected with a data logger and processed using LabVIEW.

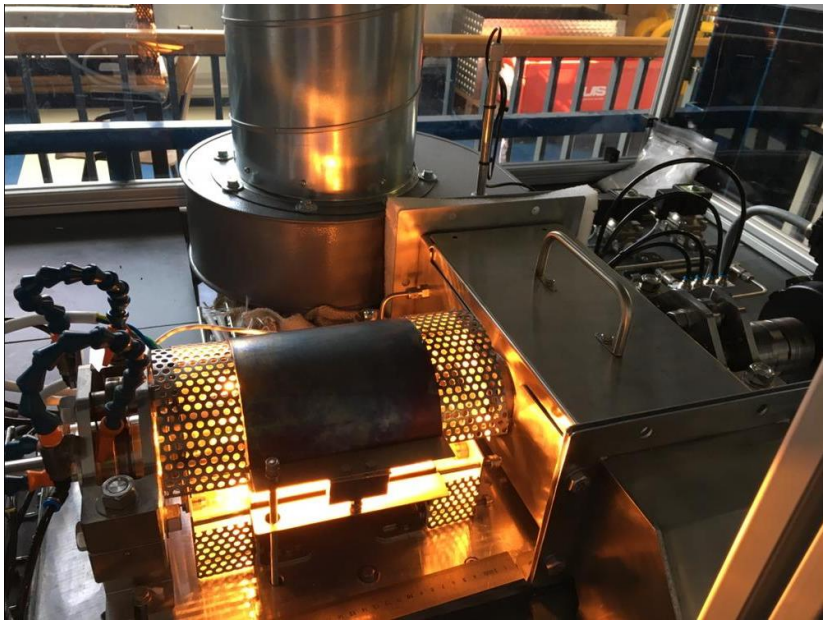

Figure 4.13: RHP setup in operation.

Table 4.4: Sensor locations.

Sensor type	Location 0 mm: evaporator end
Thermocouple inside the RHP	TC1: 74.0 mm TC2: 240.5 mm TC3: 324.0 mm TC4: 407.0 mm
Heat flux sensor and thermocouple on the RHP wall	HF1: 55.6 mm HF2: 111.1 mm HF3: 222.2 mm HF4: 277.8 mm HF5: 388.9 mm HF6: 444.4 mm

During manufacturing of the setup, an eccentricity formed along the axial direction of the RHP. The middle of the RHP is 0.36 mm off-center compared to the two ends of the RHP. This is problematic in two-ways: first, balancing of the RHP should be made to reach high rotational speeds and second, liquid flow inside the heat pipe will be disturbed. Balancing of the heat pipe is achieved by adding weight to the heat pipe with a clamp. However, as it will be shown in Subsection 4.4.3, the effect of the eccentricity is severe and it limits the learnings from the experiments.

Another problem with the setup was the lack of vacuum, as previously mentioned. This lack of vacuum is exacerbated due to a leak into the heat pipe, possibly from the location where the wires exit.

The tests are carried out with two similar fill ratios: 10.5% and 11.8% at room temperature. The fill ratio changes due to liquid density change and vapor amount at different operating temperatures. Rotational speed varied between 150 RPM and 1090 RPM. The amount of air inside the RHP varied during different runs, from a corresponding pressure of 0.2 bar to 0.35 bar at ambient temperature. Maximum operating temperature was 350 °C.

For the calculation of the heat fluxes from the sensor readings, the distance between the thermocouples and the conductivity of the material separating the thermocouples were used. For each data point used for the calculation of the thermal resistance at the evaporator and the condenser, steady-state conditions were established. The data were analyzed in real-time to determine whether steady-state conditions were actually reached.

The heater does not provide a perfectly uniform heating profile. In order to deduce the heating and thus, the heat flux profile, the temperature profile at and near the heater is measured with an IR camera at different operating temperatures and heat inputs. With this profile, the heat flux at locations where there is no heat flux sensor is derived. Heat losses from the adiabatic section and the condenser are assumed to be uniform, although the effect of non-condensable gas at low operating temperatures may invalidate this assumption at the condenser. For this reason, general deductions are made for high operating temperature cases.

Heat transfer rates into the evaporator and out of the condenser and adiabatic section with the associated uncertainties are compared to each other in Figure 4.14. It is observed that the heat input rates are systematically higher than the heat output rates. Beside the error in the sensors, the reason for this difference is expected to be the axial heat losses from the two ends of the heat pipe which are directly connected to the bearing blocks.

4.4.3. Results and discussion

A typical case for the heating up of the heat pipe to a high operating temperature with increasing lamp power is shown in Figure 4.15. In this figure, the temperatures inside the heat pipe are shown with the relevant thermocouple locations summarized in Table 4.4. In this specific case, the amount of non-condensable gas is around 0.25 bar at ambient temperature. The rotational speed is kept constant at 150 RPM.

The detrimental effect of non-condensable gas is clearly seen since a temperature gradient inside the RHP is observed especially at low temperatures. The thermocouple near the middle of the condenser (TC4) starts to show an increase in temperature only after the thermocouple at the evaporator (TC1) exceeds 200 °C. This temperature gradient decreases with increasing temperature, as expected. Steady-state is established at 339 °C. At this temperature, the difference between the operating temperature and TC4 reduces to 6 °C. With this outcome, it is clearly seen that Dowtherm A can be used as a thermal energy carrier in the RHP for

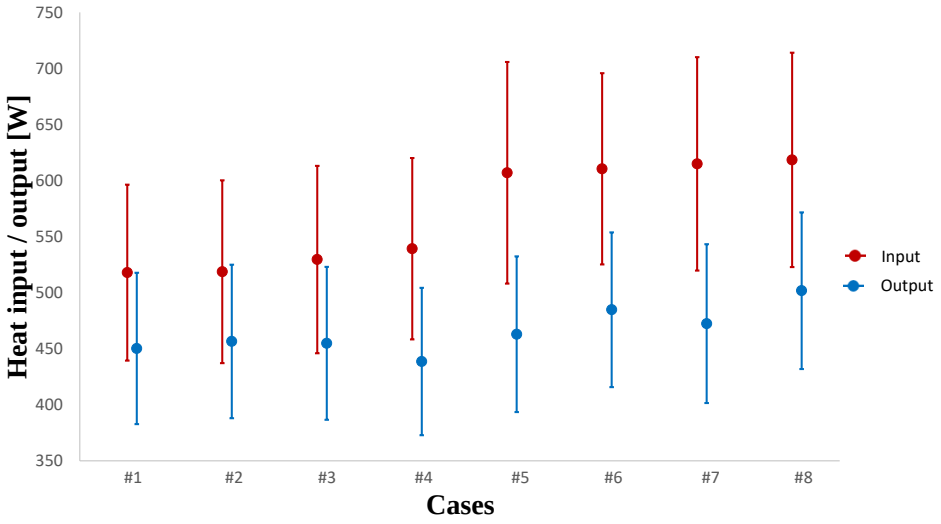

Figure 4.14: Comparison of heat input to and output from the heat pipe.

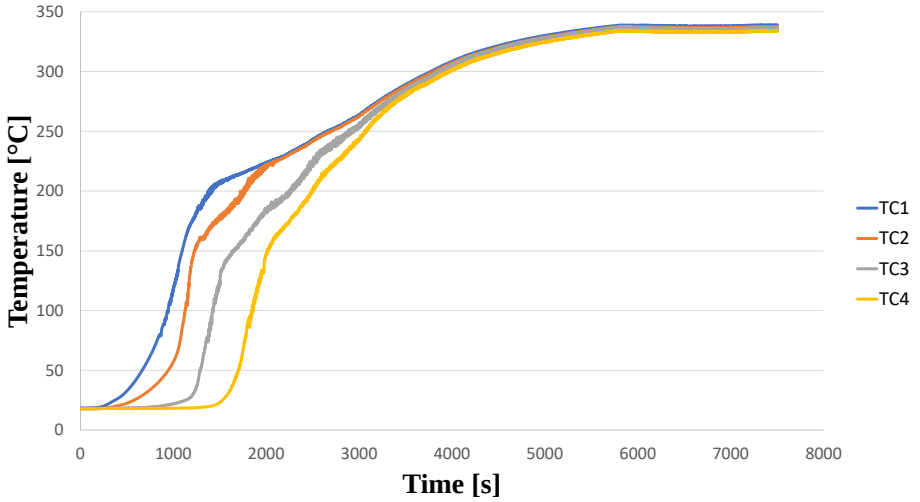

Figure 4.15: RHP heating up to 350 °C with Dowtherm A at 150 RPM.

intermediate temperatures.

At high heat input (630 W) and relatively high rotational speed (~725 RPM), local dryout at the evaporator has been observed as shown in Figure 4.16. The dryout is visible as a sudden change in the interior temperatures of the heat pipe, where the evaporator temperature increases whereas the condenser temperature decreases. This shows that the heat that is received at the evaporator is not transferred to

the condenser through vapor convection. This dryout is unexpected at this heat input rate (630 W) and rotational speed. Moreover, the dryout is normally more likely to occur at lower rotational speeds rather than higher rotational speeds as it was shown in Figure 3.8. Therefore, the reason for this dryout is most likely the disturbance of the liquid flow due to the eccentricity of the heat pipe.

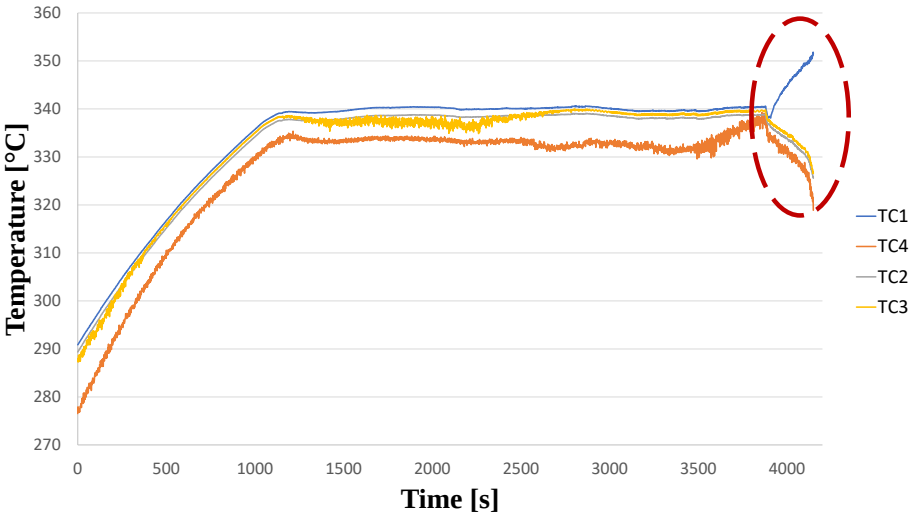

Figure 4.16: Dryout at the evaporator at 725 RPM.

With increasing rotational speed, the amount of liquid pulled against gravity also increases. Once the critical Froude number is reached, the flow pattern becomes annular [56, 58]. With the eccentricity of the heat pipe, rotational speed plays an extra role: with increasing rotational speed, more liquid flows to the high point of eccentricity. If there is annular flow and the fill ratio is high enough to compensate for the eccentricity, its effect would be less. In the dryout case, the actual Froude number (Fr = 12.9) is lower than the critical Froude number for the onset of the annular flow (Fr = 15.4) and for the complete annular flow (Fr = 29.5). It is known that the evaporator and the condenser are affected by the annular flow when the critical Froude number is between the onset and the complete annular flow [56, 58]. Therefore, it is unlikely that at the investigated condition, annular flow is established at the evaporator. This confirms that the increasing rotational speed combined with the heat pipe eccentricity results in the disturbance of the flow.

Although eccentricity of the heat pipe severely affects the liquid layer distribution and the flow, thermal resistances caused by the liquid layer at the condenser and the evaporator are computed and compared to the theoretical outcomes.

The model developed in Chapter 3 includes the calculation of the RHP in an annular flow regime. When the flow regime is not annular, the amount of liquid pulled towards the upper part of the RHP needs to be calculated. As described in Subsection 4.4.1, various studies focused on this issue. In order to determine the

flow pattern, the dimensionless Froude number is calculated (see Eq. 4.4) and then compared to the critical Froude number for onset and complete annular flow in a finite cylinder (see Eq. 4.5 and 4.6) [58].

$$\mathrm{Fr} = \frac{\omega^2 \, r_i}{g} \tag{4.4}$$

$$\mathrm{Fr}_{\mathrm{c_{onset}}} = 9.60(1-\chi)^{-2.967} \tag{4.5}$$

$$\mathrm{Fr}_{\mathrm{c_{complete}}} = 20.03(1-\chi)^{-2.421} \tag{4.6}$$

Where Fr is the Froude number, ω is the rotational speed, r_i is the inner radius of the heat pipe, g is gravity $\mathrm{Fr_c}$ is the critical Froude number and χ is the fill ratio.

An analytical expression developed by Lin et al. allows for the calculation of the average pulled liquid layer thickness in the non-annular flow regime. In this case, heat transfer is assumed to take place only through the thin liquid film that is pulled by rotation. The average thickness of the thin liquid film is calculated with Eq. 4.7, whereas angle of the liquid pool is calculated using Eq. 4.8 [56].

$$\overline{\delta} = \frac{5}{6} \frac{r_i}{\sqrt{\frac{\rho_l \, g \, r_i}{\mu_l \, \omega}}} \tag{4.7}$$

$$\chi = \frac{1}{2\pi}(\theta - \sin\theta) \tag{4.8}$$

Where $\overline{\delta}$ is the average liquid layer thickness, ρ_l is the liquid density, μ_l is the liquid viscosity and θ is the angle of the liquid pool.

Liquid resistance is calculated as follows.

$$R_l = \frac{\ln\left(\frac{r_i}{r_i - \overline{\delta}}\right)}{(2\pi - \theta) \, k_l \, \Delta z} \tag{4.9}$$

Where R_l is the liquid thermal resistance, k_l is the liquid thermal conductivity and Δz is the axial length. In case of natural convection at the evaporator, Eqs. 3.19 - 3.21 are also used.

In Figure 4.17, experimentally observed and theoretically calculated thermal resistances at the uniformly heated part of the evaporator (62 mm) and the condenser (same length as for the evaporator for better comparison) at an operating temperature of 340 °C are shown. The heat input and output are kept constant.

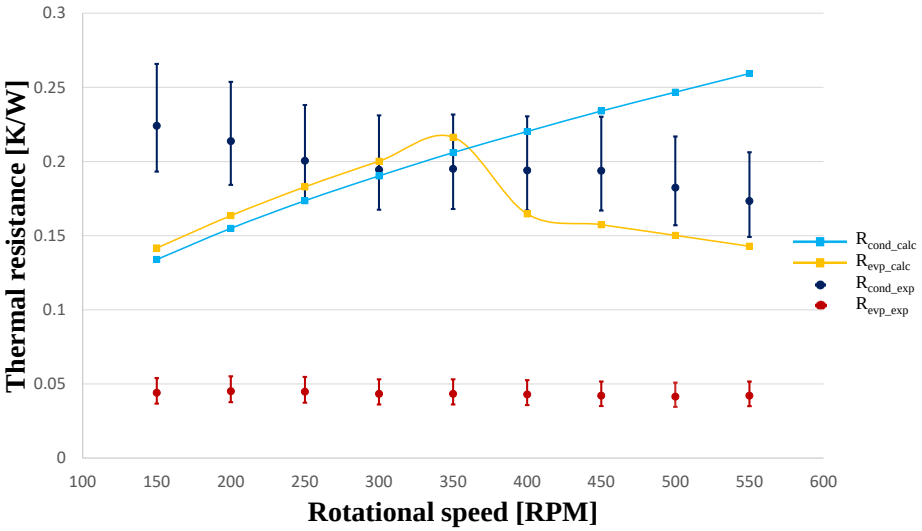

Figure 4.17: Experimentally observed and calculated thermal resistances at the evaporator and the condenser.

It is clearly observed that the experimentally observed and theoretically calculated thermal resistances at the evaporator are altogether different. Looking at the calculated thermal resistance, it is seen that it increases until 350 RPM because more fluid is pulled following Eq. 4.7. With higher rotational speed, natural convection starts to play a role and the resistance decreases. The experimental thermal resistance remains more or less constant with increasing RPM. It is 3 to 5 times lower than the calculated thermal resistance. The average thickness of liquid layer to reach this extremely low thermal resistance is ~25 µm. Along with the observation of dryout shown in Figure 4.16, this points to the severe disturbance of the liquid flow inside the RHP.

At the condenser, although the values of experimentally observed and theoretically calculated thermal resistances are closer to each other, the trends do not agree. It is expected that the average pulled liquid layer thickness and thus, the associated thermal resistance, increases with increasing rotational speed. This trend is clear in Figure 4.17. However, the experimental results show a weak and yet opposite trend.

Additionally, both experimental and theoretical values show that the non-annular flow regime increases the efficiency of the RHP. This is especially important for fluids of low figure of merit such as organics. For comparison, the same amount of fluid in annular flow would result in a thermal resistance of 1.95 K/W at the condenser side. At the evaporator, on the other hand, this difference would be much less drastic and the thermal resistance would decrease with increasing rotational speed due to natural convection. Therefore, during the implementation of the heat pipe assisted annealing line, the heat pipes filled with Dowtherm A and phenanthrene

should have a fill ratio that ensures a non-annular flow regime.

4.5. Conclusions

In this chapter, potential working fluids for the intermediate and high temperature range of the heat pipe assisted annealing concept are identified and tested. This is important because the thermophysical properties of the fluids as well as their stability, performance and risks are critical for the proper operation of the concept.

In order to achieve this objective, potential working fluids are narrowed down with a comprehensive literature review. This review encompassed criteria such as the vapor pressure of the fluid, its life time, its figure of merit and its safety aspects. This selection yielded three different working fluids: Dowtherm A (150 °C to 350 °C), phenanthrene (300 °C to 450 °C) and cesium (450 °C to 700 °C). For the high temperature range, potassium can be an alternative to cesium. For the organics, on the other hand, halides in combination with a suitable shell material can be an alternative.

Phenanthrene has not been previously tested in a conventional life time test like other fluids. Therefore, in order to test the long-term stability of phenanthrene at the intended maximum temperature, life time tests are designed and carried out. This involved the fabrication of thermosyphons filled with phenanthrene which were tested before and after they were exposed to ~460 °C for 3 months. In order to check the effectiveness of the method, several thermosyphons were also filled Dowtherm A, with the expectation that they would certainly decompose and thus, deteriorate in performance. The test results showed thermal decomposition of phenanthrene subjected to ~460 °C for 3 months. However, it is suggested that the life time tests with phenanthrene and Dowtherm A are repeated with a better initial vacuum and at multiple temperatures.

In the final section of this chapter, Dowtherm A is tested in an RHP. This is accomplished in an RHP setup specifically designed to operate at the intermediate temperature range. With these tests, it is shown that Dowtherm A is suitable to be used in an RHP at the designated temperature range in terms of performance. Although it has a low figure of merit especially compared to water and alkali metals, it can still be sufficiently efficient when annular flow is avoided. Thermal resistances at the evaporator and condenser are experimentally observed and these observations are compared to well-established theoretical outcomes. The theoretical outcomes were close to the observations at the condenser, whereas they were very different at the evaporator. The main reason for this difference is predicted to be the eccentricity of the RHP which occurred during its production.

References

[1] D. Reay, R. McGlen, and P. Kew, *Heat pipes: theory, design and applications* (Butterworth-Heinemann, 2013).

[2] A. Devarakonda and W. G. Anderson, *Thermo-physical properties of intermediate temperature heat pipe fluids,* in *AIP Conference Proceedings*, Vol. 746 (AIP, 2005) pp. 179–186.

[3] W. G. Anderson, J. H. Rosenfeld, D. Angirasa, and Y. Mi, *Evaluation of heat pipe working fluids*

in the temperature range 450 to 700 k, in *AIP Conference Proceedings*, Vol. 699 (AIP, 2004) pp. 20–27.

[4] E. A. Brandes and G. Brook, *Smithells metals reference book* (Elsevier, 2013).

[5] S. Kim, P. A. Thiessen, E. E. Bolton, J. Chen, G. Fu, A. Gindulyte, L. Han, J. He, S. He, B. A. Shoemaker, *et al.*, *Pubchem substance and compound databases,* Nucleic acids research **44**, D1202 (2015).

[6] P. J. Linstrom and W. Mallard, *Nist chemistry webbook; nist standard reference database no. 69,* (2001).

[7] W. Anderson, *Intermediate temperature fluids for heat pipes and loop heat pipes,* in *5th International Energy Conversion Engineering Conference and Exhibit (IECEC)* (2007) p. 4836.

[8] S.-T. Tu, H. Zhang, and W. Zhou, *Corrosion failures of high temperature heat pipes,* Engineering Failure Analysis **6**, 363 (1999).

[9] C. Lang and B. Lee, *Heat transfer fluid life time analysis of diphenyl oxide/biphenyl grades for concentrated solar power plants,* Energy Procedia **69**, 672 (2015).

[10] W. Anderson, R. Bonner, P. Dussinger, J. Hartenstine, D. Sarraf, and I. Locci, *Intermediate temperature fluids life tests-experiments,* in *5th International Energy Conversion Engineering Conference and Exhibit (IECEC)* (2007) p. 4808.

[11] W. G. Anderson, S. Tamanna, C. Tarau, J. Hartenstine, and D. Ellis, *Intermediate temperature heat pipe life tests and analyses,* in *43rd International Conference on Environmental Systems* (2013) p. 3304.

[12] E. W. Saaski and P. C. Owzarski, *Two-phase working fluids for the temperature range 50 to 350 C,* (1977).

[13] M. Groll, *Heat pipe research and development in western europe,* Heat Recovery Systems and CHP **9**, 19 (1989).

[14] L. Vasil'Ev, G. Volokhov, A. Gigevich, and M. Rabetskii, *Heat pipes based on naphthalene,* Journal of Engineering Physics and Thermophysics **54**, 623 (1988).

[15] L. Grzyll, D. D. Back, C. Ramos, and N. Samad, *Characterization and Testing of Novel Two-Phase Working Fluids for Spacecraft Thermal Management Operating Between 300 Deg. C and 400 Deg. C.*, Tech. Rep. (Mainstream Engineering Corp Rockledge Fl Chemical Systems Div., 1994).

[16] D. Kenney and K. Feldman Jr, *Heat pipe life tests at temperatures up to 400 c,* in *13th Intersociety Energy Conversion Engineering Conference* (1978) pp. 1056–1059.

[17] W. Muenzel, *Compatibility tests of various heat pipe working fluids and structural materials at different temperatures,* in *3rd International Heat Pipe Conference* (1978) p. 398.

[18] O. S. Bruinsma, P. J. Tromp, H. J. de Sauvage Nolting, and J. A. Moulijn, *Gas phase pyrolysis of coal-related aromatic compounds in a coiled tube flow reactor: 2. heterocyclic compounds, their benzo and dibenzo derivatives,* Fuel **67**, 334 (1988).

[19] E. Saaski and J. Hartl, *Two-phase working fluids for the temperature range of 50 to 350 deg, phase 2*, NASA Technical Note CR-159847 (NASA, 1980).

[20] I. Locci, A. Devarakonda, E. Coplan, and J. Olminsky, *Analytical and experimental thermo-chemical compatibility study of potential heat pipe materials,* in *3rd International Energy Conversion Engineering Conference* (2005) p. 5666.

[21] J. E. Deverall, *Mercury as a Heat Pipe Fluid*, Tech. Rep. LA-4300 (Los Alamos Scientific Lab., N. Mex., 1969).

[22] J. Sena and M. Merrigan, *Niobium-1 percent zirconium/potassium life-test heat pipe design and testing,* in *28th Aerospace Sciences Meeting* (1990) p. 63.

[23] J. Rosenfeld, K. Minnerly, C. Dyson, *et al.*, *Ten year operating test results and post-test analysis of a 1/10 segment stirling sodium heat pipe, phase iii,* (2012).

[24] C. Tarau, D. B. Sarraf, D. Beach, I. E. Locci, and W. G. Anderson, *Intermediate temperature fluids life tests-theory,* in *AIP Conference Proceedings*, Vol. 880 (IOP Institute of Physics Publishing Ltd, 2007) p. 137.

[25] T. Daniels and F. Al-Jumaily, *Investigations of the factors affecting the performance of a rotating heat pipe,* International Journal of Heat and Mass Transfer **18**, 961 (1975).

[26] R. A. Perkins, M. Ramires, and C. N. De Castro, *Thermal conductivity of saturated liquid toluene by use of anodized tantalum hot wires at high temperatures,* Journal of research of the National Institute of Standards and Technology **105**, 255 (2000).

[27] M. O. McLinden and J. D. Splett, *A liquid density standard over wide ranges of temperature and pressure based on toluene,* Journal of research of the National Institute of Standards and Technology **113**, 29 (2008).

[28] C. L. Yaws, *Chemical properties handbook* (McGraw-Hill, 1999).

[29] D. Scott, G. Guthrie, J. Messerly, S. Todd, W. Berg, I. Hossenlopp, and J. McCullough, *Toluene: thermodynamic properties, molecular vibrations, and internal rotation,* The Journal of Physical Chemistry **66**, 911 (1962).

[30] A. H. Krall, J. V. Sengers, and J. Kestin, *Viscosity of liquid toluene at temperatures from 25 to 150. degree. c and at pressures up to 30 mpa,* Journal of Chemical and Engineering Data **37**, 349 (1992).

[31] M. V. Roux, M. Temprado, J. S. Chickos, and Y. Nagano, *Critically evaluated thermochemical properties of polycyclic aromatic hydrocarbons,* Journal of Physical and Chemical Reference Data **37**, 1855 (2008).

[32] C. Invernizzi, P. Iora, D. Bonalumi, E. Macchi, R. Roberto, and M. Caldera, *Titanium tetrachloride as novel working fluid for high temperature rankine cycles: Thermodynamic analysis and experimental assessment of the thermal stability,* Applied Thermal Engineering **107**, 21 (2016).

[33] G. Pittinato, *Hydrogen gas generation in water heat pipes,* Journal of Engineering Materials and Technology **100**, 313 (1978).

[34] M. B. H. Mantelli, W. B. Ângelo, and T. Borges, *Performance of naphthalene thermosyphons with non-condensable gases–theoretical study and comparison with data,* International Journal of Heat and Mass Transfer **53**, 3414 (2010).

[35] A. Nuntaphan, J. Tiansuwan, and T. Kiatsiriroat, *Enhancement of heat transport in thermosyphon air preheater at high temperature with binary working fluid: A case study of teg–water,* Applied thermal engineering **22**, 251 (2002).

[36] R. Laubscher and R. T. Dobson, *Theoretical and experimental modelling of a heat pipe heat exchanger for high temperature nuclear reactor technology,* Applied Thermal Engineering **61**, 259 (2013).

[37] H. Jouhara and A. J. Robinson, *An experimental study of small-diameter wickless heat pipes operating in the temperature range 200 c to 450 c,* Heat Transfer Engineering **30**, 1041 (2009).

[38] A. Nuntaphan, J. Tiansuwan, T. Kiatsiriroat, and C. Wang, *Performance improvement of thermosyphon heat exchangers by using two kinds of working fluids,* Heat transfer engineering **22**, 28 (2001).

[39] P. J. Marto, *An analytical and experimental investigation of rotating, non-capillary heat pipes,* (1972), Report no: NASA-CR-130373.

[40] T. Daniels and R. Williams, *Experimental temperature distribution and heat load characteristics of rotating heat pipes,* International Journal of Heat and Mass Transfer **21**, 193 (1978).

[41] R. Ponnappan, J. Leland, and J. Beam, *Comparison of performance results for water and methanol rotating heat pipes,* in *34th Aerospace Sciences Meeting and Exhibit* (1996) p. 477.

[42] R. Ponnappan, Q. He, J. Leland, R. Ponnappan, Q. He, and J. Leland, *Test results of a high speed rotating heat pipe,* in *32nd Thermophysics Conference* (1997) p. 2543.

[43] P. Marto and L. Wagenseil, *Augmenting the condenser heat-transfer performance of rotating heat pipes,* Aiaa Journal **17**, 647 (1979).

[44] R. Marto and H. Weigel, *The development of economical rotating heat pipes,* in *Advances in heat pipe technology* (Elsevier, 1982) pp. 709–724.

[45] L. Vasiliev and V. Khrolenok, *Study of a heat transfer process in the condensation zone of rotating heat pipes,* Journal of heat recovery systems **3**, 281 (1983).

[46] J. S. Lee and C. J. Kim, *Heat transfer and internal flow characteristics of a coil-inserted rotating heat pipe,* International journal of heat and mass transfer **44**, 3543 (2001).

[47] K. Shukla, A. B. Solomon, and B. Pillai, *Experimental studies of rotating heat pipes,* Heat Transfer—Asian Research: Co-sponsored by the Society of Chemical Engineers of Japan and the Heat Transfer Division of ASME **38**, 475 (2009).

[48] A. Solomon, N. Arun, K. Shukla, and B. Pillai, *Steady state perormance of a rotating heat pipe,* in *46th AIAA Aerospace Sciences Meeting and Exhibit* (2008) p. 1293.

[49] M. Kamal, I. Amer, and M. Aboelnasr, *Rotating heat pipe performance with internal wire mesh screens,* Proceedings of the Institution of Mechanical Engineers, Part A: Journal of Power and Energy **224**, 993 (2010).

[50] G. P. Peterson, *An introduction to heat pipes: modeling, testing, and applications,* (1994).

[51] B. Krivosheev, M. Kukharskii, and V. Portnov, *Experimental investigation of heat transfer in a centrifugal heat pipe with an optimized layer of heat-transfer agent,* Journal of engineering physics **43**, 1242 (1982).

[52] M. Semena and Y. A. Khmelev, *Hydrodynamic regimes of a liquid in a smooth-walled rotating heat pipe. 1,* Journal of engineering physics **43**, 1235 (1982).

[53] R. Hashimoto, H. Itani, K. Mizuta, K. Kura, and Y. Takahashi, *Heat transport performance of rotating heat pipes installed in high speed spindle,* Mitsubishi Juko Giho **32**, 366 (1995).

[54] L. Lin and M. Groll, *Critical conditions for collapse of annular flow in a rotating heat pipe with a cylindrical wall,* Heat transfer engineering **17**, 29 (1996).

[55] L. Lin and A. Faghri, *Condensation in rotating stepped wall heat pipes with hysteretic annular flow,* Journal of thermophysics and heat transfer **12**, 94 (1998).

[56] L. Lin and A. Faghri, *Heat transfer analysis of stratified flow in rotating heat pipes with cylindrical and stepped walls,* International journal of heat and mass transfer **40**, 4393 (1997).

[57] L. Lin, T. Xu, and Y. Zhang, *Heat transfer mechanism in a rotating heat pipe with stepped wall, NICT-Mach*, Ph.D. thesis, MSc. Thesis-0033, Nanjing Institute of Chemical Technology (1986).

[58] J. Baker, T. Oliver, L. Lin, R. Ponnappan, and J. E. Leland, *Correlations of critical froude number for annular-rimming flow in rotating heat pipes,* Journal of fluids engineering **123** (2001).

[59] F. Song, D. Ewing, and C. Ching, *Heat transfer in the evaporator section of moderate-speed rotating heat pipes,* International journal of heat and mass transfer **51**, 1542 (2008).

[60] F. Song, D. Ewing, and C. Ching, *Experimental investigation on the heat transfer characteristics of axial rotating heat pipes,* International Journal of Heat and Mass Transfer **47**, 4721 (2004).

[61] Home, Deepayan, *Effect of Working Fluid and Fluid Loading on the Performance of Rotating Heat Pipes,* MSc Thesis, McMaster University, Hamilton, Ontario (2004).

[62] M. Xie, Z. Xue, W. Qu, and W. Li, *Experimental investigation of heat transfer performance of rotating heat pipe,* Procedia Engineering **99**, 746 (2015).

[63] W. Lian and Y. Xuan, *Experimental investigation on a novel aero-engine nose cone anti-icing system,* Applied Thermal Engineering **121**, 1011 (2017).

5

Modelling of the heat pipe assisted annealing line and simulation results

Part of this chapter has been published as:

M. Celik, M. Patki, G. Paulussen, W. de Jong, and B. J. Boersma, *Dynamic Modelling of the Heat Pipe Assisted Annealing Line*, Journal of Heat Transfer, **141**(9), 091801 (2019).

5.1. Introduction

In the previous chapters of this dissertation, various components of the heat pipe assisted annealing concept have been investigated. In Chapter 2, the contact heat transfer between the steel strip and the rotating heat pipe (RHP) has been examined. In Chapter 3, a novel RHP model that enabled fast and yet sufficiently detailed simulation has been developed. Finally in Chapter 4, applicable working fluids for the intermediate and high temperature ranges have been determined and tested. The results from these chapters provide the main tools for building a model of the heat pipe assisted annealing line. This model will help answer the 4th research question of this dissertation:

> *What is the energy efficiency brought by the heat pipe assisted annealing concept for different number of heat pipes and how does the system behave as a whole?*

The model should include the interaction of the strip and the RHPs, the interior dynamics of the RHPs filled with different working fluids, the furnace walls and the overaging section. The model should be transient and should allow for various furnace configurations.

The first part of the current chapter builds upon the previous chapters and develops a model of building blocks describing the heat pipe assisted annealing plant. Following the model development, simulations are performed for a concept heat pipe assisted annealing layout with various heat pipe numbers. With the information gathered from the simulation results, the thermal cycle of the strip and the associated energy recoveries are computed for different line configurations.

5.2. Simulation model

5.2.1. Model description

The heat pipe assisted annealing simulation model comprises of modular components called heat pipe building blocks (HPBB) and strip building blocks (SBB). Each HPBB consists of an RHP and two strips wrapped around the heat pipe placed inside the furnace walls, as shown in Figure 5.1. Each SBB comprises of two strips connecting the neighbouring building blocks. The simulation model essentially represents the interaction between these building blocks. The number of heat pipes in the installation is equal to the number of HPBBs inside the simulation model.

The HPBB comprises of the meshed heat pipe wall, heat pipe interior and strips. The wall of the heat pipe is meshed in axial, radial and angular directions. The strip is meshed only in the angular direction. Each node is a lump mass characterized by a unique thermodynamic status. Each node of the wall also includes thermal resistances on both sides in the axial and radial directions, whereas each node of the strip includes thermal resistances in the radial direction (see Figure 5.2).

The hotter strip is in contact with the evaporator and the colder strip is in contact with the condenser. The adiabatic section is situated between the evaporator and the condenser. Moreover, there are two more adiabatic sections at the two ends of the heat pipe, which are called dead zones. The angular mesh is slightly

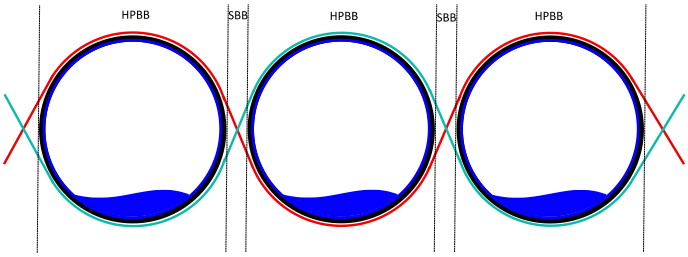

Figure 5.1: Building blocks of the simulation model.

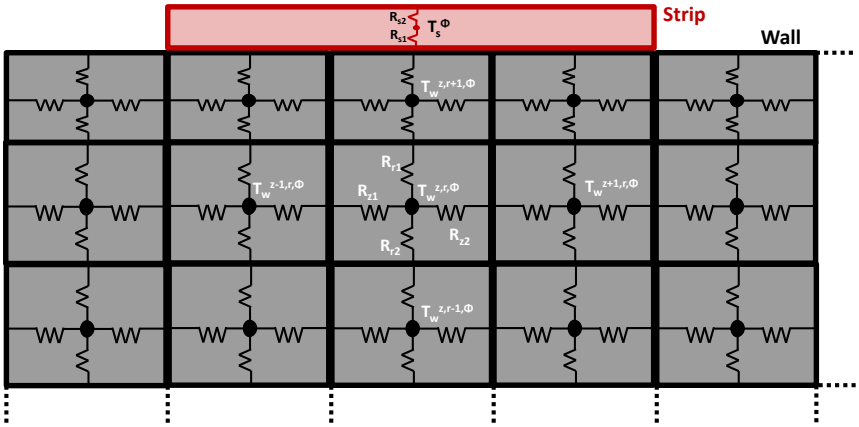

Figure 5.2: Wall and strip nodes in the radial and axial directions.

finer near the first contact point of the strip with the heat pipe in order to better capture the boundary condition change. The mesh structure is mirrored for the other half circumference. The heat pipe wall is divided into several layers in the radial direction. The mesh of the heat pipe wall in the radial direction is finer near the contact with the strip in order to better capture the interaction with the strip (see Figure 5.3).

An interior node of the roll wall is modelled with Eq. 5.1 which is presented in its discretized form in space. The properties are calculated with reference to the average wall temperature for each heat pipe.

$$\rho_w^{z,r,\Phi}\, V_w^{z,r,\Phi}\, c_{p_w}^{z,r,\Phi} \frac{\mathrm{d}T_w^{z,r,\Phi}}{\mathrm{d}t} = \frac{T_w^{z,r+1,\Phi} - T_w^{z,r,\Phi}}{R_{r1}^{z,r+1,\Phi} + R_{r2}^{z,r,\Phi}} + \frac{T_w^{z,r-1,\Phi} - T_w^{z,r,\Phi}}{R_{r2}^{z,r-1,\Phi} + R_{r1}^{z,r,\Phi}} + \frac{T_w^{z+1,r,\Phi} - T_w^{z,r,\Phi}}{R_{z1}^{z+1,r,\Phi} + R_{z2}^{z,r,\Phi}} + \frac{T_w^{z-1,r,\Phi} - T_w^{z,r,\Phi}}{R_{z2}^{z-1,r,\Phi} + R_{z1}^{z,r,\Phi}} + \rho_w^{z,r,\Phi-1}\, d_w^{z,r,\Phi-1}\, w_w^{z,r,\Phi-1}\, u_w^{z,r,\Phi-1}\, h_w^{z,r,\Phi-1} - \rho_w^{z,r,\Phi}\, d_w^{z,r,\Phi}\, w_w^{z,r,\Phi}\, u_w^{z,r,\Phi}\, h_w^{z,r,\Phi} \quad (5.1)$$

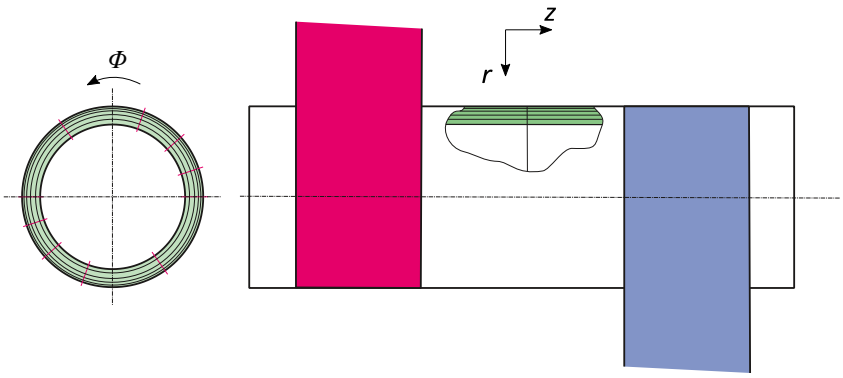

Figure 5.3: HPBB meshing.

Where ρ is the density, V is the volume, c_p is the specific heat capacity, T is the temperature, t is the time, R is the thermal resistance, d is the thickness, w is the width, u is the velocity and h is the specific enthalpy. The superscripts z, r and Φ are indices for the node location in the axial, radial and angular directions respectively and the subscript w represents the wall component. Locations of the thermal resistances are shown in Figure 5.2.

Thermal resistances in the radial and axial directions are found with Eqs. 5.2 and 5.3.

$$R_{radial} = \frac{\ln(r_o/r_i)}{\Delta\Phi\, k\, \Delta z} \tag{5.2}$$

$$R_{axial} = \frac{\Delta z}{k\, A} \tag{5.3}$$

Where r_o and r_i are the outer and inner radii of the given resistance respectively, $\Delta\Phi$ is the angular span of the resistance, k is the thermal conductivity of the component, Δz is the length of the resistance in the axial direction and A is the cross-sectional area of the cell in the axial direction.

The innermost nodes are subjected to the liquid layer temperature, whereas the outermost nodes below the strip are subjected to the strip temperature. For the outermost nodes that are not neighboured by the strip, radiation heat transfer plays a role. For a strip node in the HPBB, Eq. 5.4 applies.

$$\rho_s^{\Phi}\, V_s^{\Phi}\, c_{p_s}^{\Phi} \frac{\mathrm{d}T_s^{\Phi}}{\mathrm{d}t} = \frac{T_w^{z,r_0,\Phi} - T_s^{\Phi}}{R_{r1}^{z,r_0,\Phi} + R_{con}^{\Phi} + R_{s1}^{\Phi}} + \dot{Q}_{rad} + \rho_s^{\Phi-1}\, d_s^{\Phi-1}\, w_s^{\Phi-1}\, u_s^{\Phi-1}\, h_s^{\Phi-1} - \rho_s^{\Phi}\, d_s^{\Phi}\, w_s^{\Phi}\, u_s^{\Phi}\, h_s^{\Phi} \tag{5.4}$$

Where R_{con} is the contact thermal resistance between the strip and the RHP outer wall, $\dot{Q}_{rad}$ is the radiation heat transfer rate, the superscript r_0 represents the node radially located at the outermost layer of the RHP and the subscript s represents the strip.

Contact thermal resistance (R_{con}) is calculated with the simplified expression developed in Section 2.8. The exterior gas properties are calculated based on a typical protective gas composition used commonly in the annealing of steel (5% H_2 / 95% N_2) [1]. It should be noted that the thermal conductivity and the viscosity of the interstitial gas are temperature-dependent and this dependency is accounted for in the calculations. The specific tension applied to the strip at room temperature is taken as 30 MPa. At higher temperatures, a reduction factor describing the change of the actual yield strength with respect to the yield strength at room temperature is applied, as shown in Figure 5.4 [2].

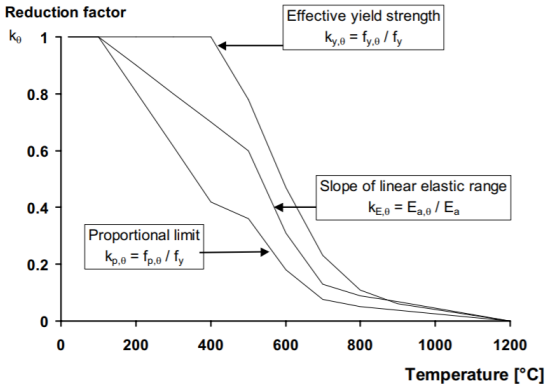

Figure 5.4: Reduction factors for the stress-strain relationship of carbon steel [2].

There are also two end caps to the heat pipe which are modelled as disks with a diameter equal to the heat pipe outer diameter. They are assumed to interact only with the dead zones and thus, are described with the following equation:

$$\rho_w \, V_{ec} \, c_{p_w} \frac{\mathrm{d}T_{ec}}{\mathrm{d}t} = \sum_{r,\Phi} \frac{T_w^{dz1/dz2,r,\Phi} - T_{ec}}{R_{z1/z2}^{dz1/dz2,r,\Phi}} \tag{5.5}$$

Where $dz1$ and $dz2$ represent the dead zones and the subscript ec represents the end cap.

Interior dynamics of the RHP is described with the model derived in Chapter 3, with a number of changes in order to increase the computational speed and to incorporate additional physics. When the flow pattern is not annular (relatively high fill ratio), the thermal resistance caused by the liquid pool and the pulled thin film are calculated with the Eqs. 4.4 to 4.9. Convective terms in the liquid momentum equation are assumed to be negligible due to film layer theory [3–5]. Viscous terms

for liquid and vapor are approximated with friction factors. For laminar flow where Re is lower than 2100, friction factor (f) is taken as $64/\mathrm{Re}$. For turbulent flow, friction factor is calculated as $0.0791/\mathrm{Re}^{0.25}$ [6–8]. This approximation has a negligible effect on the liquid layer distribution and the associated thermal resistance for relatively high fill ratios used in the simulations as also observed in Subsection 3.4.2.

The governing equation for a strip node in the SBB is shown in Eq. 5.6.

$$\rho_s^i \; V_s^i \; c_{p_s}^i \frac{\mathrm{d}T_s^i}{\mathrm{d}t} \;=\; \dot{Q}_{rad} \;+\; \rho_s^{i-1} \; d_s^{i-1} \; w_s^{i-1} \; u_s^{i-1} \; h_s^{i-1} \;-\; \rho_s^i \; d_s^i \; w_s^i \; u_s^i \; h_s^i \tag{5.6}$$

Each building block is always neighboured by side walls and also optionally by bottom, top, front and/or back walls according to the plant layout. Heat losses from the system are through these insulation walls to the surroundings. Furnace walls interact with the building blocks through radiation. The walls are composed of multiple layers with different thermophysical properties and the heat is conducted through these layers. The interaction of the furnace wall with the environment is through natural convection from the outer surface. Due to the solver methodology explained in Subsection 5.2.2, the communication between the building blocks (and associated furnace walls) is only achieved through the traveling strip. This results in more accentuated temperature difference between neighbouring furnace wall elements. Moreover, since the radiation heat transfer should reside in the building block, the receiving surfaces are assumed as semi-infinite during the calculation of view factors.

Furnace wall elements are divided into cells over the thickness as shown in Figure 5.5. The governing equation for each wall cell is shown in Eq. 5.7.

$$\rho_{fw}^i \; V_{fw}^i \; c_{p_{fw}}^i \frac{\mathrm{d}T_{fw}^i}{\mathrm{d}t} = \frac{T_{fw}^{i-1} - T_{fw}^i}{R_{z2}^{i-1} + R_{z1}^i} + \frac{T_{fw}^{i+1} - T_{fw}^i}{R_{z1}^{i+1} + R_{z2}^i} \tag{5.7}$$

Where the subscript fw represents the furnace wall and the superscript i is the index that shows the location of the node. Locations of the thermal resistances are shown in Figure 5.5.

The innermost cells of the furnace wall are subjected to radiation from the building block elements and itself, whereas the outermost cells are subjected to natural convection. Natural convection is associated with the Rayleigh number ($\mathrm{Ra}_{\mathrm{L_c}}$).

$$\mathrm{Ra}_{\mathrm{L_c}} = \frac{g \; \beta \; (T_{sur} - T_\infty) \; L_c^3}{\nu \; \alpha} \tag{5.8}$$

Where $\mathrm{Ra}_{\mathrm{L_c}}$ is the Rayleigh number based on the characteristic length, g is gravity, β is the thermal expansion, T_{sur} is the surface temperature, T_∞ is the ambient temperature, L_c is the characteristic length calculated as the ratio of surface

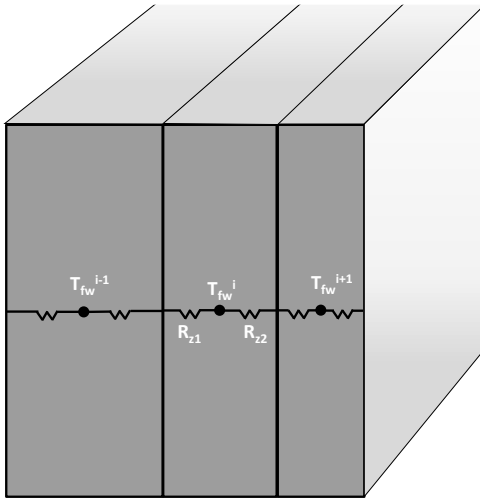

Figure 5.5: Furnace wall cells.

area to perimeter, ν is the kinematic viscosity and α is the thermal diffusivity. All properties are calculated at the film temperature, $T_f = (T_{sur} + T_\infty)/2$.

For a vertical wall surface, Eq. 5.9, for a horizontal wall top surface, Eq. 5.10 and finally for a horizontal wall bottom surface, Eq. 5.11 are used to calculate the average Nusselt number based on the characteristic length ($\overline{\mathrm{Nu}}_{\mathrm{L_c}}$) [9].

$$\overline{\mathrm{Nu}}_{\mathrm{L_c}} = 0.68 + \frac{0.670\ \mathrm{Ra_{L_c}}^{1/4}}{[1 + (0.492\ \mathrm{Pr})^{9/16}]^{4/9}} \tag{5.9}$$

$$\overline{\mathrm{Nu}}_{\mathrm{L_c}} = 0.54\ \mathrm{Ra_{L_c}}^{1/4} \tag{5.10}$$

$$\overline{\mathrm{Nu}}_{\mathrm{L_c}} = 0.52\ \mathrm{Ra_{L_c}}^{1/5} \tag{5.11}$$

Where Pr is the Prandtl number. The average heat transfer coefficient ($\overline{h}$) is related to the average Nusselt number ($\overline{\mathrm{Nu}}_{\mathrm{L_c}}$) with Eq. 5.12.

$$\overline{\mathrm{Nu}}_{\mathrm{L_c}} = \frac{\overline{h}\, L_c}{k} \tag{5.12}$$

View factors follow the rules of unity and reciprocity, as shown in Eqs. 5.13 and 5.14 [9]. Only some of the view factors are calculated and the rest is deduced from these rules.

$$\sum_{j=1}^{N} F_{kj} = 1 \tag{5.13}$$

$$A_j \, F_{jk} = A_k \, F_{kj} \tag{5.14}$$

Where F is the view factor, A is the area, N is the number of surfaces and the subscripts k and j represent different surfaces. Following these rules, view factors are calculated through Eq. 5.15. Curved surfaces are approximated by discretizing the surface to smaller polygons. Integration is performed with the MATLAB function "viewfactor.m" [10].

$$F_{kj} = \frac{1}{A_k} \int_{A_k} \int_{A_j} \frac{\cos\theta_k \cos\theta_j}{\pi S^2} \mathrm{d}A_k \mathrm{d}A_j \tag{5.15}$$

Where S is the distance between the surfaces and θ is the angle between the normal to the surface and the line connecting the surfaces. The net radiation heat transfer to a surface element is modelled with Eq. 5.16 which is valid for diffuse and gray surfaces in a non-participating medium.

$$\dot{Q}_j = \frac{E_{b_j} - J_j}{\frac{1-\varepsilon_j}{\varepsilon_j \, A_j}} \tag{5.16}$$

Where E_b is the blackbody emissive power, J is the radiosity and ε is the emissivity. Radiosity from a surface is calculated with Eq. 5.17.

$$\varepsilon_j \, \sigma \, T_{sur_j}^4 = J_j - (1 - \varepsilon_j)\left(\sum_{k}^{N} F_{jk} \, J_k\right) \tag{5.17}$$

The above equation can be expressed in the form of a matrix multiplication, $\mathcal{P} = \mathcal{W} \, \mathcal{J}$, where the left part of Eq. 5.17 for all surfaces is represented by matrix $\mathcal{P}$ and radiosities are represented by matrix $\mathcal{J}$. The matrix $\mathcal{W}$ is written as follows:

$$\mathcal{W} = \sum_{k}^{N} \left(\delta_{jk} - (1 - \varepsilon_j) \, F_{jk}\right) \tag{5.18}$$

Where δ_{jk} is the Kronecker delta. For each plant layout, the matrix $\mathcal{W}$ is formed once and is used to calculate the radiosities and the radiative heat transfer between elements during the simulation.

Fluid and material properties are obtained from [11–15]. These properties are shown in the Appendix. Thermal expansion of the strip and the heat pipe shell is not

taken into account. Conventional heating and conventional cooling are calculated based on the amount of heat required to reach the target temperatures.

5.2.2. Boundary conditions and system solver

The governing equations describing the building block consist of both first-order ordinary differential equations and algebraic equations. The equations are formulated in their discretized forms in space. Given an initial condition and boundary conditions, the set of equations can be solved with an integration method.

The boundary conditions at the outer furnace wall is a Type-III boundary condition:

$$x = d_{fw} \rightarrow -k\frac{\mathrm{d}T}{\mathrm{d}r} = h_{conv}(T_{\infty} - T_{fw_o}) \tag{5.19}$$

Where x is the coordinate in the direction of the furnace wall thickness, d_{fw} is the furnace wall thickness and T_{fw_o} is the temperature at the outer furnace wall. In the simulations, ambient temperature (T_{∞}) is taken as 25 °C.

The strip temperatures at the furnace entry and soaking section exit are simulated with a Type-I boundary condition:

$$T_{s_{entry}} = T_{\infty} \;\&\; T_{s_{soaking}} = T_{target} \tag{5.20}$$

Where T_{target} is selected as 700 °C in the simulations.

The boundary conditions applied to the interior surfaces of the heat pipe end caps are:

$$z = 0 \;\&\; z = L_{hp} \rightarrow u_l = u_v = 0 \;\&\; \frac{\mathrm{d}T}{\mathrm{d}z} = 0 \tag{5.21}$$

where L_{hp} is the heat pipe length. The boundary condition at the symmetry line of the heat pipes is:

$$r = 0 \rightarrow \frac{\mathrm{d}T}{\mathrm{d}r} = 0 \tag{5.22}$$

The entering strip temperature to the evaporator and the condenser of a certain heat pipe is equal to the exiting strip temperature of the preceding building block. Equations for each building block is solved for a finite time step. After the effects of the time step are calculated for all the building blocks, the resulting strip temperatures entering the building blocks as well as the material properties of each component are updated. The time step is selected as the time it takes for a strip element to travel over the heat pipe. It is defined with Eq. 5.23. This time step can be relaxed as the simulation approaches steady-state.

$$\Delta t = \frac{\min(\kappa)\, r_o}{u_s} \tag{5.23}$$

Where $\min(\kappa)$ is the minimum wrap angle, r_o is the outer radius of the heat pipe and u_s is the strip velocity (line speed).

The initial conditions for each heat pipe are selected such that the heat pipe starts with a uniform temperature throughout and at an idle state. The initial temperatures for the heat pipes increase from the first heat pipe to the last. The problem at hand is stiff. Therefore, the system of equations is solved implicitly with the "MATLAB ode15i" function.

Mesh independence has been tested by systematically varying the number of cells in each direction as well as their sizes near boundary change locations. When doubling the number of cells in all directions caused less than 0.5% variation in the results, the meshing is fixed. The number of cells for each HPBB in total is selected as 294. The heat pipe interior is composed of 20 cells, the heat pipe wall is composed of 5 x 5 x 10 cells in the radial, axial and angular directions, respectively. The strips are composed of 7 cells each in the angular direction and the furnace wall is divided into 10 cells along its thickness. For each SBB, the total number of nodes is 24, with the strips composed of 7 cells each and the furnace wall divided into 10 cells.

5.3. Simulation results

5.3.1. Annealing line configurations

In a typical continuous annealing line, strip enters the line at room temperature. It is then heated up to the target soaking temperature (in this case 700 °C). The line speed in continuous annealing varies with strip thickness. In the current simulations, the product of strip thickness and line speed is kept constant. Some of the heat pipes in the line need to be driven by motors in order to adjust the tension in the line. The heat pipes should be placed as close as possible to each other in order to maximize the wrap angle of the strip.

In the light of this information, the simulations are run for a fixed plant layout determined by Drever International but with varying number of heat pipes. During the plant layout determination, strip steering and strip tension control were taken into account. Important parameters regarding the annealing plant and the simulations are shown in Table 5.1.

The working fluids were determined as water, Dowtherm A, phenanthrene and cesium. Initial simulations showed that water is not applicable because the operating temperature of the first heat pipe in the line is always above 150 °C. Therefore, Dowtherm A, phenanthrene and cesium are used inside the heat pipes. The fill ratio is selected such that there is no annular flow in the organic heat pipes. For cesium heat pipes, the criterion is to have enough liquid regardless of the flow pattern.

Table 5.1: Annealing plant and simulation parameters.

Parameter	Data
Heat pipe length	3 m
Heat pipe outer diameter	0.6 m
Heat pipe wall thickness	22 mm
Heat pipe material	Stainless steel
Strip width	1 m
Strip thickness	0.20 & 0.25 mm
Line speed	7.667 & 6.133 m/s
Target soaking temperature	700 °C
Target overaging temperature	400 °C
Furnace wall thickness	250 mm
Number of heat pipe	45 to 90
Wrap angle	97° to 118° (average of 104°)
Fill ratio	~25% for organic heat pipes ~5% for cesium heat pipes

5.3.2. Near steady-state results

Following the plant and simulation parameters shown in Table 5.1, initially four cases with different number of heat pipes are examined. For all these cases, the strip thickness is 0.25 mm and the line speed is 6.133 m/s. For each case, the simulation is run until near steady-state conditions are achieved.

Figures 5.6 to 5.9 show the strip temperature evolution for all of these cases. Strip temperature changes over different heat pipes and different stages are shown with the following color code: green for Dowtherm A, orange for phenanthrene, red for cesium heat pipes and black for conventional heating/cooling and thermal soaking stages. The abbreviations on the figures are as follows: DP for direct-pass between the heat pipes before and after the overaging stages of the plant during heating, CH for conventional heating, SO for soaking, OA for overaging and CC for conventional cooling.

In these figures, it is seen that each heat pipe contributes to the strip heating and cooling. The close-up of part of the heating cycle in Figure 5.6 shows that the magnitude of these contributions may differ between various heat pipes. It is seen that the heat transfer via cesium heat pipes is significantly larger compared to the heat transfer achieved via heat pipes filled with organic fluids (Dowtherm A and phenanthrene).

The main reason for such difference in the effectiveness of working fluids is the figure of merit of these fluids. The most prominent contributor to the difference between the figure of merit of these working fluids is the liquid thermal conductivity. Still, heat pipes filled with organic fluids are indispensable to the concept in order to cover the intermediate temperature range. A too low temperature, and thus pressure, of a cesium heat pipe is likely to result in high vapor velocities, eventually encountering sonic limitations [16, 17].

Looking at the heating part in Figures 5.6 to 5.9, the strip temperature increase over the first cesium heat pipe is larger than the strip temperature increase over the last cesium heat pipe. This is caused mainly by the increase of the strip specific heat with temperature and the reduction of the strip tension at high temperatures (see Figure 5.4) causing higher thermal contact resistance. To a lesser degree, the increase in the radiation losses also contributes to this behavior. The increase in the strip specific heat has a less obvious consequence on the effectiveness of individual heat pipes. Because the specific heat capacity of the strip is larger at high temperatures, the temperatures of the entering strip to the condenser and the evaporator of a heat pipe operating at a high temperature are closer to each other compared to the temperatures of the entering strips of a heat pipe operating at a lower temperature. This results in less heat to be transferred at higher temperature heat pipes even if the thermal resistances of the heat pipes with the same working fluid are similar. As an example, for the case with 90 heat pipes, the heat transferred with the last cesium heat pipe (~54 kW) is less than the heat transferred with the first cesium heat pipe (~83 kW). For comparison, for the same case, the heat transferred with the last phenanthrene heat pipe is ~34 kW.

The energy recovery of the system is calculated with Eq. 5.24.

$$\eta_e = \frac{h_s^{exit} - h_s^{25°C}}{h_s^{700°C} - h_s^{25°C}} \tag{5.24}$$

Where η_e is the energy efficiency, h_s^{exit} is the specific enthalpy of the exiting strip from the condenser of the last heat pipe, $h_s^{25°C}$ is the specific enthalpy of the entering strip and $h_s^{700°C}$ is the specific enthalpy of the strip at the target temperature.

Consequently, the heat transfer rate via heat pipes is calculated as ~3.9 MW for the first case where the number of heat pipes is 90. This corresponds to an energy recovery of 76.5%. The energy recovery for the simulations run with a total number of 75, 60 and 45 heat pipes are 73.4%, 69.4% and 63.9%, respectively. It is observed that each heat pipe contributes more to the transfer of energy from the cooling stage to the heating stage when the number of heat pipes is lower. This is because the potential that drives the heat transfer for each individual heat pipe (temperature difference between the hot strip and the cold strip on a heat pipe) increases when the number of heat pipes decreases.

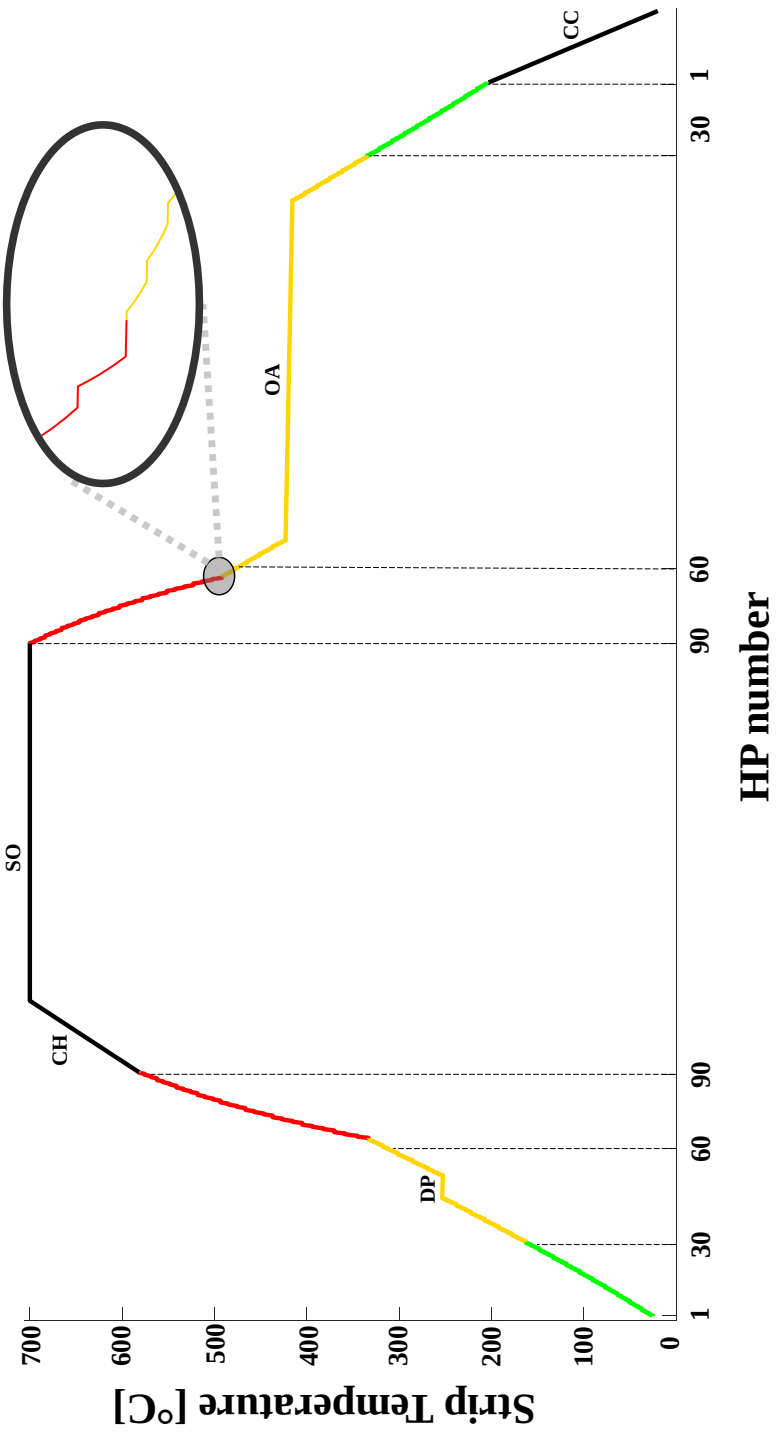

Figure 5.6: Near steady-state result with 90 heat pipes.

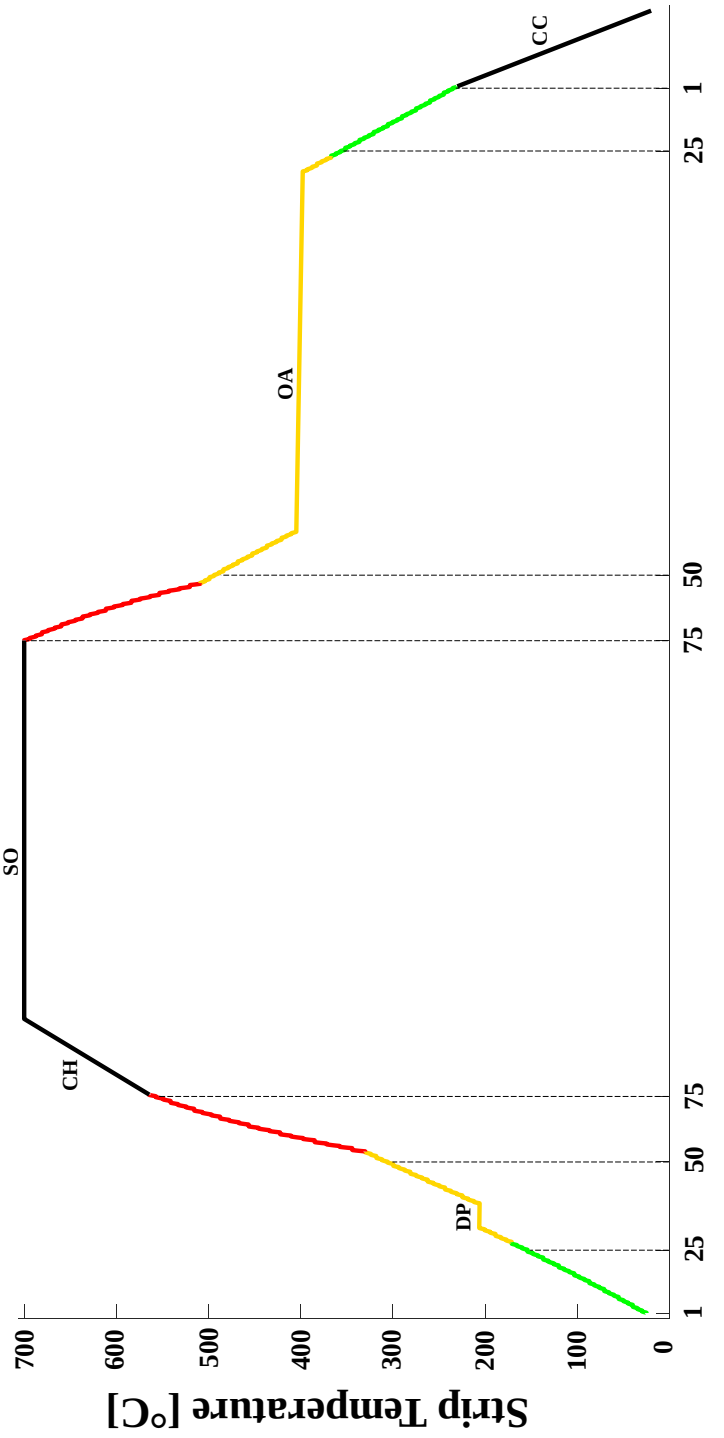

Figure 5.7: Near steady-state result with 75 heat pipes.

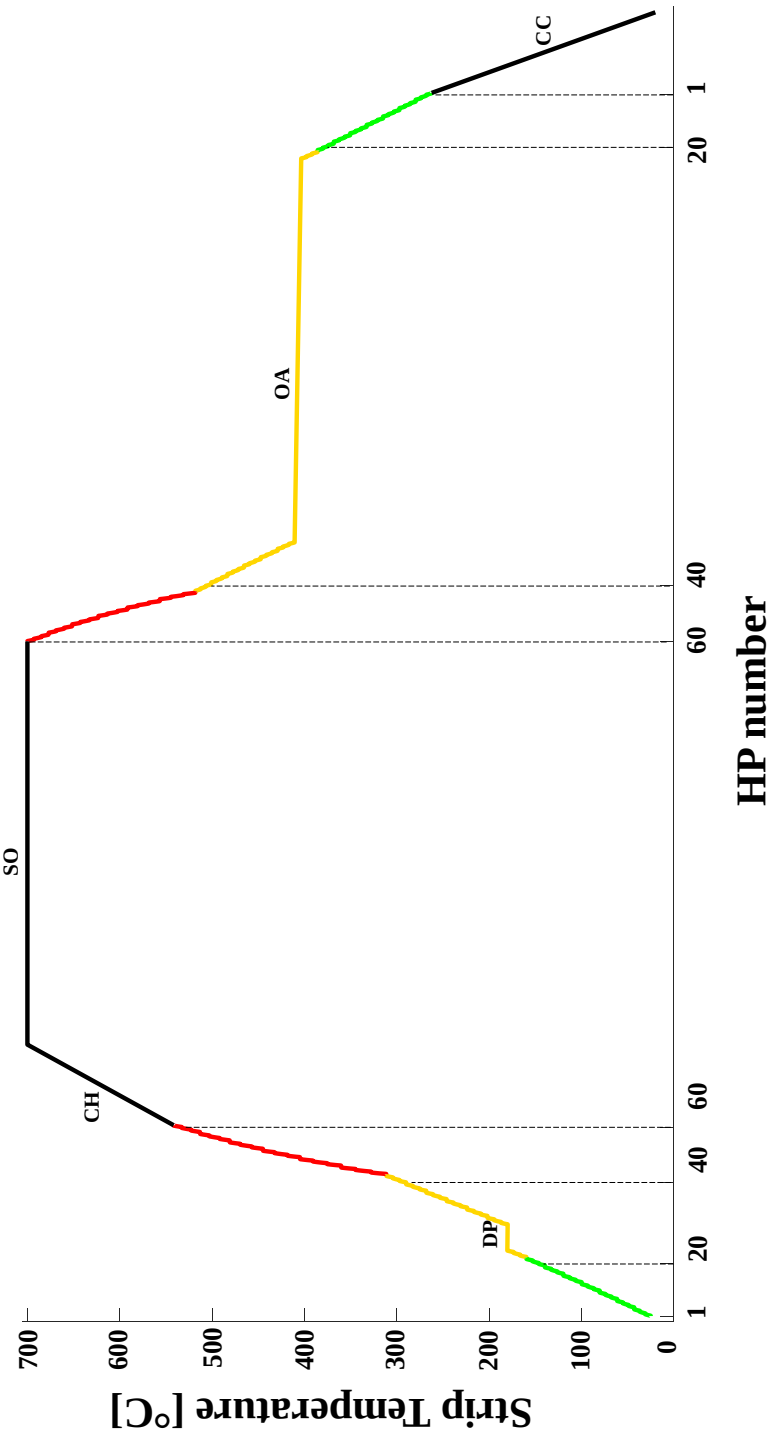

Figure 5.8: Near steady-state result with 60 heat pipes.

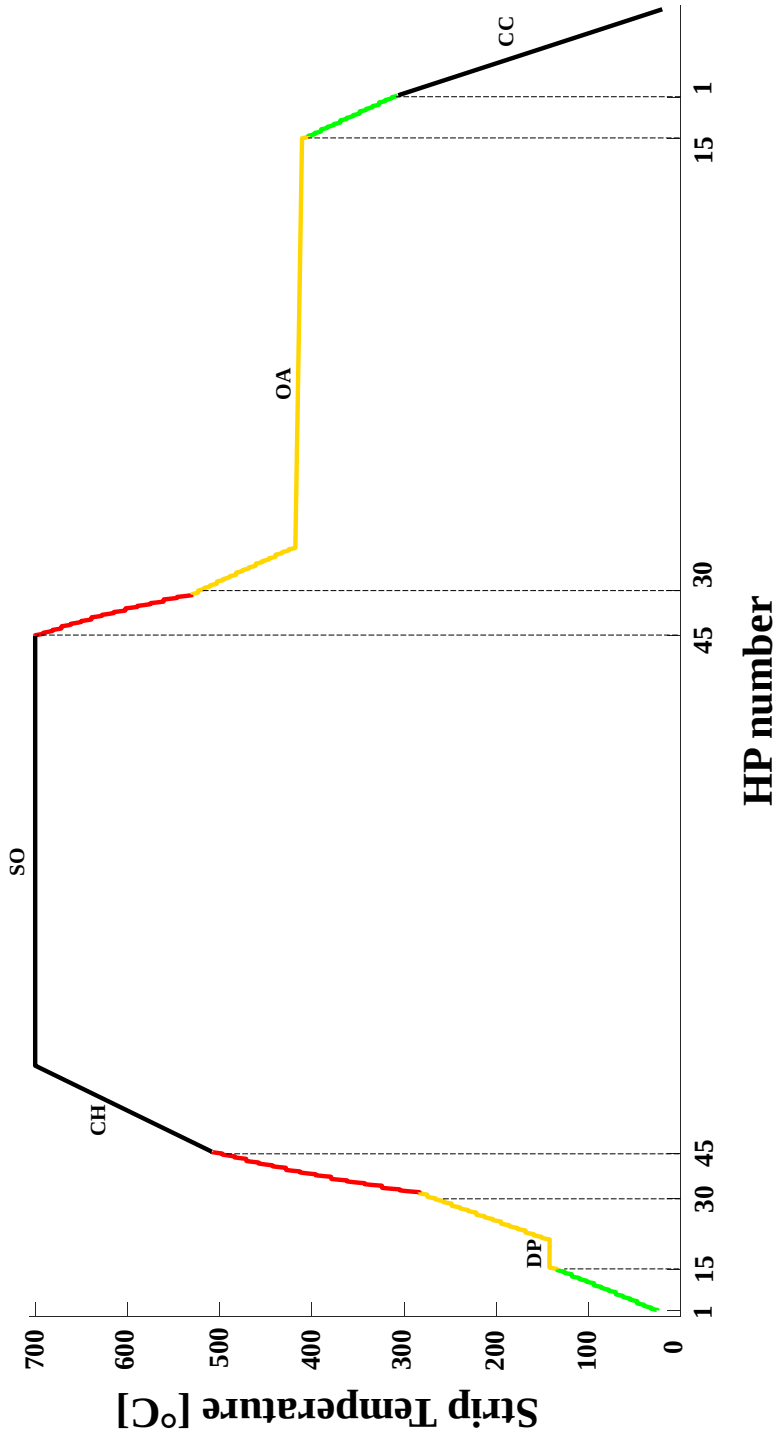

Figure 5.9: Near steady-state result with 45 heat pipes.

Previously considered cases are useful for comparing the effect of varying number of heat pipes in a line. However, it is also likely that strips with different thicknesses will be run in the same plant. When the strip thickness in the line changes, the line speed will be adjusted accordingly to yield the same product of strip thickness and line speed, as mentioned in Subsection 5.3.1. The main effects of changing the line speed and the strip thickness are two-fold in terms of heat transfer. First, contact heat transfer is affected such that a higher line speed and a lower strip thickness results in a higher thermal resistance, as explained in Chapter 2. Second, a higher line speed causes more liquid to be pulled upwards for non-annular flow regimes, increasing the thermal resistance of the liquid layer at the condenser, as elaborated in Chapter 4. On this ground, a simulation with 60 heat pipes, a strip thickness of 0.20 mm and a line speed of 7.667 m/s is run until near steady-state. As expected, the energy recovery decreased to 67.5% compared to the standard case (with 0.25 mm strip thickness and 6.133 m/s line speed) where the energy recovery was 69.4%.

One more simulation is run to estimate the effect of the uncertainty that may be related to the liquid amount pulled upwards for non-annular flow regime. Since this calculation has not been validated in the context of this thesis, the standard case with 60 heat pipes is run with the amount of liquid layer pulled increased by 25%. The result shows that the effect is limited, with the energy recovery decreasing by 1.0% to 68.4%.

All the energy recovery results are summarized in Figure 5.10.

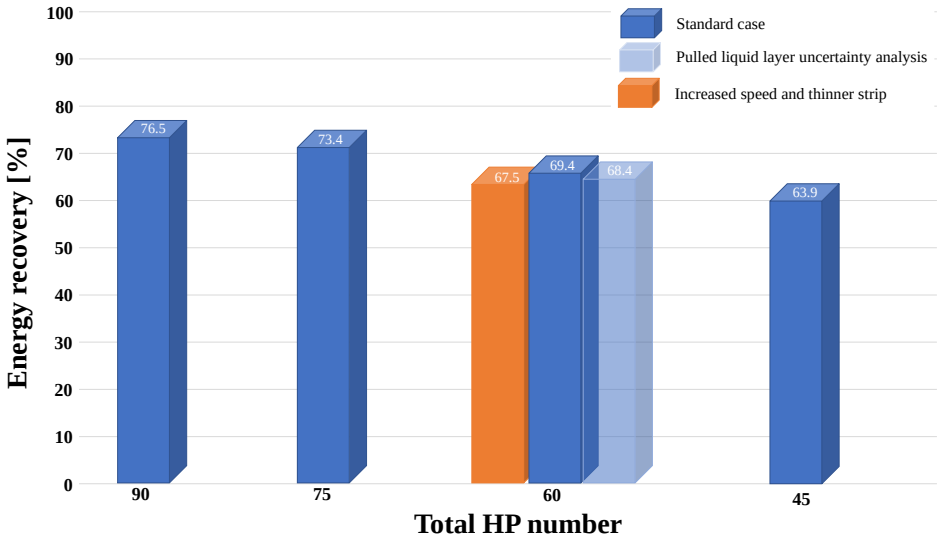

Figure 5.10: Summary of the near steady-state results.

5.3.3. Transient results

With the model, detailed state information such as temperature, pressure, liquid height and vapor velocity in a heat pipe is obtained. In addition, the time-based calculation method allows for time tracking of such parameters.

In Figure 5.11, the temperatures of the first two Dowtherm A heat pipes and the last two cesium heat pipes following a transition to a thinner strip in a plant of 60 heat pipes are shown. It is seen that the temperatures of the cesium heat pipes increase, whereas the temperatures of the Dowtherm A heat pipes decrease, reaching a new near steady-state.

The reason for the decrease in the heat pipe interior temperature can be explained by considering the system as a whole. Looking at the last heat pipe in the line, the entering strip temperature to the evaporator is always equal to the soaking temperature, in this case to 700 °C. However, the entering strip temperature to the condenser increases after the strip thickness decreases. This is because the thinner strip has a lower thermal inertia compared to the thicker strip. Although the contact heat transfer decreases for each strip / heat pipe interaction, in overall this results in a higher strip temperature increase during the heating stage and translates into a lower heat output from the heat pipe after the strip thickness change. Same conditions are true for the other cesium heat pipe.

For the Dowtherm A heat pipes, on the other hand, the exact opposite conditions occur. For the first heat pipe in the line, the entering strip temperature to the condenser is at room temperature before and after the strip transition. The entering strip temperature to the evaporator decreases after the strip transition due to its lower thermal inertia, resulting in the total decrease of the operating temperature.

It is important to note that the thermal cycle requirements of the annealing plant are met at all times during the transition between these near steady-states.

5.4. Conclusions

In this chapter, the energy efficiency and the dynamic behaviour of the heat pipe assisted annealing system are investigated. In order to achieve this objective, the dynamic model of the system is developed. The model is composed of a series of building blocks. A heat pipe building block (HPBB) consists of a rotating heat pipe, steel strips hemicylindrically wrapped around it and furnace walls. A strip building block (SBB) includes strips connecting HPBBs and furnace walls. The contact heat transfer and the RHP models are adapted from Chapters 2, 3 and 4.

The described model is used as a process model to simulate the behavior of the system. Additionally, it is used as an engineering support model to optimize the installation configuration with respect to the number of heat pipes and the locations of the heat pipes in the plant. The simulations are run for a fixed plant layout, with varying number of heat pipes. The average wrap angle in the considered design was 104°.

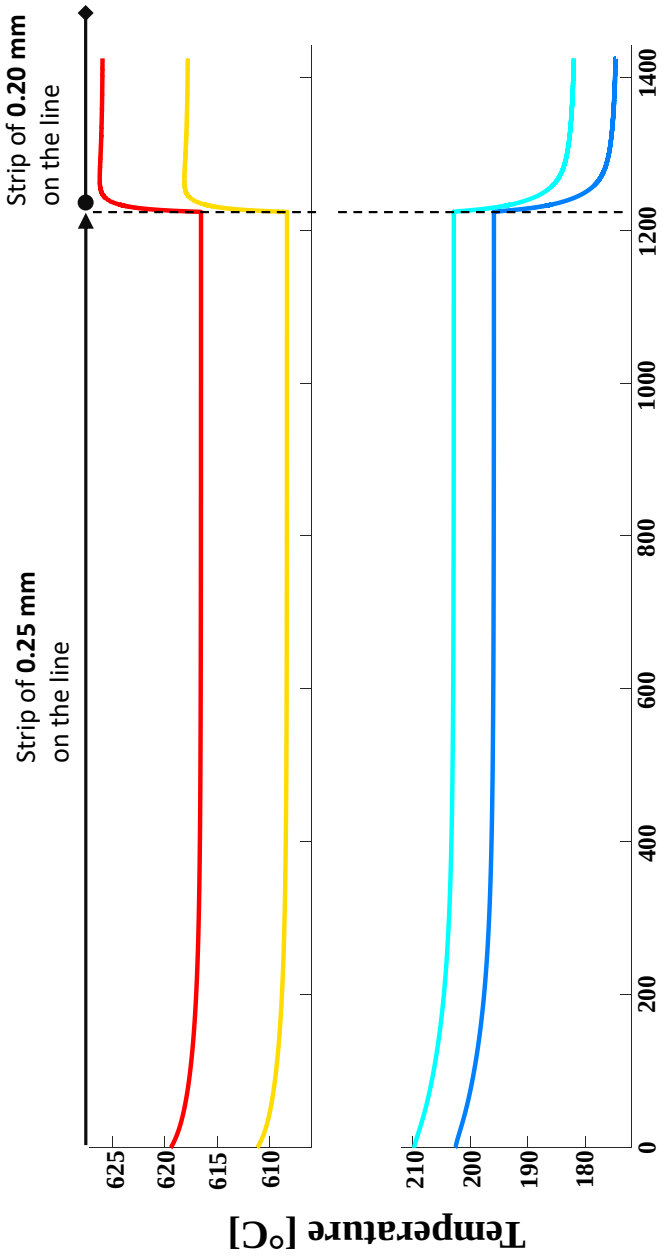

Figure 5.11: Transient behaviour of the system following a strip change in the line.

The simulation results show that the thermal cycle requirements can be satisfied with this new technology. The efficiency of the liquid metal heat pipes is much higher compared to the organic heat pipes. However, the organic heat pipes are indispensable to the concept as they are instrumental in covering the intermediate temperature range during annealing. The energy recoveries for the simulations run for a strip of 0.25 mm and a line speed of 6.133 m/s with a total number of 90, 75, 60 and 45 heat pipes are 76.5%, 73.4%, 69.4% and 63.9%, respectively. Even though the product of line speed and strip thickness is kept constant, a faster and thinner strip in the line results in the decrease of energy transfer through heat pipes. This is mainly caused by the deterioration of the contact heat transfer between the strip and the heat pipe.

References

[1] H. Chandler, *Heat treater's guide: practices and procedures for irons and steels* (ASM international, 1994).

[2] E. Eurocode, *3: Design of steel structures: Part 1.2, general rules–structural fire design,* Brussels: European Committee for Standardization. DD ENV **1** (1993).

[3] R. Bertossi, N. Guilhem, V. Ayel, C. Romestant, and Y. Bertin, *Modeling of heat and mass transfer in the liquid film of rotating heat pipes,* International Journal of Thermal Sciences **52**, 40 (2012).

[4] F. Song, D. Ewing, and C. Ching, *Fluid flow and heat transfer model for high-speed rotating heat pipes,* International Journal of Heat and Mass Transfer **46**, 4393 (2003).

[5] C. Harley and A. Faghri, *Two-dimensional rotating heat pipe analysis,* Journal of Heat Transfer **117**, 202 (1995).

[6] R. McGlen, P. Kew, and D. Reay, *Heat pipes: theory, design and applications* (Elsevier, 2006).

[7] C. Ferrandi, F. Iorizzo, M. Mameli, S. Zinna, and M. Marengo, *Lumped parameter model of sintered heat pipe: Transient numerical analysis and validation,* Applied Thermal Engineering **50**, 1280 (2013).

[8] Y. Cao and A. Faghri, *Transient multidimensional analysis of nonconventional heat pipes with uniform and nonuniform heat distributions,* Journal of Heat Transfer **113**, 995 (1991).

[9] T. L. Bergman, F. P. Incropera, D. P. DeWitt, and A. S. Lavine, *Fundamentals of heat and mass transfer* (John Wiley & Sons, 2011).

[10] . Developped by Nicolas Lauzier with collaboration of Daniel Rousse, Université Laval, *Matlab viewfactor.m,* https://nl.mathworks.com/matlabcentral/fileexchange/5664-view-factors?s_tid=FX_rc1_behav, accessed: 2019-03-01.

[11] C. L. Yaws, *Chemical properties handbook* (McGraw-Hill, 1999).

[12] D. C. Company, *Dowtherm, a. heat transfer fluid – product technical data,* http://msdssearch.dow.com/PublishedLiteratureDOWCOM/dh_0030/0901b803800303cd.pdf, accessed: 2019-03-01.

[13] P. J. Linstrom and W. G. Mallard, *The nist chemistry webbook: A chemical data resource on the internet,* Journal of Chemical & Engineering Data **46**, 1059 (2001).

[14] M. Ghatee and M. Sanchooli, *Viscosity and thermal conductivity of cesium vapor at high temperatures,* Fluid phase equilibria **214**, 197 (2003).

[15] P. Colonna and T. Van der Stelt, *Fluidprop: a program for the estimation of thermo physical properties of fluids,* Energy Technology Section, Delft University of Technology, Delft, The Netherlands, http://www. FluidProp. com (2004).

[16] C. Busse, *Theory of the ultimate heat transfer limit of cylindrical heat pipes,* International Journal of Heat and Mass Transfer **16**, 169 (1973).

[17] P. Nemec, A. Čaja, and M. Malcho, *Mathematical model for heat transfer limitations of heat pipe,* Mathematical and Computer Modelling **57**, 126 (2013).

6

Conclusions and Recommendations

6.1. Conclusions

In this thesis, the fundamentals and the feasibility of the heat pipe assisted annealing concept are studied through a thermal engineering perspective. To perform this study, the gaps in the required knowledge are identified and are expressed in the form of four research questions. Each research question is addressed in a separate chapter of this thesis. These research questions and the key aspects of the answers to the research questions are summarized below.

In Chapter 2 of this thesis, answers are sought to the question: "What are the underlying physics governing the heat transfer between a moving steel strip and a rotating heat pipe and how can this be quantified?". When a strip runs over a moving roll, gas from the surroundings is dragged and compressed in between the strip and the roll. When the roll is large enough, this gas layer converges into a uniform thickness and forms a thermal resistance between the strip and the roll. In this case, the heat transfer between the strip and the roll becomes a function of the gas layer thickness, gas properties, solid-to-solid contact between the surfaces and surface temperatures. In order to determine these properties, Reynolds lubrication equation and the force balance for a stiff strip are solved simultaneously. The solution for gas layer and contact pressure is then coupled with the contact heat transfer model based on the conduction through the gas layer, conduction through the solid contact and radiation. The developed model is validated with experiments executed with a test rig that consists of an RHP and steel strips hemicylindrically wrapped around it. The thermal resistance between the strip and the RHP is deduced for various conditions from the temperature evolution of the strip measured with an IR camera.

The numerical model based on first principles showed good agreement with the experimental results. For the considered cases, it is shown that the uniform region forms around 99% of the total contact area and conduction through the gas layer is responsible for almost all of the heat transferred. The contact heat transfer coefficient in the uniform region varied between 4,000 to 20,000 W/(m^2.K). The contact heat transfer coefficient shows an increase with decreasing strip velocity due to less gas being dragged and it shows an increase with increasing radial stress following the force balance of the strip. Moreover, the effect of different gas properties on the heat transfer coefficient is studied. The increase in the viscosity of the gas causes more entrainment and thus a larger thermal resistance, whereas the increase in the thermal conductivity of the gas naturally reduces the thermal resistance.

For the faster calculation of the contact heat transfer in the dynamic modelling of the heat pipe assisted annealing plant, a simplified expression is obtained through multiple regression analysis. Two synthetic variables, namely the foil bearing number and the compressibility number, are created and used to generate this expression. The expression is applicable when conduction dominates the heat transfer, side leakage is negligible and the uniform region forms most of the heat transfer area.

In Chapter 3, the research question: "How can one develop a transient rotating heat pipe model which provides sufficient details about its interior dynamics without experiencing long computational times?" is investigated. The transient modelling of

cylindrical RHPs has been extensively studied in the published literature. However, these models are all based on detailed CFD models, providing a lot of detail about the functioning and the state of an RHP at the expense of a high computational cost. This computational cost is considered to be mainly caused by the tracking of the liquid / vapor interface. Nonetheless, the liquid / vapor interface should be tracked to describe the interior dynamics of an RHP. This is especially important for calculating the thermal resistances caused by the liquid layer and for understanding the limits of dryout at the evaporator. In this regard, a model describing the dynamics of the RHP is developed. The novelty of this model lies in sufficiently describing the interior dynamics of the heat pipe with a much lower computational cost. In this way, the developed model can be used in the dynamic modelling of the heat pipe assisted annealing plant where ~100 heat pipes connected to each other with strip are modelled. The developed model is applicable to cylindrical capillary-driven heat pipes (CDHPs) as well, with small variations in the equations.

The model assumes an axisymmetric geometry and a one dimensional vapor and liquid flow. Moreover, the dynamics of the vapor is considered to be much faster compared to the heat pipe wall and the liquid. At each axial location of the heat pipe, only one cell for each component (wall, liquid and vapor) is formed. To inexpensively track the interface, the liquid and the vapor cells are allowed to change size radially. This enables tracking without the need for fine meshing or re-meshing. Based on this geometry and meshing, the equations for mass, momentum and energy are solved implicitly.

The model is validated for both RHP and CDHP, showing an excellent agreement with other experimental, analytical and numerical studies. The deviation is calculated as around 2% with the numerical and analytical studies and around 6% with the experimental study. The accuracy is observed to worsen with a low number of computational cells especially when the fill ratio is very low, the heat flux is high and the heat pipe is long. Computational time and relative error in the heat transferred through the heat pipe is calculated for different mesh sizes. It is seen that a doubling in the mesh size triples the computational time. The effect of operating temperature on vapor dynamics is studied with the model. It is demonstrated that the vapor velocity increases with a decrease in the operating temperature due to lower vapor density. It is also shown that the same amount of liquid can be transported in an RHP with a lower liquid head when the rotational speed is higher.

In Chapter 4, the research question ”What are the applicable working fluids for the high temperature range (150 °C to 700 °C) of the heat pipe assisted annealing concept?” is examined. In order to answer this question, initially a comprehensive literature review is made. After the preliminary selection, a life time test is carried out for one of the selected working fluids (phenanthrene). Finally at the last part of this chapter, experiments are performed with an RHP setup at a relatively high temperature with another selected working fluid (Dowtherm A).

The literature review systematically considered various criteria, namely vapor pressure, life time, figure of merit and safety. With these criteria, a preliminary selection of working fluids covering the region from the ambient temperature to 700 °C is made. This selection yielded water, Dowtherm A, phenanthrene and cesium

as potential working fluids. Potassium can be considered as a cheaper alternative to cesium. As an alternative to organics, on the other hand, halides can be used in combination with a suitable heat pipe material or with a thin coating.

Phenanthrene has not been tested so far as a working fluid in a heat pipe. However, it has been reported to be very stable. To test its stability, a life time test is designed and performed. The objective of this test is to determine whether phenanthrene is adequately stable in long-term for the maximum intended temperature which is 450 °C. In this regard, the performances of thermosyphons filled with phenanthrene before and after they are subjected to a thermal load are measured. The duration of the test is determined as 3 months. The deterioration of performance after 3 months would signal the thermal decomposition of the organic working fluid. Some of the thermosyphons were also filled with Dowtherm A and introduced to the test as a control, since Dowtherm A is expected to deteriorate at these conditions. The test results showed a significant deterioration in the performance of all thermosyphons. However, the deterioration could have been facilitated by the presence of air inside the thermosyphons.

Another working fluid that has been selected, Dowtherm A, is tested in an RHP setup. The tests are performed at a temperature range between 150 °C and 350 °C and with a rotational speed up to 1090 RPM. The results show that Dowtherm A can be used as a thermal energy carrier in an RHP. Although it has a very low figure of merit mainly due to its low thermal conductivity, the non-annular flow regime can be beneficial in increasing the efficiency of the RHP. The thermal resistance at the evaporator and the condenser of the RHP at different rotational speeds is compared to the theoretical estimations. The predictions at the evaporator yielded completely different results, most probably due to the eccentricity of the heat pipe occurred during its manufacture. The agreement was better at the condenser.

In Chapter 5 of this thesis, the knowledge gathered from the previous chapters is used to address the following question: "What is the energy efficiency brought by the heat pipe assisted annealing concept for different number of heat pipes and how does the system behave as a whole?". In this context, the dynamic simulation of the heat pipe assisted annealing line is performed. The dynamic simulation consists of the interaction of two types of computational building blocks. The heat pipe building block (HPBB) is composed of a rotating heat pipe, steel strips hemicylindrically wrapped around it and furnace walls. The strip building block (SBB), on the other hand, consists of strips connecting HPBBs and furnace walls.

The simulations are run for a fixed plant layout with different number of heat pipes and operational settings. With a strip of 0.25 mm and a line speed of 6.133 m/s, the energy recoveries are found to be 76.5%, 73.4%, 69.4% and 63.9% for a total heat pipe number of 90, 75, 60 and 45, respectively. When the strip thickness is decreased to 0.20 mm and the line speed is increased to 7.667 m/s (keeping the product of strip thickness and line speed constant compared to previous cases), the resulting energy recovery was lower. For the case of 60 heat pipes, the energy recovery reduced to 67.5% compared to 69.4% with the thicker strip. The main reason for this decrease is the deterioration of the contact heat transfer due to lower radial stress and higher line speed.

The dynamic model is also used to gather information during changes in the operational conditions. It has been shown that a decrease in the thickness of the strip on the line results in the spreading of the operating temperatures of the heat pipe. It is seen that the thermal cycle requirements of the annealing plant are met at all times during the transitions.

6.2. Recommendations

The contact heat transfer study addressed in Chapter 2 can be extended in several ways for future work. In case it is later necessary in the context of the heat pipe assisted annealing project or in other studies, improvement opportunities for the contact heat transfer can be considered and examined in detail. Examples to these improvements can be the addition of grooves to the roll surface and extra auxiliary rolls to the entry and exit of the heat pipe. Different simplified expressions can be created for different geometries (e.g. with grooves) and for cases where solid-to-solid heat transfer also plays a large role. For the experimental part of this work, an additional measurement for the roll surface temperature or for the heat flux through the heat pipe shell would provide more accurate estimates.

As for the future work regarding the model developed in Chapter 3, the model can also be adapted to stepped and tapered RHPs. Especially stepped RHPs can be relevant to the heat pipe assisted annealing concept, where the efficiency of the RHPs can be increased with relatively low cost. It should be noted that the application of the model to both stepped and tapered RHPs would require a finer meshing at the condenser because the liquid layer thickness at the condenser would be lower for such heat pipes. Details of the model can be increased or decreased at the expense of a higher computational cost or at the benefit of a lower one, based on the selected application. Moreover, a model including the physics governing the non-condensable gases can be coupled to the developed engineering model.

There is a lot of room for improvement regarding Chapter 4 of this thesis. First of all, the life time tests need to be performed again with better vacuumed and sealed thermosyphons. The tests should be carried out at different temperature levels, both for phenanthrene and Dowtherm A. These tests can be extended to halides and alkali metals in the future. For the RHP tests, it is clear that eccentricity played a large role in the results. A new RHP should be integrated to the setup for a better analysis. Moreover, the performance increase with a stepped-wall RHP can be investigated. An acrylic heat pipe can be produced to visually study the flow pattern inside the heat pipe at different rotational speeds and fluid properties. Additionally, phenanthrene, cesium and potassium can be tested in RHPs provided that better vacuum is achieved.

The model developed in Chapter 5 can be used for other plant layouts (e.g. even lower number of heat pipes, using intermediate heaters, etc.), different heat pipe designs (e.g. stepped heat pipes, different working fluids, etc.) and other operating conditions (e.g. different soaking temperatures). Future work can also be based on the improvements of models and findings from Chapters 2, 3 and 4 based on the recommendations which can be integrated to the dynamic model of the heat pipe assisted annealing line.

Appendix

Appendix A - Infrared camera calibration

In Chapter 2 of this dissertation, an infrared camera has been used to record the temperature of the strip running over the heat pipe. To achieve this, digital level readings from the infrared camera ($\mathcal{L}$) are converted to temperature readings (T) with the help of Wien's approximation of Planck's law for short wavelengths as shown below.

$$\mathcal{L} = \Lambda e^{-\frac{h\,c}{k_b\,\lambda\,T}} \tag{A.1}$$

Where Λ is the camera factor which incorporates system-dependent factors, h is Planck's constant, c is the light speed, k_b is Boltzmann's constant and λ is the wavelength captured by the camera.

Eq. A.1 can be rewritten in the following form to establish a linear relationship between $1/T$ and $\ln \mathcal{L}$.

$$\frac{1}{T} = -\frac{\lambda\,k_b}{h\,c}\ln \mathcal{L} + \frac{\lambda\,k_b}{h\,c}\ln \Lambda \tag{A.2}$$

Digital level readings from the infrared camera are matched to temperatures readings of a contact thermocouple used when the setup is at a high temperature and at rest. $1/T$ is plotted against $\ln \mathcal{L}$ for various temperatures and the relationship is modelled with linear regression. The camera factor Λ and the wavelength λ are deduced from the linear regression with the help of Eq. A.2. Same procedure is applied to different positions and strips.

Appendix B - Derivation of the heat pipe model equations

In Chapter 3 of this dissertation, the equations describing the dynamics of the heat pipe interior are written in their discretized forms in space. Below, the integrations for two equations (continuity equation and energy equation for liquid layer in RHP) are given to serve as exemplary procedures.

The continuity equation for an infinitesimally small geometry in cylindrical coordinate can be written as in Eq. B.1

$$\frac{\partial(\rho\,\mathrm{d}V)}{\partial t}+\frac{\partial(\rho\,r\,u_r)}{\partial r}\mathrm{d}r\,\mathrm{d}\Phi\,\mathrm{d}z+\frac{\partial(\rho\,u_\Phi)}{\partial \Phi}\mathrm{d}\Phi\,\mathrm{d}r\,\mathrm{d}z + \frac{\partial(\rho\,u_z)}{\partial z}\mathrm{d}z\,r\,\mathrm{d}\Phi\,\mathrm{d}r=0 \quad \text{(B.1)}$$

Where $\mathrm{d}V$ is defined as:

$$\mathrm{d}V=\mathrm{d}z\,r\,\mathrm{d}\Phi\,\mathrm{d}r \quad \text{(B.2)}$$

Integration is performed over the control volume for an annular liquid layer with a volume of $\pi(r_i^2-(r_i-d_l)^2)\Delta z$.

Integration of term 1: $\frac{\partial(\rho\,\mathrm{d}V)}{\partial t}$

$$\int_{r_i-d_l}^{r_i}\int_0^{2\pi}\int_z^{\Delta z}\frac{\partial(\rho\,\mathrm{d}z\,r\,\mathrm{d}\Phi\,\mathrm{d}r)}{\partial t}=\frac{\partial(\rho\,\Delta z\,\pi\,(r_i^2-(r_i-d_l)^2))}{\partial t} \quad \text{(B.3)}$$

Where $\Delta z\,\pi\,(r_i^2-(r_i-d_l)^2)$ is the volume of the node.

Integration of term 2: $\frac{\partial(\rho\,r\,u_r)}{\partial r}\mathrm{d}r\,\mathrm{d}\Phi\,\mathrm{d}z$

$$\int_{r_i-d_l}^{r_i}\int_0^{2\pi}\int_z^{\Delta z}\frac{\partial(\rho\,r\,u_r)}{\partial r}\mathrm{d}r\,\mathrm{d}\Phi\,\mathrm{d}z = 2\pi\,\Delta z\,r_i\,\rho\,u_r\big|_{r_i}-2\pi\,\Delta z\,(r_i-d_l)\,\rho\,u_r\big|_{r_i-d_l} \quad \text{(B.4)}$$

Where the mass crossing the heat pipe wall at $r=r_i$ is 0 and the mass crossing the interface located at $r=r_i-d_l$ is $\dot{m}_{ph}$.

Integration of term 3: $\frac{\partial(\rho\,u_\Phi)}{\partial \Phi}\mathrm{d}\Phi\,\mathrm{d}r\,\mathrm{d}z$

Due to axisymmetry:

$$\int_{r_i-d_l}^{r_i}\int_{0}^{2\pi}\int_{z}^{\Delta z}\frac{\partial(\rho\, u_\Phi)}{\partial\Phi}\mathrm{d}\Phi\,\mathrm{d}r\,\mathrm{d}z = 0 \tag{B.5}$$

Integration of term 4: $\dfrac{\partial(\rho\, u_z)}{\partial z}\mathrm{d}z\, r\, \mathrm{d}\Phi\, \mathrm{d}r$

$$\int_{r_i-d_l}^{r_i}\int_{0}^{2\pi}\int_{z}^{\Delta z}\frac{\partial(\rho\, u_z)}{\partial z}\mathrm{d}z\, r\, \mathrm{d}\Phi\, \mathrm{d}r = \pi\,\rho\, u_z\left(r_i^2-(r_i-d_l)^2\right)\Big|_{z+\Delta z} - \pi\,\rho\, u_z\left(r_i^2-(r_i-d_l)^2\right)\Big|_{z} \tag{B.6}$$

Assigning the index $i-0.5$ to the location corresponding to $z=z$ and $i+0.5$ to the location corresponding to $z=z+\Delta z$, describing u_z as u_l and defining A_l as in Eq. 3.7 and finally adding all integrated terms together yields:

$$\frac{\mathrm{d}\left(\rho_l^i\, V_l^i\right)}{\mathrm{d}t} = \rho_l^{i-0.5} A_l^{i-0.5} u_l^{i-0.5} - \rho_l^{i+0.5} A_l^{i+0.5} u_l^{i+0.5} - \dot{m}_{ph}^i \tag{B.7}$$

The energy equation for an infinitesimally small geometry in cylindrical coordinates can be written as in Eq. B.8 when the angular direction is neglected due to axisymmetry and the source term is described as the heat flow in the radial direction.

$$\frac{\partial(\rho\, h\, \mathrm{d}V)}{\partial t} + \frac{\partial(\rho\, u_z\, h\, \mathrm{d}V)}{\partial z} + \frac{\partial(\rho\, u_r\, h\, \mathrm{d}V)}{\partial r} = -\frac{\partial \dot{q}_r}{\partial r}\mathrm{d}r \tag{B.8}$$

Where $\mathrm{d}V$ is defined as in Eq. B.2 and h is the specific enthalpy. As in the continuity equation, integration is performed over the control volume for an annular liquid layer with a volume of $\pi(r_i^2-(r_i-d_l)^2)\Delta z$.

Integration of term 1: $\dfrac{\partial(\rho\, h\, \mathrm{d}V)}{\partial t}$

$$\frac{\partial(\rho\, h\, \mathrm{d}V)}{\partial t} = \rho\, \mathrm{d}V\, \frac{\partial h}{\partial t} + h\, \frac{\partial(\rho\, \mathrm{d}V)}{\partial t}$$

$$\Rightarrow \int_{r_i-d_l}^{r_i}\int_{0}^{2\pi}\int_{z}^{\Delta z}\rho\, \mathrm{d}V\, \frac{\partial h}{\partial t} + \int_{r_i-d_l}^{r_i}\int_{0}^{2\pi}\int_{z}^{\Delta z} h\, \frac{\partial(\rho\, \mathrm{d}V)}{\partial t}$$

$$= \rho\, V\, \frac{\partial h}{\partial t} + h\left(\dot{m}_{in} - \dot{m}_{out} - \dot{m}_{ph}\right) \tag{B.9}$$

Integration of term 2: $\frac{\partial(\rho\, u_z\, h\, \mathrm{d}V)}{\partial z}$

$$\int_{r_i-d_l}^{r_i}\int_0^{2\pi}\int_z^{\Delta z}\frac{\partial(\rho\, u_z\, h\, \mathrm{d}V)}{\partial z} = \rho\,\pi\left(r_i^2-(r_i-d_l)^2\right)u_z\,h\,\big|_{z+\Delta z} - \rho\,\pi\left(r_i^2-(r_i-d_l)^2\right)u_z\,h\big|_z = \dot{m}_{in}\,h_{in} - \dot{m}_{out}\,h_{out} \quad \text{(B.10)}$$

Integration of term 3: $\frac{\partial(\rho\, u_r\, h\, \mathrm{d}V)}{\partial r}$

$$\int_{r_i-d_l}^{r_i}\int_0^{2\pi}\int_z^{\Delta z}\frac{\partial(\rho\, u_r\, h\, \mathrm{d}V)}{\partial r} = \rho\,\Delta z\,2\pi\,r_i\,u_r\,h\big|_{r_i} - \rho\,\Delta z\,2\pi\,(r_i-d_l)\,u_r\,h\big|_{r_i-d_l} = 0 - \dot{m}_{ph}\,h_{out} \quad \text{(B.11)}$$

Integration of term 4: $-\frac{\partial \dot{q}_r}{\partial r}\mathrm{d}r$

Taylor series expansion dictates $-\frac{\partial \dot{q}_r}{\partial r}\mathrm{d}r = \dot{q}_r - \dot{q}_{r+\mathrm{d}r}$

First, the heat flow from the wall to the liquid (or vice versa) is calculated.

$$-\dot{q}_{r+\mathrm{d}r} = k\frac{\mathrm{d}T}{\mathrm{d}r}\,r\,\mathrm{d}\Phi\,\mathrm{d}z \quad \text{(B.12)}$$

Rearranging and integrating in between the nodes (including the interface between the wall and the liquid nodes):

$$\int_{r_i-d_l/2}^{r_i+-d_l/2}\int_0^{2\pi}\int_z^{\Delta z}\frac{\dot{q}_{r+dr}}{k\,r\,\mathrm{d}\Phi\,\mathrm{d}z}\mathrm{d}r = \int_{T_l}^{T_w}\mathrm{d}T \quad \text{(B.13)}$$

As the thermal conductivity changes from one material to the other, the integral is performed in two steps, from $r_i + d_l/2$ to r_i and then from r_i to $r_i - d_l/2$.

$$\dot{q}_{r_i}\left[\frac{\ln\left(\frac{r_i+d_l/2}{r_i}\right)}{k_w\,2\pi\,\Delta z} + \frac{\ln\left(\frac{r_i}{r_i-d_l/2}\right)}{k_l\,2\pi\,\Delta z}\right] = T_w - T_l \quad \text{(B.14)}$$

Where the terms in brackets are radial thermal resistances as defined in Eq. 3.1.

Applying the same procedure for $\dot{q}_r$, the heat flow from the liquid to the vapor (or vice versa) can be written as follows:

$$\dot{q}_{r_i-d_l}\left[\frac{\ln\left(\frac{r_i-d_l/2}{r_i-d_l}\right)}{k_l\ 2\pi\ \Delta z}+R_{ph}\right]=T_v-T_l \tag{B.15}$$

Adding all the integrated terms together, cancelling out the terms on the heat transfer in the axial direction as per the assumptions for RHPs, defining the thermal resistances and locations according to Figure 3.3 and finally replacing $\frac{\partial h}{\partial t}$ with $c_p\frac{\partial T}{\partial t}$, the following final equation is found:

$$\rho_l^i\ V_l^i\ c_{p_l}^i\frac{\mathrm{d}T_l^i}{\mathrm{d}t}=\frac{T_w^i-T_l^i}{R_{w_{r2}}^i+R_{l_{r1}}^i}+\frac{T_v^i-T_l^i}{R_{ph}^i+R_{l_{r2}}^i} \tag{B.16}$$

It should be noted that the last term of Eq. B.16 is equal to the heat input / output associated with phase change rate due Eq. 3.6 of the thesis.

Appendix C - Material properties

In Chapter 4 of this dissertation, Dowtherm A, phenanthrene and cesium were selected to be used in the simulations of the heat pipe assisted annealing line. The thermophysical properties of these working fluids as well as of the heat pipe and the strip used in the simulations are shown in the tables below as a function of temperature (valid for the temperature ranges they were used). Fluid and material properties are obtained from the following:

[1] C. L. Yaws,Chemical properties handbook (McGraw-Hill, 1999).

[2] D. C. Company,Dowtherm, A. heat transfer fluid – product technical data.

[3] P. J. Linstrom and W. G. Mallard, The nist chemistry webbook: A chemical data resource on the internet, Journal of Chemical & Engineering Data, 1059 (2001).

[4] M. Ghatee and M. Sanchooli, Viscosity and thermal conductivity of cesium vapor at high temperatures, Fluid phase equilibria 214, 197 (2003).

[5] P. Colonna and T. Van der Stelt, Fluidprop: a program for the estimation of thermo physical prop-erties of fluids, Energy Technology Section, Delft University of Technology, Delft, The Netherlands (2004).

Fluid vapor pressures

$$\log_{10} p = A - \frac{B}{C-(T-273.15)}$$

(p in bar and T in °C)

	A	B	C
Dowtherm A	4.35	1987.623	-71.556
Phenanthrene	4.68	2673.000	-40.700
Cesium	3.69	3453.122	-26.829

Liquid specific heat capacities

$$c_p = AT^2 + BT + C$$

(c_p in kJ/(kg.K) and T in °C)

	A	B	C
Dowtherm A	5.885e-7	2.536e-3	1.547
Phenanthrene	5.129e-6	-1.207e-3	1.968
Cesium	1.155e-7	-7.578e-5	0.259

Liquid thermal conductivities

$$k = AT^2 + BT + C$$

(c_p in W/(m.K) and T in °C)

	A	B	C
Dowtherm A	-	-1.600e-4	0.142
Phenanthrene	-4.100e-8	-4.784e-6	0.128
Cesium	-6.169e-6	-2.137e-4	20.714

Liquid densities

$$\rho = AT^2 + BT + C$$

(ρ in kg/m^3 and T in °C)

	A	B	C
Dowtherm A	-8.095e-4	-0.607	1,061
Phenanthrene	-8.717e-4	-0.304	1,093
Cesium	-5.893e-5	-0.547	1,865

Liquid viscosities

$$\mu = AT^2 + BT + C$$

(μ in mPa.s and T in °C)

	A	B	C
Dowtherm A	1.031e-5	-7.197e-3	1.430
Phenanthrene	5.802e-6	-5.589e-3	1.499
Cesium	3.026e-7	-5.481e-4	0.393

Fluid latent heats of vaporization

$$H_{fg} = AT^2 + BT + C$$

(H_{fg} in kJ/kg and T in °C)

	A	B	C
Dowtherm A	-5.336e-4	-0.225	389.3
Phenanthrene	-5.646e-4	-0.100	402.6
Cesium	-4.158e-5	-0.115	592.9

Liquid thermal expansion

$$\beta = AT^2 + BT + C$$

(β in 1/K and T in °C)

	A	B	C
Dowtherm A	1.158e-8	-2.157e-6	9.916e-4
Phenanthrene	1.091e-8	-4.053e-6	1.115e-3
Cesium	1.689e-10	4.745e-8	3.194e-4

Vapor viscosities

$$\mu = AT + B$$

(μ in mPa.s and T in °C)

	A	B
Dowtherm A	2.039e-5	4.838e-3
Phenanthrene	1.765e-5	4.695e-3
Cesium	2.601e-5	8.269e-3

Heat pipe properties

$$c_p = AT^B$$
$$k = AT + B$$
$$\rho = A$$
$$\varepsilon = A$$

(c_p in J/(kg.K), k in W/(m.K), ρ in kg/m^3 and T in °C)

	A	B
c_p	322.418	9.689e-2
k	1.432e-2	14.912
ρ	7900	-
ε	0.3	-

Strip properties

$$c_p = AT^2 + BT + C$$
$$k = AT + B$$
$$\rho = A$$
$$\varepsilon = A$$

(c_p in J/(kg.K), k in W/(m.K), ρ in kg/m^3 and T in °C)

	A	**B**	**C**
c_p	1.201e-3	-0.285	521.84
k	-2.675e-2	50.58	-
ρ	7870	-	-
ε	0.2	-	-

Curriculum Vitæ

Metin Celik was born on the 12th of December 1986 in Rize, Turkey. He studied chemical engineering during his bachelor's degree at Bogazici University, graduating in 2010. He pursued a master's degree in sustainable energy technology in Delft University of Technology and graduated cum laude in 2012. He worked on carbon project development for one and a half year in Mavi Consultants of GITEC-IGIP Holding SE. In 2015, he got admitted to the PhD programme at Delft University of Technology under the supervision of Prof. Wiebren de Jong and Prof. Bendiks Jan Boersma. During his PhD, he worked on the heat pipe assisted annealing concept, a project in collaboration with Tata Steel and Drever International. Since May of 2019, he is working at the Thermal Processes group of Tata Steel Europe R&D as a Principal Researcher.

List of Publications

Journal publications

1. M. Celik, K. Devendran, G. Paulussen, P. Pronk, F. Frinking, W. de Jong, and B. J. Boersma, *Experimental and numerical investigation of contact heat transfer between a rotating heat pipe and a steel strip*, International Journal of Heat and Mass Transfer, **122**, 529-538 (2018), DOI:10.1016/j.ijheatmasstransfer.2018.02.009.

2. M. Celik, G. Paulussen, D. van Erp, W. de Jong, and B. J. Boersma, *Transient Modelling of Rotating and Stationary Cylindrical Heat Pipes: An Engineering Model*, Energies, **11**(12), 3458 (2018), DOI:10.3390/en11123458.

3. M. Celik, M. Patki, G. Paulussen, W. de Jong, and B. J. Boersma, *Dynamic Modelling of the Heat Pipe Assisted Annealing Line*, Journal of Heat Transfer, **141**(9), 091801 (2019), DOI:10.1115/1.4042701.

Proceedings

1. M. Celik, G. Paulussen, P. Pronk, L. Sturnack, W. de Jong, and B. J. Boersma, *Modelling of a single rotating heat pipe for heat pipe assisted annealing concept*, in Proc. of the Joint 18th IHPC and 12th IHPS, Jeju, Korea, June 12-16, 2016, pp.72-78.

Acknowledgements

I am grateful that I found the opportunity to work as a PhD student in TU Delft Process & Energy Department and in very close collaboration with Tata Steel Europe R&D. There has been a great deal of learning and personal development involved in these 4 years. On the other hand, PhD is mentally very demanding and challenging. Therefore, PhD students heavily rely on supports from others, be it family members, friends or colleagues. This makes Acknowledgements an essential part of all PhD theses. This thesis is no exception.

First and foremost, I would like to thank Geert Paulussen. Not only the project exists thanks to you, but also you have been an influential figure during these 4 years. You have substantially contributed to my knowledge and critical thinking skills, helping me become a better engineer. I see it a privilege to have worked with you.

I would like to express my gratitude to my promotor Prof. Wiebren de Jong. Wiebren, first of all thank you for trusting me with this project. I benefited a lot from your feedback and your help on content and project management. I also learned from your approach to MSc students and I could put my learnings into practice thanks to a large number of very good students you included in the project. And above all, I appreciate the open communication culture you provided. Additionally, I am grateful to my other promotor Prof. Bendiks Jan Boersma for his help on the content. Thank you for making me part of this exciting project. Moreover, I benefited from your technical expertise which has been a sanity check for the numerical part of the work.

I am grateful to the committee members for their involvement in the evaluation of this dissertation. More specifically, I would like to thank Prof. Theo van der Meer, Prof. Piero Colonna, Prof. Jean-Marie Buchlin, Prof. David Smeulders and Dr. Wim van der Meer for reviewing my work. I had many interesting discussions with the committee members during these 4 years. These discussions are separately acknowledged in other paragraphs.

There have been many people from TU Delft that helped me on a daily basis. Bas, thank you very much for your patience and hard-work. You found many great practical solutions to unforeseen problems in the setup. Your contribution to the experimental part of the work is beyond measure. Jaap, Michel and Martijn, thank you for assisting me with a positive attitude. Secretaries of the department, Eveline, Leslie and Helma, thank you for being available for assistance. Additionally, I would like to thank Léon Rohrbach from the University of Groningen for carying out the GC analysis.

I had many interesting conversations on technical content with Prof. Piero Colonna, Dr. Mathieu Pourquie, Dr. Rene Delfos and Dr. Wim Haije. Your willingness to help is much appreciated. I would like to thank Prof. Dirk Roekaerts for

his guidance during my MSc study and for referring me to Prof. de Jong in the first place.

I cannot emphasize enough the contribution of the MSc students I worked with during my PhD. Bob, Karthikeyan, Mrunal, Vinayak, Stefan and Frederik, a sincere thank you to all of you. You all did a great job. It is fair to say that this thesis has been realized thanks to your contributions. I always considered you as my colleagues rather than students and I learned a lot from all of you. I hope that you also learned from me.

Additionally, I am thankful for the fruitful and interesting discussions I had with Prof. Jean-Marie Buchlin at the von Karman Institute during the first year of my PhD, with Prof. David Smeulders at Tata Steel IJmuiden and TU Eindhoven, with Dr. Wessel Wits during the heat pipe conferences and with Jeroen de Jong during his MSc study at Tata Steel Europe R&D.

During these 4 years, probably half of the time I worked at Tata Steel IJmuiden. Working in an industrial environment during PhD is a great experience. There are lots of colleagues and mentors I would like to thank there as well.

First of all, I would like to thank Wim van der Meer and Hans van der Weijde, Programme Managers of the heat pipe assisted annealing project. I believe that only few PhD students are lucky enough to have regular meetings with visionary high-level managers as yourselves. It was great to observe your approach to project management, your critical thinking, communication skills and modesty. I want to acknowledge the contributions of my first group leader at Tata Steel, Pepijn Pronk. Pepijn, you have become a role model to me during the first half of my PhD. You introduced me to a lot of very useful concepts to help my planning and management skills. Additionally, I would like to thank Mustapha Bsibsi, my group leader at Tata Steel. Mustapha, you analyze the way I work in a clear way and show me my strong points and improvement opportunities. This helps and motivates me to improve as an R&D engineer. I would also like to thank all the colleagues who made the time I spent at Tata Steel enjoyable. One of the reasons for my decision to continue at Tata Steel R&D is the culture you have fostered there.

Out of the three different experiments included in this thesis, two were conducted at Tata Steel IJmuiden Lab 5. Many colleagues helped me with the setting up and execution of these experiments. First of all, I would like to acknowledge the contributions of Ferry Frinking and Cor Bijleveld. Ferry, I learned a lot from your approach to experimenting and to safe practices. Cor, you facilitated the execution of experiments a lot during my first year and you have done this with a positive attitude. Additionally, I am thankful to Bastiaan de Bruijn, Stephan de Bruijn and David Prins for their valuable opinions in the design of experimental setups and for helping me with the instruments I worked with.

Additionally, I would like to thank Amédéo di Giovanni, Olivier Pensis, Laurent Sturnack, Serge Vanderheyden, Michel Renard, Jean Marc Raick and Jean-Pierre Crutzen of Drever International, third partner of our collaboration project. Chapter 5 of this thesis is built upon the plant layout designed by Drever International. Furthermore, I had some very fruitful interactions with all of you during the team and board meetings, leading to better outcomes.

I would like to thank my friends who were around during these 4 years and who helped me survive. Julia, Tim, Sebastian, Remco and Dion, we have spent many good times together at TU Delft and elsewhere. Some of you witnessed my wedding, some shared my happiness with the new little member of my family. You were always available and you brought joy to my life in your own ways. I think it is fair to say that except for my family, you were my main mental support and motivator during this journey. A sincere thank you to all of you. Fatma and Hakan, all the many coffee breaks with you added much happiness to my time there. Additionally, Marloes, Karsten, Weiwei, Christos, Mate, Max, Hassan, Alper, Megha, Mara, Christos and Andrea I am glad that I got to meet you and thank you for being good PhD companions. Giannis, we followed similar paths since 2010 and it was great to have you on my side at all times. And thus, I name you my paranymph (consider it a gift, not a punishment). Tanel, Kati, Srikanth and Faidra, thank you for sharing good memories with me since masters.

Finally, I would like to thank my family. My dear parents, we (me and my brothers) are lucky to have been born to such caring, compassionate and intellectual parents. I'd like to think that we all flourished well in this fruitful environment you have provided. Bahar, Deniz, Aydin and Murat, I consider myself extremely privileged to have such a loving family. Your presence is a great source of support, reassurance and happiness. Umut, you brought bliss to our family.

And Serpil, the highlight of my life. It would be a futile attempt to fully describe what you mean to me and how you help me. Suffice to say that you saw me through my darkest hours and you are the source of my brightest ones. Last and most importantly, my dear Ekim, I love you.